Conventional and Multiple Trellis-coded 8-PSK Modulations over EHF Mobile Satellite Channels

by

Nan Yuan Rao, B.A.Sc.

A thesis submitted to
the School of Graduate Studies and Research
in partial fulfillment of
the requirements for the degree of

Master of Applied Science

Ottawa-Carleton Institute for Electrical Engineering
Faculty of Engineering
Department of Electrical Engineering
University of Ottawa
Ottawa, Ontario, Canada, K1N 6N5

September 20, 1994

ISBN 0-612-00551-8

Abstract

The increasing demand of the frequency spectrum for land mobile satellite communication services has led to the approach of moving the current operating frequency up to EHF (30/20 GHz) band. In this thesis, the propagation characteristics of the EHF mobile satellite communication channel are estimated and modeled. Conventional and multiple trellis-coded modulation schemes designed for fading environment are considered for the EHF mobile satellite channel. The design criteria for optimum trellis-coded modulation scheme on the fading channel are studied. Through computer simulation, the performances of both coherent and differential trellis-coded modulation systems with selected coding schemes on the EHF channel models are evaluated. The effects of using channel state information and interleaving technique on the trellis-coded modulation systems are also studied. Finally the simulation results are presented and discussed.

I hereby declare that I am the sole author of this thesis.

I authorize the University of Ottawa to lend this thesis to other institutions or individuals for the purpose of scholarly research.

Nan Yuan Rao

I further authorize the University of Ottawa to reproduce this thesis by photocopy or by other means, in total or in parts, at the request of other institutions or individuals for the purpose of scholarly research.

Nan Yuan Rao

Acknowledgments

I would like to express my sincere thanks to my supervisor, Dr. Jean-Yves Chouinard, for his academic guidance and financial support during the course of this research.

I would also like to thank Dr. Jin Yun Zhang of the Bell Northern Research for her valuable suggestions and various supports.

Finally, to my wife and parents, I owe a special debt of gratitude. Their affection and encouragement made the writing of this thesis possible.

Contents

List of Figures

List of Tables

List of Acronyms

ACTS	Advanced Communication Technology Satellite
AFD	Average Fade Duration
AWGN	Average White Gaussian Noise
BER	Bit Error Rate
BPSK	Binary Phase Shift Keying
CSI	Channel State Information
DSP	Digital Signal Processing
DTCM	Differential Trellis-coded Modulation
EHF	Extremely High Frequency
GHz	Giga Hertz
ISI	Intersymbol Interference
LCR	Level Crossing Rate
LMS	Land Mobile Satellite
LOS	Line of Sight
M-PSK	M-ary Phase Shift Keying
MTCM	Multiple Trellis-coded Modulation
MTCM3/6_8s	Rate 3/6 8-state multiple TCM
MTCM4/6_4s	Rate 2/3 4-state multiple TCM
NASA	National Aeronautic Space Agency
QPSK	Quadrature Phase Shift Keying
pdf	Probability Density Function
PCS	Personal Communication Service
PSK	Phase Shift Keying
SNR	Signal to Noise Ratio
SPW	Signal Processing Worksystem
TCM	Trellis Coded Modulation
TCM2/3_4s	Rate 2/3 4-state conventional TCM
TCM2/3_8s	Rate 2/3 8-state conventional TCM
TCM2/3_16s	Rate 2/3 16-state conventional TCM
TCM2/3_64s	Rate 2/3 64-state conventional TCM
VA	Viterbi Algorithm
8-PSK	Eight Phase Shift Keying

List of Symbols

A_c	Envelope of the constant direct wave
$a(\mathbf{x}, \hat{\mathbf{x}})$	Number of bit errors that occur when symbol sequence $\mathbf{x}$ is sent and symbol sequence $\hat{\mathbf{x}}$ is decoded
b	Number of input bits of multiple TCM encoder
b_0	Average scattered power due to multipath
$b_{0(1.5GHz)}$	b_0 for 1.5 GHz frequency
$b_{0(20GHz)}$	b_0 for 20 GHz frequency
$\tilde{b}$	The number of encoded bits
BT	Normalized fading bandwidth
c	Speed of light
C	Set of all possible coded sequences
$C1$	Constant
D	Interleaving depth
d_0	Variance of $\ln r$ (natural logarithm of envelope r)
$d_{0(1.5GHz)}$	d_0 for 1.5 GHz frequency
$d_{0(20GHz)}$	d_0 for 20 GHz frequency
d^2_{free}	Squared free Euclidean distance
d_t	Depth of trees intercepted by LOS signal (in meters)
$E\{\}$	Expectation
E_b	Energy per bit
$erfc()$	Complementary error function
$\bar{E}_b$	Average energy per bit
$\bar{E}_s$	Average energy per symbol
E_s	Energy per symbol
f_c	Carrier frequency
f_d	Maximum Doppler frequency shift
f_i	The Doppler frequency shift of the ith signal
$I(t)$	In-phase component of signal
$I_i(t)$	In-phase component of the ith signal
$I_0(x)$	Zeroth order Bessel function
k	Time index
K	Power ratio of LOS and the multipath components

l	Number of encoded bits in a multiple TCM encoder
L	Length of the shortest error event path
L_η	Length of the error event path
m	Number of input bits of a conventional TCM encoder
m_1	Number of encoding bits of a conventional TCM encoder
m_2	Number of uncoded bits of a conventional TCM encoder
M_b	Branch metric
n	Number of mapping bits of a conventional TCM encoder
N	Total number of the transmitted bits in the simulation
n_1	Number of encoded bits of a conventional TCM encoder
n_k	Complex Gaussian noise at time k
N_0	Noise power spectral density
N_R	Level crossing rate at level R
$\bar{N}_R$	Average level crossing rate at level R
$n(t)$	White Gaussian noise
P	Squared distance product along the shortest error event path
P_{min}	Minimum squared Euclidean distance product
P_b	Bit error probability
$p_{log-normal}(z)$	Log-normal probability density function of z
$p_{Rayleigh}(r)$	pdf of r for Rayleigh model
$p_{Rician}(r)$	pdf of r for Rician model
$p_{Rician}(\phi)$	pdf of ϕ for Rician model
$p(R, \dot{r})$	Joint pdf of $\dot{r}$ and r at $r = R$
$p_{sh-Rician}(r)$	pdf of r for Log-normally shadowed Rician model
$p_{sh-Rician}(\phi)$	pdf of ϕ for Log-normally shadowed Rician model
$P(\mathbf{x})$	A priori probability of transmitting $\mathbf{x}$
$P(\mathbf{x} \to \hat{\mathbf{x}})$	Pairwise error probability
$P(\mathbf{x} \to \hat{\mathbf{x}}\|\mathbf{r})$	Pairwise error probability conditioned on $\mathbf{r}$
q	Multiplicity of MTCM
$Q_i(t)$	The quadrature component of the ith signal
$Q(t)$	The quadrature component of a signal
$\dot{r}$	Changing rate of the signal envelope r
$r(t)$	Envelope of $s(t)$
r_k	Normalized fading signal amplitude at time k
r_s	Estimate of channel fading amplitude at stage s
S	Interleaving span
s	Stage index of a trellis diagram
$S_{direct}(t)$	Direct signal component
$S_{diffuse}(t)$	Diffuse signal component
$s(t)$	Received signal
T_N	Average fade duration
T_s	Symbol interval

u_k	Input signal of differential detector at time k
u_{k-1}	Input signal of differential detector at time $k-1$
v	Speed of vehicle
v_k	Output signal of differential encoder at time k
v_{k-1}	Output signal of differential encoder at time $k-1$
$\mathbf{x}$	Transmitted M-ary PSK symbol sequence
$\hat{\mathbf{x}}$	Decoded M-ary PSK symbol sequence
x_k	Transmitted M-ary PSK symbol at time k
$\hat{x}_k$	Decoded M-ary PSK symbol at time k
x_s	Branch symbol of the associated encoder at stage s
$\mathbf{y}$	Channel output sequence
y_k	Channel output at time k
y_s	Input symbol at stage s
$z(t)$	Envelope of the shadowed direct wave
μ	Mean of $\ln z$
$\mu_{1.5GHz}$	μ for 1.5 GHz frequency
μ_{20GHz}	μ for 20 GHz frequency
η	Set of all k for which $x_k \neq \hat{x}_k$
σ^2	Variance of Gaussian noise in each dimension
σ_l^2	Variance of $\ln z$
σ_p^2	Variance of phase
β	Constant
$\phi(t)$	Phase of $s(t)$
ρ	Correlation coefficient
ρ_s	Frequency scaling factor
α	Attenuation coefficient
$\alpha_{1.5GHz}$	Attenuation coefficient for 1.5 GHz frequency
α_{20GHz}	Attenuation coefficient for 20 GHz frequency
α_i	Arriving angle of the ith signal
λ	Number of encoder memory (in bits)
θ_i	Phase of the ith signal
ξ	Constant

Chapter 1

Introduction

1.1 Mobile Satellite Communications at EHF Frequencies

Land mobile satellite (LMS) communication systems have developed rapidly over the past few years. Because of the increasing utilization of the spectrum in the present operating frequency bands and the requirement for wider information bandwidth, it is necessary to find more frequency resources to accommodate further developments of mobile satellite communication services, especially those supporting the coming global personal communication system (PCS) [1]. Limited by the satellite orbit slots, this spectrum demand leads to extending the current operating carrier frequency to higher bands, for instance, the 30/20 GHz band referred as the Extremely High Frequency frequency (EHF) band.

In addition to the available large spectrum, employing higher carrier frequencies such as 30/20 GHz can also bring several other implementation advantages, including reduced hardware size and weight of the terminal equipment [2, 3], smaller antenna diameters, and the capability of implementing new anti-jamming techniques [4].

1.2 Challenges for EHF System Design

The propagation constraints at 30/20 GHz frequency can be quite severe if compared with current L-band (1.6/1.5 GHz) satellite systems. It can be expected that the EHF channels will suffer larger Doppler frequency shifts and more severe signal deterioration caused by the shadowing effect. Also, the absolute frequency offsets and drifts of the EHF oscillators will also increase significantly due to the oscillator inaccuracy.

In design and development of an EHF land mobile satellite system, the first challenge we are facing is how to model the EHF propagation channel properly. Since the propagation of a LMS communication channel is usually affected by the random nature of the transmission media in space, statistical analysis and modeling techniques are very useful tools for evaluation of the propagation effects on mobile satellite communication links. Appropriate channel propagation models play an important role in system design and implementation.

The second challenge is to find efficient modulation/demodulation and error control strategies for the EHF mobile satellite communication channels. In order to combat the severe channel impairments to be encountered on an EHF mobile satellite channel, powerful and efficient signal transmission techniques must be used. Trellis-coded modulation is a power and bandwidth efficient modulation scheme. Recent studies have shown that trellis-coded modulation demonstrates a significant bit error performance in the fading channel environment. It is therefore a good modulation candidate to be considered for the EHF mobile satellite communication system.

1.3 Related Research

Although the EHF mobile satellite communications have received much attention in recent years, there are still a limited number of published results that can be found with respect to the channel modeling and corresponding impairment mitigating techniques, such as trellis-coded modulation. However, related researches on L-band

LMS systems have been conducted extensively. Some relevant results are summarized in the following subsections.

1.3.1 LMS Channel Modeling

The propagation characteristics of mobile communication channel can be usually represented by the Rayleigh and Rician random processes depending on the presence or not of a LOS component in addition to the multipath signals [5, 6]. To characterize the LMS channel, many studies have been conducted on channel modeling and statistical analysis [7, 8, 9, 10, 11, 12, 13], among which the log-normally shadowed Rician model [7] proposed by Loo for the L-band LMS channel is well recognized. The log-normally shadowed Rician model assumes that the amplitude of the LOS component under foliage shadowing follows the log-normal distribution with a multipath component being Rayleigh distributed. The computer models for the Rayleigh, Rician and log-normally shadowed Rician channels are described in [10] and a set of model parameters for the L-band channels are presented, which is especially suited for an area of high latitude as in Canada.

In order to explore the necessary technologies and collect propagation data at 30/20 GHz bands, several experimental satellites have been launched to meet the need of the sponsoring agency's research. These include the European Space Agency's Olympus satellite, the NASA's Advanced Communications Technology Satellite (ACTS) and the ETS-VI satellite of the Japanese National Space Development Agency. Each of these satellites is capable of working at 30/20 GHz frequencies [1].

The data collected from experimental mobile satellite systems on 30/20 GHz channel is still not publicly accessible, and it is therefore not possible at this point to develop an EHF mobile satellite propagation model using the actual channel statistics. In this circumstance, propagation models extrapolated from existing L-band (1.6/1.5 GHz) channel parameters constitute an alternative choice.

In [2, 3, 4], the possible channel interference and propagation impairments on

30/20 GHz frequencies are estimated and analyzed. Due to the limitation of available measured data for LMS system operating at these frequency bands, a frequency scaling technique is applied in certain conditions to estimate signal attenuation factors. Based on [3] and [10], a set of model parameters is derived in [14, 15] for the Ka-band LMS channel by conducting scaling transformation from L-band parameters. From estimated channel parameters, performances of coherent and non-coherent PSK systems are evaluated over the proposed EHF channel model in [14, 15].

1.3.2 Trellis-coded Modulation on Fading Channels

Trellis-coded modulation (TCM), originally proposed by Ungerboeck [16], is a class of digital transmission modulation schemes in which the error control coding and modulation techniques are optimally integrated. It is indicated that the performance of a conventional TCM code improves when the number of states increases. However, as the state number exceeds a certain value, the additional coding gain increases very slowly. In order to achieve higher coding gains, the concept of multidimensional trellis-coded modulation was introduced [17, 18, 19]. As a special form of the multidimensional TCM modulation, multiple trellis-coded modulation (MTCM) was proposed by Divsalar [20]. It can be viewed as coding onto a multidimensional signal set constructed from successive channel symbols. Compared with conventional TCM, multiple TCM transmits more channel symbols per trellis branch.

Due to the bandwidth efficiency and the significant coding gain over average white Gaussian noise channel (AWGN), trellis-coded modulation technique has received a great attention in the application to land mobile satellite communications. The most influential papers were given by Divsalar and Simon. In [21, 22, 23], they presented a new design criteria and signal set partitioning method for TCM over fading channel, which are different from those for TCM on AWGN channel [16, 24]. The code design methods were demonstrated and a set of multiple TCM codes designed specially for fading channel was also presented in [23]. With the new code design criteria, Schlegel and Costello constructed a set of new codes for conventional 8-PSK TCM in [25]. In [26, 27], the rate 2/3, 4-state conventional 8-PSK TCM codes were extensively studied on fading channels by Wilson, Leung and Jamali.

Coherent and differential TCM systems are evaluated by computer simulations in the presence of the Rayleigh, Rician and shadowed Rician fading channel in [21, 26, 28, 29, 30, 31, 32, 33]. On the other hand, several papers concentrated on the analytical performance bounds. In [21, 22, 34], the error performance of both coherent and differential M-ary TCM in the Rayleigh and Rician channels has been upper bounded by the Chernoff bound. A tighter upper bound is derived by McKay, McLane and Biglieri for trellis-coded M-ary PSK in the Rayleigh, Rician and shadowed Rician channels in [35]. In [36], an accurate expression of the pairwise error probability for TCM transmitted over the Rayleigh fading channel is presented. Under the correlated Rician and shadowed Rician fading conditions, the pairwise error probabilities of the differential trellis-coded M-ary PSK signals are calculated directly and approximated asymptotically in [37, 38].

1.4 Thesis Objectives

One objective of this thesis is to characterize the 30/20 GHz EHF mobile satellite communication channel with proper models based on the knowledge of the existing L-band LMS channel statistics and assumptions made for the EHF channel conditions. The main objective is to set up a computer simulation system, based on the proposed EHF channel model, to evaluate and assess the performance of the trellis-coded modulation schemes that are optimally designed for fading channels.

1.5 Thesis Organization

The remainder of this thesis is organized into six chapters and an appendix, which are summarized as follows:

In Chapter 2, the commonly recognized channel models, which can be used to characterize the land mobile satellite communication channels, are described in detail. The corresponding computer models are also presented. Based on the prediction of the channel characteristics over the EHF frequency band, a set of channel model parameters is derived from existing L-band model parameters by using a frequency scaling method. The second order statistics of the channel models are also considered and computer simulation results of channel model statistics are shown.

Chapter 3 presents the conventional and multiple trellis-coded modulation and demodulation techniques. The design criteria for an optimum TCM scheme on fading channel are discussed. According to these design principles, several TCM schemes are selected and analyzed. The advantage of the interleaving technique is also discussed in this chapter.

Chapter 4 presents the analytical and asymptotic performance of the coherent and differential TCM systems on Rician fading channel with respect to the different channel conditions and system configurations.

In Chapter 5, the computer simulation tool used is briefly described. The implementation of simulation systems and function blocks, as well as the programming techniques are discussed in detail.

The simulation results of both coherent and differential TCM systems over the AWGN, Rayleigh, Rician and EHF mobile satellite fading channels are presented and discussed in Chapter 6.

In Chapter 7, conclusions are reached and suggestions for further research are given.

Appendix A includes some of the typical SPW block diagrams of the EHF mobile satellite communication link components used in the computer simulations.

Chapter 2

EHF Mobile Satellite Communication Channel

2.1 Introduction

In order to predict and analyze the performance of trellis-coded modulation scheme over EHF land mobile satellite communication channel, mathematical and computer models should be developed to characterize the channel propagation properties.

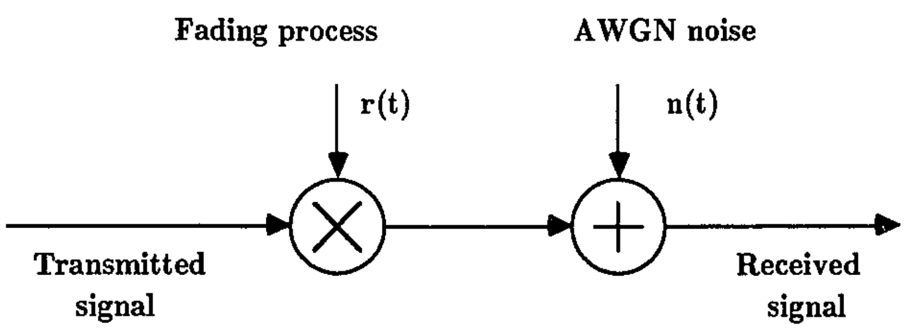

Figure 2.1: Channel model for EHF mobile satellite communications.

In this thesis, the EHF mobile satellite communication channel is mathematically modeled as a process in which a transmitted signal suffers from a multiplicative fading distortion and additive white Gaussian noise (AWGN), as shown in Figure 2.1. The discussions in this chapter focus on modeling the fading processes.

According to different types of propagation environment, the channel fading process can be further characterized as Rayleigh, Rician or log-normally shadowed Rician channel models. In following sections, the basic characteristics of signal propagation on a LMS channel are introduced first. The Rayleigh, Rician and shadowed Rician fading statistics and their corresponding application environment are discussed. A set of model parameters is derived from the existing L-band (1.6/1.5 GHz) channel model which are then used to simulate the fading processes on the EHF channels. Statistics obtained from the simulation of these fading processes are then presented.

2.2 Propagation Characteristics of LMS Fading Channel

In a land mobile satellite communication system, the signal transmitted between satellite and mobile terminal is subjected to several propagation factors [2, 3, 4]:

- Free space path losses that increase with the operating frequency.
- Ionospheric distortions, such as Faraday rotation, scintillation and refraction index variation. These distortions are inversely proportional to the frequency of operation.
- Tropospheric effects that result from depolarization, hydrometeor (rain, clouds, fog, snow, ice) attenuation, and atmospheric gas (primarily water vapor and oxygen) attenuation. These effects induce degradation that is increased with the operating frequency.
- Multipath propagation effects caused by the signal reflection and scattering from the terrain and obstacles (buildings and other man-made constructions) around mobile terminal.
- Vegetative shadowing

- The Doppler frequency shifts introduced by the relative movement between a mobile vehicle and a transmission signal.

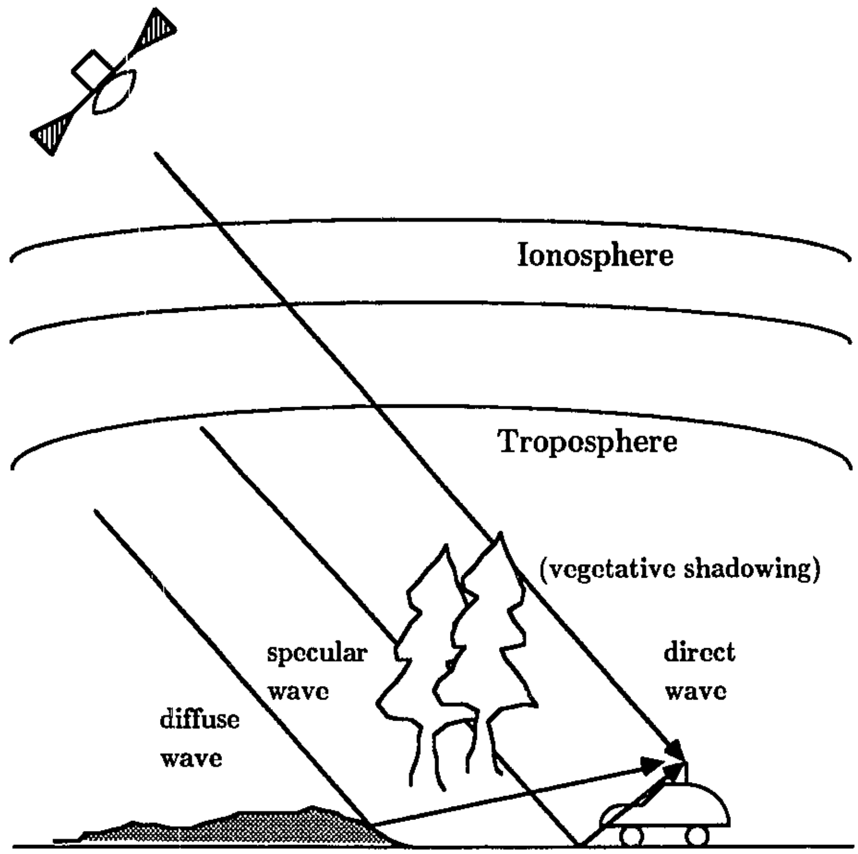

Figure 2.2: Propagation of the Land Mobile Satellite Signal.

As shown in Figure 2.2, the signal received at the antenna of a mobile terminal can be identified as the sum of three components: direct, specular and diffuse waves. The direct wave arrives at the mobile receiver via a line-of-sight path without reflection. The specular wave results from the ground reflection. The diffuse wave is produced by the multipath effect, which is actually the sum of a large number of individual signals with randomly distributed amplitudes and phases. The interaction among direct, specular and diffuse components causes severe fading of the received signal. Since the specular reflections can be substantially attenuated by properly adjusting the directivity of the antenna, the effect of the specular component on direct component can be ignored.

The Doppler frequency shift affects the bandwidth of the received signals. The maximum Doppler frequency shift f_d is determined by the traveling speed of vehicle v and the signal carrier frequency f_c.

$$f_d = \frac{v f_c}{c} \tag{2.1}$$

where c represents the speed of light.

Table 2.1 lists, for a carrier frequency f_c of 20 GHz and a vehicle speed ranging from 20 to 130 km/h, the maximum Doppler frequency shift f_d, as calculated from equation (2.1).

Table 2.1: Maximum Doppler frequency shift corresponding to different vehicle speeds at 20 GHz carrier frequency

speed v (km/h)	Maximum Doppler Shift f_d (Hz)
20	370
30	556
40	741
43	800
50	925
60	1111
65	1200
70	1296
80	1481
90	1667
100	1852
130	2400

Since the signal propagation characteristics are strongly dependent on the location of the mobile terminal, it is necessary to define some typical types of propagation environments to represent the different channel conditions. As a mobile vehicle travels through different areas, the signal components received at the antenna are quite different. Generally, three simplified propagation scenarios can be identified as follows:

1. Received signal consists of diffuse component only.
2. Received signal consists of diffuse and direct components.
3. Received signal consists of diffuse and shadowed direct components.

Corresponding to these scenarios, three mathematical models; the Rayleigh, Rician and log-normally shadowed Rician models, are developed to characterize the LMS fading processes.

2.3 Rayleigh Fading Model

As a mobile vehicle travels in a metropolitan area, the direct path between the satellite and the mobile vehicle is often obstructed by high buildings and other man-made constructions. In such case, there is no direct signal component at the mobile receiver, and the received signal $s(t)$ consists of only the multipath diffuse component $S_{diffuse}(t)$ reflected from all directions.

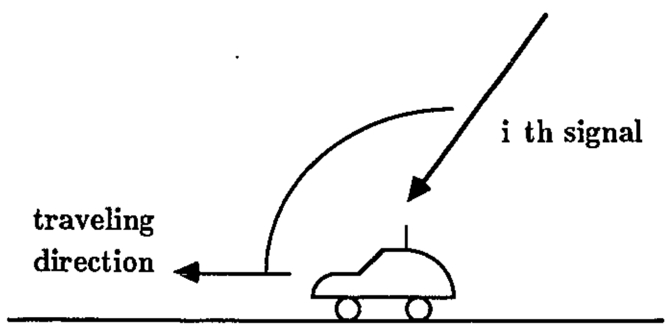

Figure 2.3: Angle between the ith receiving signal and vehicle traveling direction.

$$s(t) = S_{diffuse}(t). \tag{2.2}$$

The diffuse multipath component can be expressed as the sum of many independent scattering sources. Assume there are N indirect signals received at the mobile terminal. The ith signal has an arriving angle α_i with respect to the traveling direction of the vehicle as shown in Figure 2.3. The Doppler frequency shift f_i of the ith signal component is given by

$$f_i = \frac{v f_c}{c} \cos \alpha_i. \tag{2.3}$$

The ith reflected signal component $s_i(t)$ can be represented as

$$s_i(t) = r_i(t) \cos[2\pi(f_c + f_i)t + \theta_i] \tag{2.4}$$

where $r_i(t)$ is the envelope of the ith signal component and θ_i is its phase.

The signal component $s_i(t)$ can also be expressed in the in-phase and quadrature form as

$$s_i(t) = I_i(t) \cos 2\pi f_c t - Q_i(t) \sin 2\pi f_c t \tag{2.5}$$

where

$$I_i(t) = r_i(t) \cos(2\pi f_i t + \theta_i) \tag{2.6}$$

$$Q_i(t) = r_i(t) \sin(2\pi f_i t + \theta_i). \tag{2.7}$$

Therefore, the resulting diffuse signal is given by

$$s(t) = S_{diffuse}(t) = I(t) \cos 2\pi f_c t - Q(t) \sin 2\pi f_c t \tag{2.8}$$

where the resulting in-phase and quadrature components are

$$I(t) = \sum_{i=1}^{N} I_i(t) \tag{2.9}$$

$$Q(t) = \sum_{i=1}^{N} Q_i(t). \tag{2.10}$$

For the heavily built-up city areas, the number of the reflected signal N gets very large. In this case, according to the Central Limited Theorem, the $I(t)$ and $Q(t)$ components can be represented as two uncorrelated Gaussian random processes with zero mean and variance b_0. The signal envelope $r(t)$ is defined as

$$r(t) = \sqrt{I(t)^2 + Q(t)^2} \tag{2.11}$$

where $r(t)$ is a Rayleigh distributed random process. The Rayleigh probability density function of the signal envelope $r(t)$ is given by

$$p_{Rayleigh}(r) = \frac{r}{b_0} \exp(\frac{-r^2}{2b_0}), \quad r \geq 0 \tag{2.12}$$

where b_0 represents the average scattered power due to multipath.

The phase $\phi(t)$ of $s(t)$

$$\phi(t) = \arg[I(t) + jQ(t)] \tag{2.13}$$

is uniformly distributed in the interval $[-\pi, \pi]$.

2.4 Rician Fading Model

When a mobile vehicle travels in open areas, the direct wave from satellite generally encounters no obstacles and the diffuse wave is produced by the nearby terrain reflections. In this case, we assume the line-of sight signal suffers no distortion except the free space attenuation. The received signal at the mobile terminal is the sum of the diffuse and the direct components

$$s(t) = S_{direct}(t) + S_{diffuse}(t). \tag{2.14}$$

The direct component is just a signal wave with constant envelope, while the diffuse component consists of multipath signals and its envelope follows the Rayleigh distribution. Therefore, the received signal $s(t)$ is the sum of a constant direct component A_c and a Rayleigh distributed diffuse component.

$$s(t) = [A_c + I(t)]\cos 2\pi f_c t - Q(t)\sin 2\pi f_c t \tag{2.15}$$

The envelope $r(t)$ and phase $\phi(t)$ of the resulting signal $s(t)$ are

$$r(t) = \sqrt{[A_c + I(t)]^2 + Q(t)^2} \tag{2.16}$$

$$\phi(t) = \arg[A_c + I(t) + jQ(t)] \tag{2.17}$$

where the envelope $r(t)$ follows the Rician distribution [7] and its probability density function is given by

$$p_{Rician}(r) = \frac{r}{b_0}\exp[\frac{-(r^2 + A_c^2)}{2b_0}]I_0(\frac{rA_c}{b_0}) \quad r \geq 0 \tag{2.18}$$

where b_0 is the average scattered power due to the multipath, A_c is the envelope of the constant direct wave, and $I_0()$ is the modified Bessel function of zeroth order.

The severity of fading of the Rician model is usually determined by the K-factor, defined as the signal power ratio of the line-of-sight (LOS) and the multipath diffuse components. It can be expressed as

$$K = \frac{A_c^2}{2b_0}. \tag{2.19}$$

In terms of K-factor, the Rician probability distribution function of signal envelope r can also be given as [12, 34]

$$P_{Rician}(r) = \begin{cases} 2r(K+1)\exp[-(K+1)r^2 - K]I_0(2r\sqrt{K(K+1)}), & r \geq 0; \\ 0, & r < 0. \end{cases} \tag{2.20}$$

The phase statistics of the Rician fading process can be described by [12]

$$P_{Rician}(\phi) = \frac{e^{-K}}{2\pi} + \frac{\sqrt{K}\cos\phi e^{-K\sin^2\phi}}{2\sqrt{2\pi}}\left[2 - \mathrm{erfc}(\sqrt{K\cos\phi})\right] \tag{2.21}$$

where erfc() is complementary error function

$$\mathrm{erfc}(x) = \frac{2}{\sqrt{\pi}}\int_x^\infty e^{-t^2}dt. \tag{2.22}$$

2.5 Log-normally Shadowed Rician Fading Model

In most rural and suburban areas, roads are surrounded by trees and bushes. This vegetative shadowing causes attenuation to the direct wave component. The shadowing attenuation varies as the vehicle moving along the road. The envelope of the shadowed direct component follows a log-normal distribution [7]. The probability density function of the log-normal distribution is given by

$$p_{Log-normal}(z) = \frac{1}{z\sqrt{2\pi}\sigma_l}\exp\left[\frac{-(\ln z - \mu)^2}{2\sigma_l^2}\right] \tag{2.23}$$

where $z(t)$ is the envelope of the shadowed direct wave, μ is the mean of $\ln z$, and σ_l is the standard deviation of $\ln z$.

In this case, the received signal at the mobile receiver is the sum of a multipath diffuse component with the Rayleigh distribution and a shadowed direct component with log-normal distribution

$$s(t) = S_{shadowed-direct}(t) + S_{diffuse}(t). \tag{2.24}$$

The probability density function of the envelope $r(t)$ of the sum $s(t)$ was derived by Loo [7] and is given by

$$p_{sh-Rician}(r) = \frac{r}{b_0\sqrt{2\pi d_0}} \int_0^\infty \frac{1}{z} \exp\left[\frac{-(\ln z - \mu)^2}{2d_0} - \frac{(r^2+z^2)}{2b_0}\right] I_0\left(\frac{rz}{b_0}\right) dz. \quad (2.25)$$

The pdf of the phase $\phi(t)$ of $s(t)$ is approximately Gaussian [7]

$$p_{sh-Rician}(\phi) \cong \frac{1}{\sqrt{2\pi}\sigma_p} \exp\left[\frac{-(\phi-\eta)^2}{2\sigma_p^2}\right] \quad (2.26)$$

where b_0 is the average scattered power due to the multipath, $\sqrt{d_0}$ is the standard deviation of $\ln z$, and μ is the mean value of $\ln z$ due to shadowing. η and σ_p are the mean and standard deviation of the signal phase respectively.

Formula 2.25 can be simplified as following expressions [7]

$$p_{sh-Rician}(r) \approx \begin{cases} \frac{1}{r\sqrt{2\pi d_0}} \exp\left[\frac{-(\ln r-\mu)^2}{2d_0}\right], & r \gg \sqrt{b_0}; \\ \frac{r}{b_0} \exp\left[-\frac{r^2}{2b_0}\right], & r \ll \sqrt{b_0}. \end{cases} \quad (2.27)$$

The envelope r is log-normally distributed for larger values ($i.e., r \gg \sqrt{b_0}$) whereas Rayleigh distributed for smaller values ($i.e., r \ll \sqrt{b_0}$).

2.6 Computer Models for Fading Processes

Based on the mathematical expressions of the Rayleigh, Rician and log-normally shadowed Rician fading processes, three computer models can be implemented by manipulating the Gaussian random processes through lowpass filters [10] as shown in Figure 2.4. These baseband models assume the fading processes are frequency non-selective and generate multiplicative fading signals.

In the Rayleigh fading model of Figure 2.4 (a), the complex fading signal is generated by two narrow band Gaussian random signals with zero mean and variance b_0. The bandwidth of the lowpass filters is chosen to be equal to the normalized fading bandwidth, which is denoted by BT. The BT is determined by the maximum Doppler frequency shift f_d and the signal transmission rate.

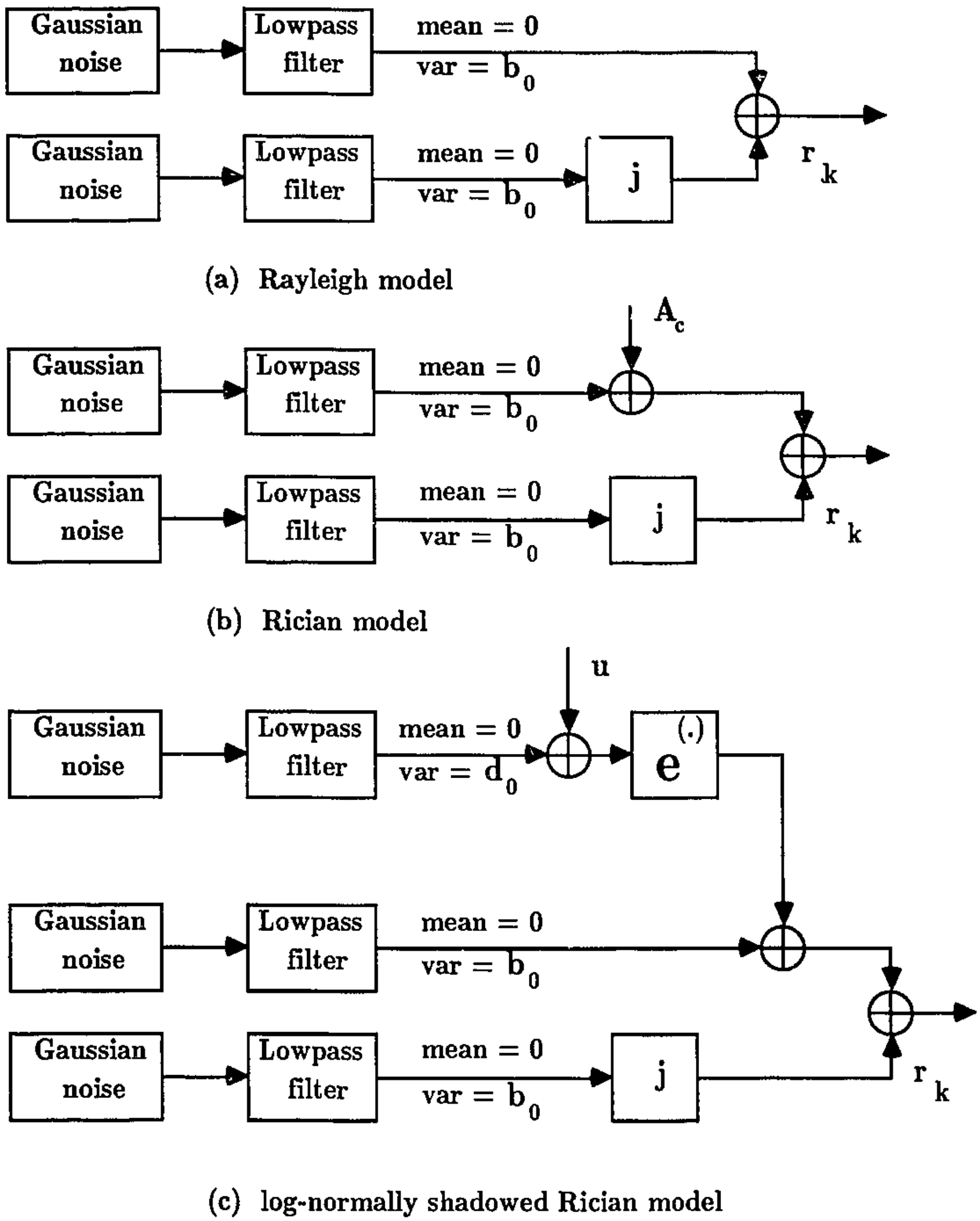

Figure 2.4: Computer channel models.

$$BT = f_d \times T_s \tag{2.28}$$

where T_s is the signal symbol duration.

The Rician fading signal is produced simply by adding a constant value, which represents the amplitude of the direct LOS component, to the real part of the complex Rayleigh fading signal as shown in Figure 2.4 (b).

Similarly, the log-normally shadowed Rician fading model is composed by two components, the Rayleigh distributed multipath component and the log-normally distributed LOS component. The log-normal LOS component is generated by letting a narrow band Gaussian random process with mean μ and variance d_0 pass through an exponential process as illustrated in Figure 2.4 (c). The bandwidth of the lowpass filter used to produce the shadowed LOS is normally chosen to be much smaller than BT since the fade rate of the direct wave is significantly lower than the fading rate of the multipath diffuse wave.

2.7 Model Parameters for EHF Fading Channel

From the analysis of previous sections, the fading processes of the EHF land mobile satellite communication channels can be characterized by the Rayleigh, Rician and log-normally shadowed Rician fading models corresponding to the three different types of propagation environments respectively. Actually, the Rayleigh and Rician channel models can be described as the special cases of the log-normally shadowed Rician model. From the shadowed Rician model, the Rayleigh model is derived if the log-normal component is set to zero. If the log-normal component is kept constant, the Rician model is generated.

2.7.1 Model Parameters for L-band Channel

By making use of the empirical results and models, an analysis of the overall LMS channel statistics has been carried out at the L-band frequencies [7, 10]. Based on the measurement statistics in the area of Ottawa, a set of parameters was proposed in [10] for the log-normally shadowed Rician fading model. These parameters are listed in Table 2.2 for different shadowing conditions.

Table 2.2: The model parameters for the L-band frequency

	b_0	μ	$\sqrt{d_0}$
Light shadowing	0.158	0.115	0.115
Average shadowing	0.126	-0.115	0.161
Heavy shadowing	0.0631	-3.91	0.806

The parameters b_0, μ and d_0 are defined in previous sections. The relation between these parameters and the log-normally shadowed fading model is illustrated in Figure 2.4 (c).

2.7.2 Characteristic Prediction of EHF Channel

Due to the high operating frequency, the 30/20 GHz EHF mobile satellite system mainly experiences the tropospheric propagation effects while the impact of the ionospheric distortions can be ignored [2, 3, 4]. Compared with the L-band system, the EHF channel suffers increased atmospheric attenuation, larger Doppler frequency shift, and more severe vegetative shadowing and multipath fading. Among these impairments, the additional atmospheric attenuation has less dramatic impact on the performance of the EHF satellite system [3]. Since the reflection coefficient and ground conductivity increase with the operating frequency, the multipath effect at 30/20 GHz frequency becomes much more severe than that at L-band [3]. However, if only the open and tree-shadowed areas are considered as the propagation environment, the antenna radiation beam at 30/20 GHz frequencies can be narrow enough to eliminate almost completely this additional multipath effect [3].

From these predictions, two basic assumptions are made for open and tree-shadowed propagation environment.

- The multipath fading at 30/20 GHz does not impair system performance more than that at L-band [3].
- The propagation attenuation results mainly from the foliage shadowing.

2.7.3 Derived EHF Channel Parameters for the Shadowed Rician Fading Model

Since the downlink design is critical to a satellite system development, the analysis and simulation of the channel models are concentrated on 20 GHz carrier frequency.

From the assumptions made above, the average scattered power due to multipath at L-band, b_0, can be directly adopted by the EHF model.

$$b_{0(20GHz)} = b_{0(1.5GHz)}. \tag{2.29}$$

For the shadowing parameters, μ and d_0, an empirical formula can be used to compute the attenuation coefficient α [3].

$$\alpha \simeq 0.45 f_c^{0.284} \quad for \quad 0 \leq d_t \leq 14 \tag{2.30}$$

where f_c is the carrier frequency in GHz and d_t is the depth of trees in meters intercepted by LOS signal.

By substituting 20 and 1.5 GHz frequencies into (2.30) respectively, two attenuation coefficients, α_{20GHz} and $\alpha_{1.5GHz}$, are calculated and the scaling factor ρ_s can be obtained as

$$\rho_s = \frac{\alpha_{20GHz}}{\alpha_{1.5GHz}} \simeq 2.1. \tag{2.31}$$

From this scaling factor, the corresponding EHF shadowing parameters can be easily derived.

$$\mu_{(20GHz)} = 2.1\mu_{(1.5GHz)} \tag{2.32}$$

$$d_{0(20GHz)} = 2.1d_{0(1.5GHz)}. \tag{2.33}$$

The derived EHF model parameters corresponding to the 20 GHz downlink transmission channel are listed in Table 3.1.

Table 2.3: Model parameters for 20 GHz carrier frequency

	b_0	μ	$\sqrt{d_0}$
Light shadowing	0.158	0.2415	0.1667
Average shadowing	0.126	-0.2415	0.2333
Heavy shadowing	0.0631	-8.211	1.168

2.8 Second-order Statistics of the Shadowed Rician Model

The models discussed above predict fade distributions for LMS signals. In addition to the first-order statistics, there are also two second-order statistics considered in this analysis: average fade duration (AFD) and level crossing rate (LCR). These statistics provide measures of the dynamics of the propagation which tell us how often severe fading occurs and how long it lasts. They are very important in characterizing the fading channel and useful for the design of a reliable LMS transmission system.

2.8.1 Level Crossing Rate

The level crossing rate (LCR) is defined as the expected rate at which the envelope crosses a specified signal level R with positive slope, which is given by [5]

$$N_R = \int_0^\infty \dot{r} p(R, \dot{r}) d\dot{r} \tag{2.34}$$

where $\dot{r}$ is the changing rate of the signal envelope (i.e., the time-derivative of $r(t)$) and $p(R, \dot{r})$ is the joint probability density function of $\dot{r}$ and r at $r = R$. With respect to the maximum Doppler frequency shift f_d, a normalized expression of the LCR for the log-normally shadowed Rician model is expressed as [10]

$$\bar{N}_R = \frac{N_R}{f_d} = \sqrt{2\pi(1-\rho^2)} \left[\frac{b_0(b_0 + 2\rho\sqrt{b_0 d_0})^{\frac{1}{2}}}{b_0(1-\rho^2) + 4\rho\sqrt{b_0 d_0}} \right] p(r) \tag{2.35}$$

in which, ρ is the correlation coefficient between envelope changing rate $\dot{r}$ and the receiving envelope $r(t)$.

2.8.2 Average Fade Duration

The average fade duration (AFD) is defined as the average length of time over which the signal attenuation is higher than a specified value. Corresponding to the normalized LCR, the normalized AFD is given as [5]

$$T_N = \frac{1}{\bar{N}_R} \int_0^R p(r) dr = \frac{p(r < R)}{\bar{N}_R}. \tag{2.36}$$

2.9 Computer Simulation of EHF Channel

The Rayleigh, Rician and log-normally shadowed Rician fading processes are simulated by using a computer software package SPW (which is described in Chapter 5). The simulations are carried out with parameters in Table 3.1 and with the normalized fading bandwidth BT equal to 0.25, which corresponds to a vehicle speed of 65 km/h if the signal transmission rate is 4800 symbols per second. 50,000 samples are generated for each simulation to obtain these results. The first and second order statistics of the simulated fading models under different conditions are graphically illustrated in Figures 2.5 - 2.7.

Figure 2.5 shows the cumulative distributions of the signal envelopes for the Rayleigh, Rician and shadowed Rician models with different parameters. It is indicated that the heavy shadowing experiences higher signal amplitude losses than that of the light and average shadowing in the log-normally shadowed Rician fading channel. For the Rician channel, the average amplitude level of the fading model increases with the value of K-factor. The amplitude levels of the heavy shadowed Rician model is quite close to that of the Rayleigh model with b_0 equal to 0.158.

In Figure 2.6, the curves show that the maximum value of the level crossing rate moves toward to the small signal amplitude as the power of the LOS component decreases. Figure 2.7 demonstrates that the average fade duration increases as the shadowing effect increases.

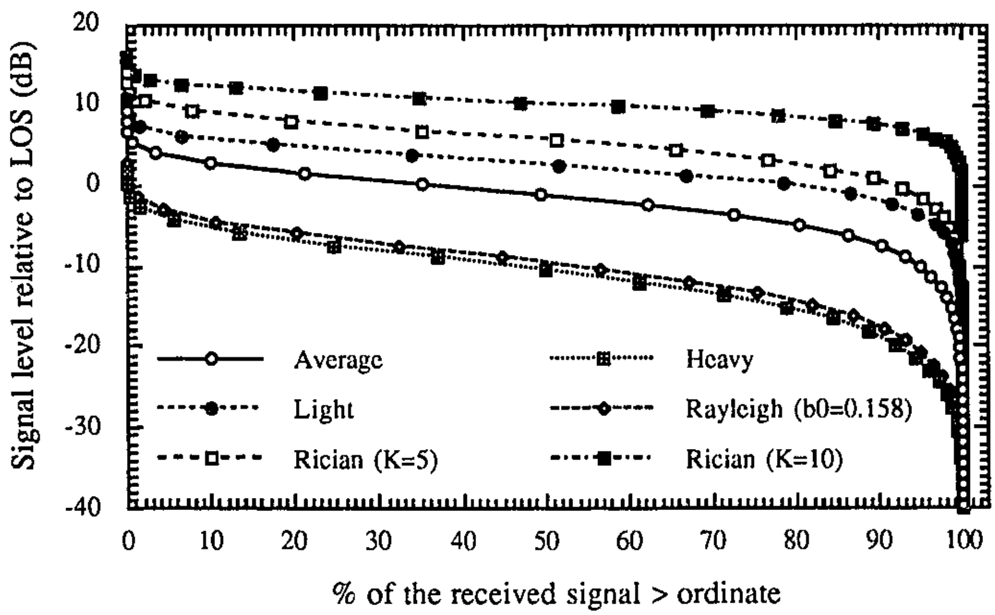

Figure 2.5: Envelope distributions of Rayleigh, Rician and shadowed Rician fading models (BT=0.25).

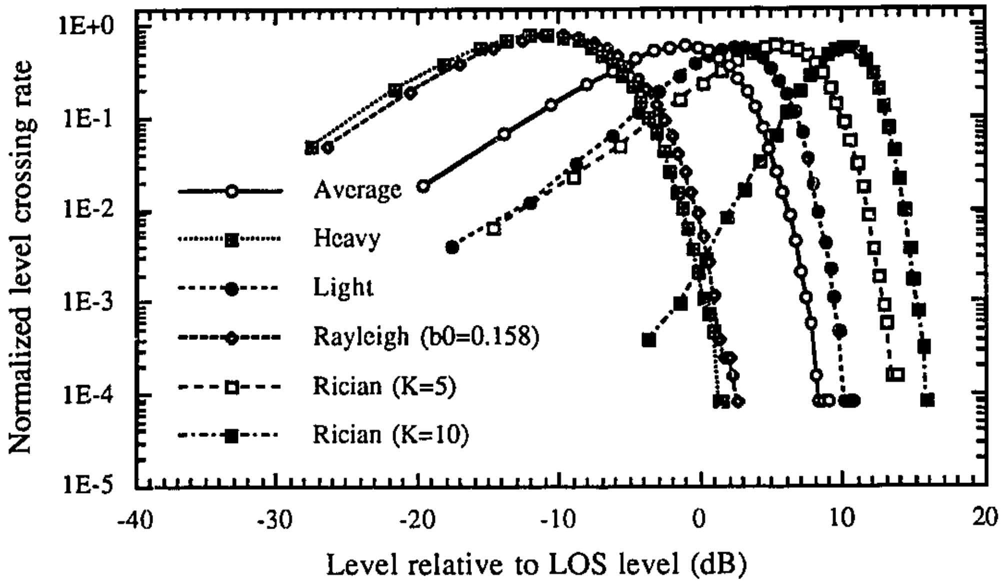

Figure 2.6: Level crossing rate of Rayleigh, Rician and shadowed Rician fading models (BT=0.25).

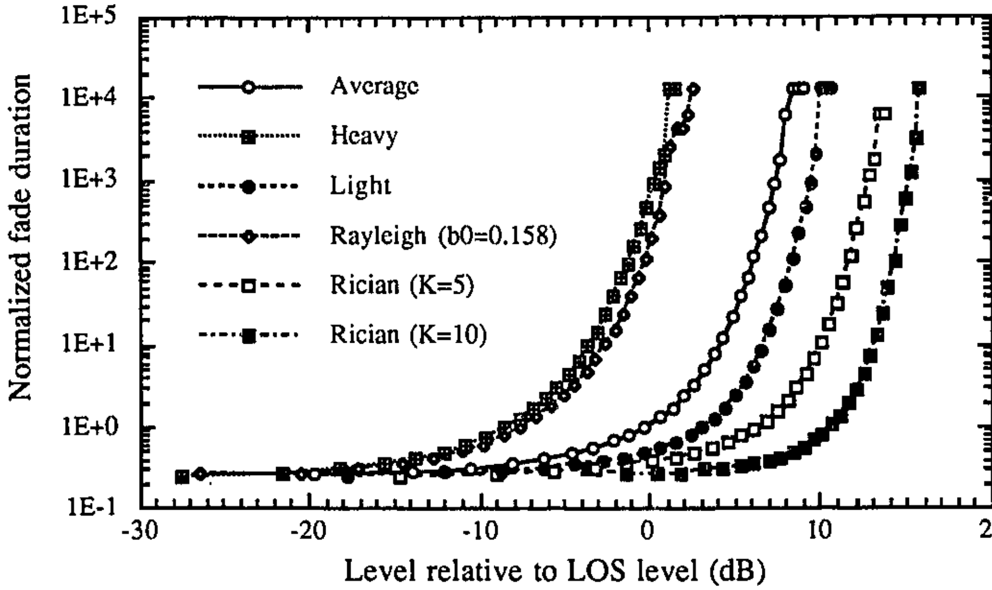

Figure 2.7: Average fade duration of Rayleigh, Rician and shadowed Rician fading models (BT=0.25).

2.10 Summary

The EHF mobile satellite communication channel is characterized by the combined effects of a multiplicative fading process and an additive white Gaussian noise. Depending on the different transmission conditions, the fading process can be represented by the Rayleigh, Rician or log-normally shadowed Rician model. The EHF model parameters are tentatively derived from the existing L-band channel model parameters by using frequency scaling technique. In system analysis and performance evaluation, these channel models play important roles for both theoretical derivation and computer simulation.

Chapter 3

TCM and Its Design Criteria on Fading Channel

3.1 Introduction

The basic idea of trellis-coded modulation (TCM) is to combine the coding and modulation (or decoding and demodulation) processes into one step operation instead of separating them as two independent functions [16]. The significant advantage of TCM is that it can provide coding gain without bandwidth expansion. This technique is especially suited for channels with limitations on bandwidth and power, like the mobile satellite communication channel. The design of a particular TCM scheme is determined by signal mapping and set partitioning. Under different channel conditions, the design criterion for optimum TCM code differs. On fading channels, multiple trellis-coded modulation (MTCM), which is a special form of multidimensional TCM, allows for flexibility in code design as well as a time diversity property. To combat the burst errors usually encountered in a fading channel, interleaving techniques can be used in conjunction with an error correcting code.

In this chapter, we introduce the basic concepts of both conventional and multiple trellis-coded modulation techniques, as well as the corresponding demodulation/decoding method. The TCM code design criteria for the fading channel are presented. TCM schemes that are optimized for fading channels are presented and studied. The advantage of using interleaving is also discussed.

3.2 Conventional Trellis-coded Modulation

The general structure of a rate m/n conventional TCM encoder/modulator is shown in the Figure 3.1. It has m input bits during each output symbol duration. These m bits are grouped into two subsets with m_1 and m_2 bits each. Here $m_1 + m_2 = m$. Through a rate m_1/n_1 convolutional encoder, the m_1 bits are encoded into n_1 bits. The n bits ($n = n_1 + m_2$) are mapped into one of the M-ary ($M = 2^n$) output symbols by certain mapping criteria depending on the different channel applications.

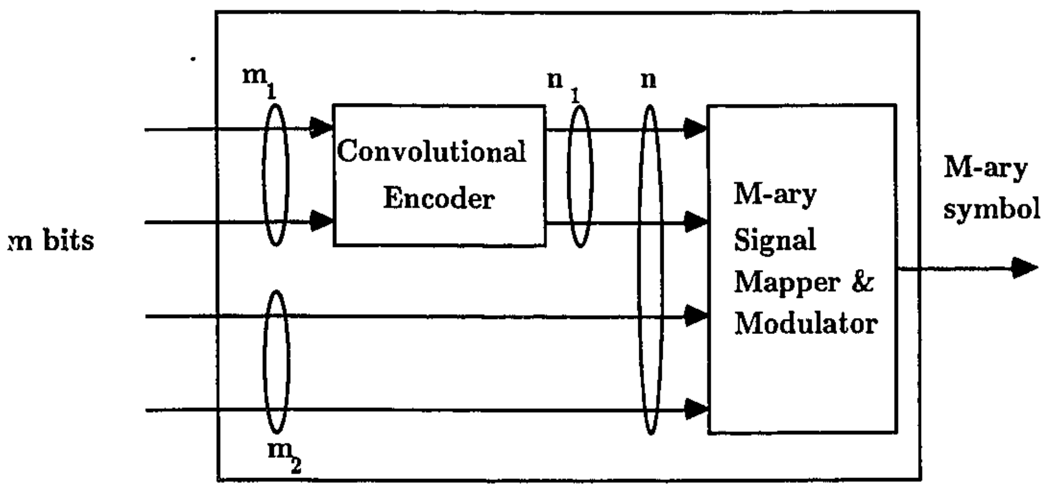

Figure 3.1: General structure of a conventional TCM encoder/modulator.

A conventional TCM coding scheme can be illustrated by a trellis diagram. In the trellis diagram, the encoder states at time index s (referred as stage in a trellis diagram) are the nodes of the trellis. With each output symbol, we associate a branch that stems from each state at stage s and reaches the next state at stage $s + 1$. The branch is labeled by a number that represents the corresponding M-ary symbol in the signal constellation. Parallel transitions occur when two or more branches connect the same pair of nodes. The trellis structure is determined by the coding scheme of a

TCM code. Examples are shown in Figure 3.2 - 3.4: 4-state, 8-state and 16-state rate 2/3 conventional trellis-coded 8-PSK modulation schemes are shown. A TCM coding scheme can also be described by using a state transition table (see Table 3.1, in which a rate 2/3 64-state conventional trellis-coded modulation scheme is specified).

3.3 Multiple Trellis-coded Modulation

Generally, a multiple TCM encoder consists of a rate b/l convolutional encoder and a memoryless signal mapper/modulator as shown in Figure 3.5. In each transmission interval, the multiple TCM encoder first encodes the b input bits to a l bits convolutional codeword, and then maps these encoded l bits into q M-ary output symbols. In the common case, the l binary encoded bits are equally partitioned into q groups. Each group has $\log_2 M$ bits and is mapped into a M-ary output symbol. Therefore the l encoded bits must conform to $l = q \log_2 M$. Here the parameter q is referred as the multiplicity of the MTCM scheme. The q output symbols are selected from an expanded q-tuple M-ary signal set. Such a MTCM encoder has a throughput of b/q bits/symbol and a unity bandwidth expansion when compared to an uncoded system with a $2^{b/q}$ point signal constellation [22].

For instance, a 4/6 4-state multiple trellis-coded 8-PSK modulation scheme is equivalent to rate 2/3 4-state conventional TCM/8-PSK in code rate. In this encoder, four input bits ($b = 4$) are first encoded into six output bits ($l = 6$), then these six bits are partitioned into 2 groups ($q = 2$). Finally these two 3-bit groups are mapped into two 8-PSK symbols and transmitted within four information bit periods.

Similarly, a multiple TCM scheme can be represented by a trellis diagram. The trellis structure consists of 2^b transitions stemming from each state. Each transition is associated with q M-ary output symbols, which are chosen from a q-tuple M-ary signal set in such a way as to meet certain code design and set partitioning criteria. The trellis structure is dependent on the coding scheme of the MTCM code. The trellis diagrams of a rate 4/6 4-state trellis-coded 8-PSK modulation (MTCM/8-PSK) and

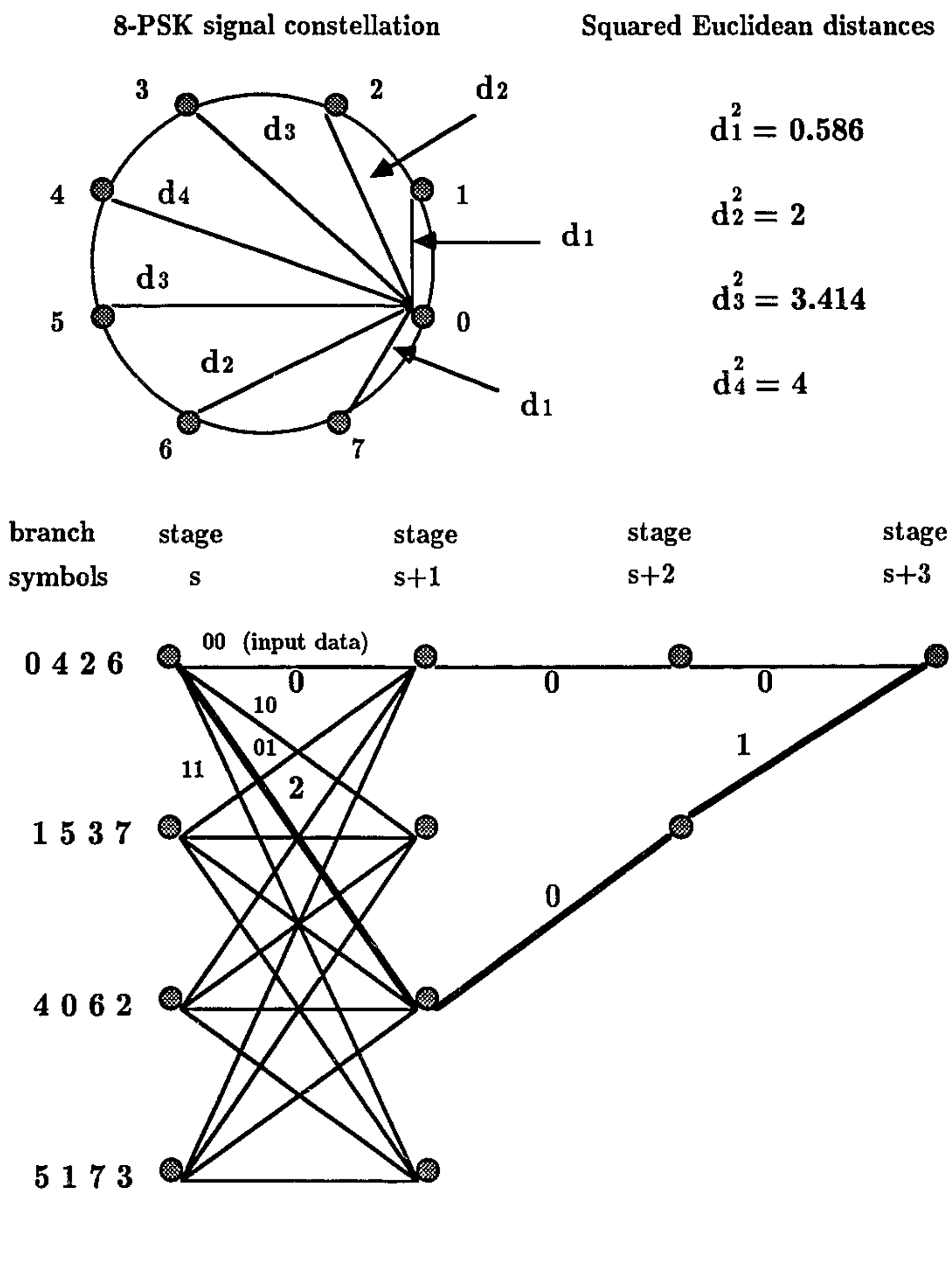

Figure 3.2: Trellis diagram of a conventional rate 2/3 4-state 8-PSK TCM

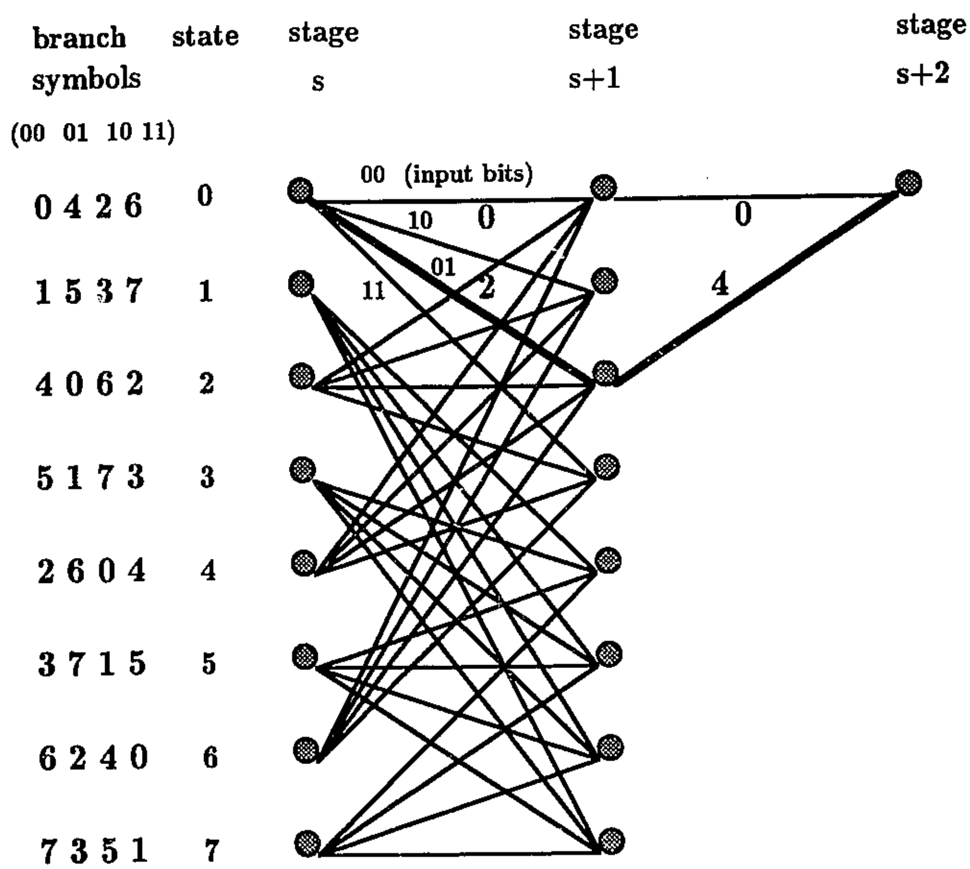

Figure 3.3: Trellis diagram of a conventional rate 2/3 8-state 8-PSK TCM

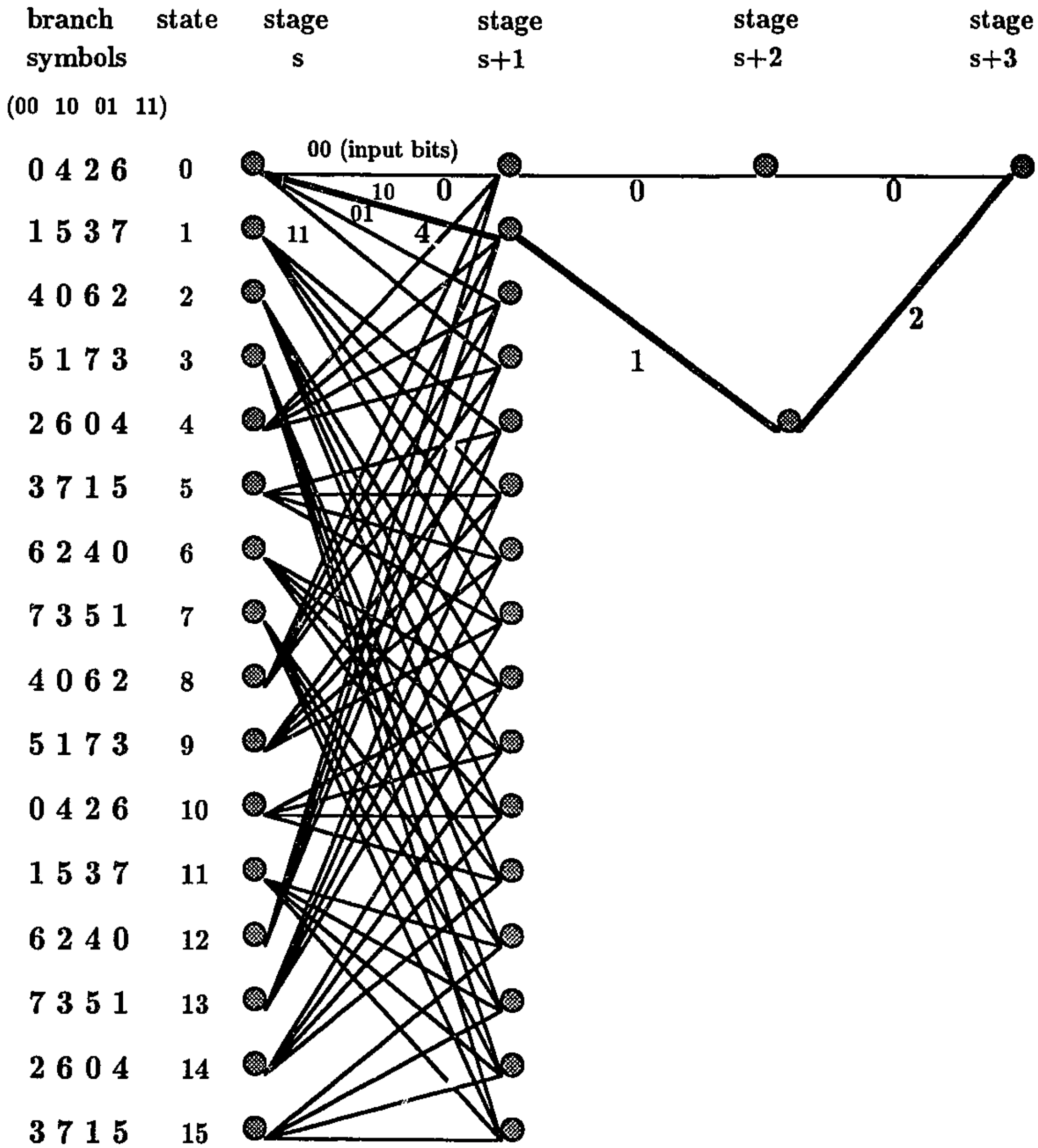

Figure 3.4: Trellis diagram of a conventional rate 2/3 16-state 8-PSK TCM

Table 3.1: Transition table of a conventional rate 2/3 64-state 8-PSK TCM

Current state	Branch symbols*	Next states**	Current state	Branch symbols	Next states
0	0 4 2 6	0 54 15 57	32	0 4 2 6	16 38 31 41
1	1 5 3 7	33 23 46 24	33	1 5 3 7	49 7 62 8
2	0 4 2 6	1 55 14 56	34	0 4 2 6	17 39 30 40
3	1 5 3 7	32 22 47 25	35	1 5 3 7	48 6 63 9
4	0 4 2 6	2 52 13 59	36	0 4 2 6	18 36 29 43
5	1 5 3 7	35 21 44 26	37	1 5 3 7	51 5 60 10
6	0 4 2 6	3 53 12 58	38	0 4 2 6	19 37 28 42
7	1 5 3 7	34 20 45 27	39	1 5 3 7	50 4 61 11
8	0 4 2 6	4 50 11 61	40	0 4 2 6	20 34 27 45
9	1 5 3 7	37 19 42 28	41	1 5 3 7	53 3 58 12
10	0 4 2 6	5 51 10 60	42	0 4 2 6	21 35 26 44
11	1 5 3 7	36 18 43 29	43	1 5 3 7	52 2 59 13
12	0 4 2 6	6 48 9 63	44	0 4 2 6	22 32 25 47
13	1 5 3 7	39 17 40 30	45	1 5 3 7	55 1 56 14
14	0 4 2 6	7 49 8 62	46	0 4 2 6	23 33 24 46
15	1 5 3 7	38 16 41 31	47	1 5 3 7	54 0 57 15
16	0 4 2 6	8 62 7 49	48	0 4 2 6	24 46 23 33
17	1 5 3 7	41 31 38 16	49	1 5 3 7	57 15 54 0
18	0 4 2 6	9 63 6 48	50	0 4 2 6	25 47 22 32
19	1 5 3 7	40 30 39 17	51	1 5 3 7	56 14 55 1
20	0 4 2 6	10 60 5 51	52	0 4 2 6	26 44 21 35
21	1 5 3 7	43 29 36 18	53	1 5 3 7	59 13 52 2
22	0 4 2 6	11 61 4 50	54	0 4 2 6	27 45 20 34
23	1 5 3 7	42 28 37 19	55	1 5 3 7	58 12 53 3
24	0 4 2 6	12 58 3 53	56	0 4 2 6	28 42 19 37
25	1 5 3 7	45 27 34 20	57	1 5 3 7	61 11 50 4
26	0 4 2 6	13 59 2 52	58	0 4 2 6	29 43 18 36
27	1 5 3 7	44 26 35 21	59	1 5 3 7	60 10 51 5
28	0 4 2 6	14 56 1 55	60	0 4 2 6	30 40 17 39
29	1 5 3 7	47 25 32 22	61	1 5 3 7	63 9 48 6
30	0 4 2 6	15 57 0 54	62	0 4 2 6	31 41 16 38
31	1 5 3 7	46 24 33 23	63	1 5 3 7	62 8 49 7

* The 4 symbols correspond to input 00, 01,10 and 11 respectively;
** The 4 states correspond to input 00, 01,10 and 11 respectively.

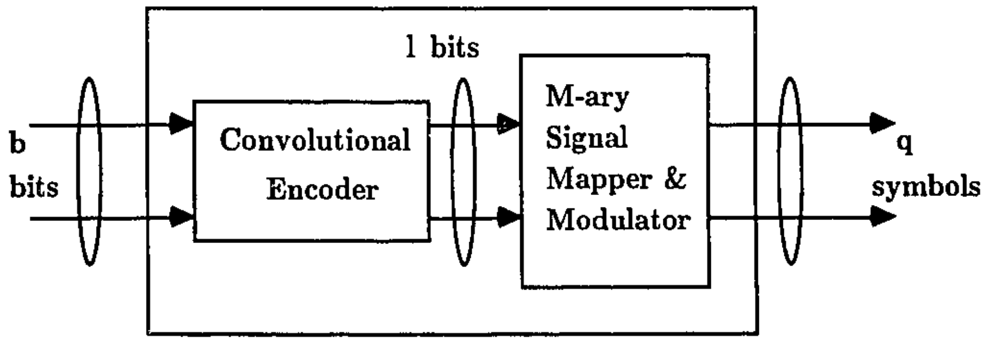

Figure 3.5: General structure of a multiple TCM encoder/modulator.

a rate 3/6 8-state MTCM/8-PSK schemes are shown in Figure 3.6 and 3.7.

3.4 TCM Decoding/Demodulation with Viterbi Algorithm

To decode/demodulate the TCM signal, the most commonly used method is the Viterbi algorithm (VA), which was originally developed for decoding convolutional codes [40]. In applying VA to TCM decoding, the decoder directly takes the Euclidean distance between the received symbol sequence and the possible transmitted symbol sequence as metrics to determine the most likely coded sequence, i.e., the symbol sequence with the smallest squared Euclidean distance from the received sequence is decoded as the transmitted sequence. This algorithm performs the maximum likelihood sequence estimation procedure [39].

The Viterbi algorithm for TCM decoding can be described based on the trellis diagram. The VA decoding process moves sequentially through the trellis, stage by stage, to find the path with the minimum cumulative path metric. As indicated before, the stage represents the time index, and the state transitions occurs between those stages. The VA decoding procedure is briefly stated as following steps.

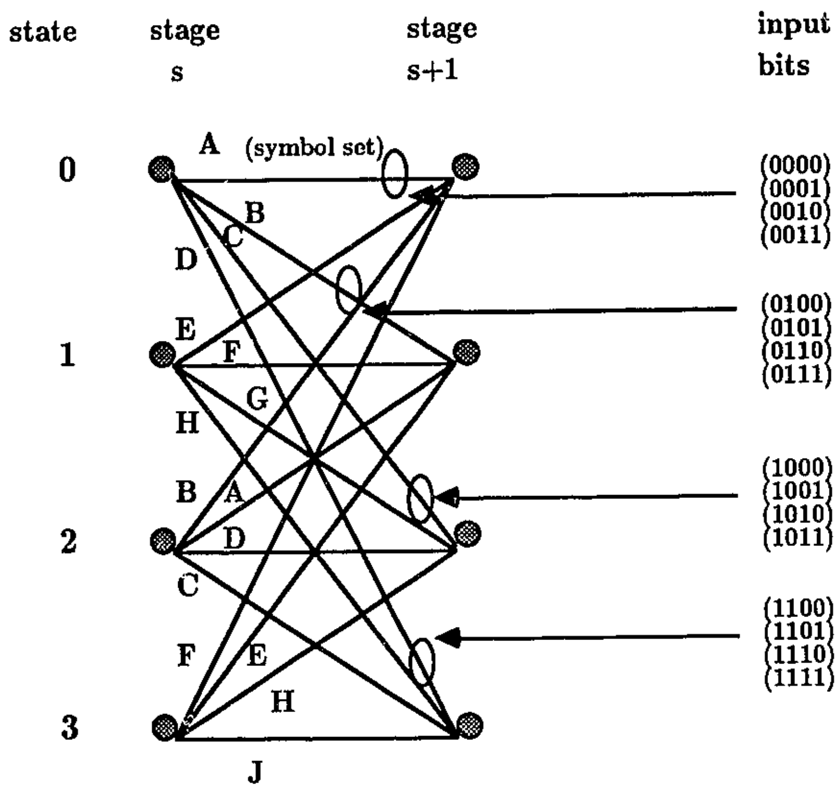

Symbol sets for transitions:

A=	B=	C=	D=
0, 0	1, 5	0, 4	1, 1
2, 2	3, 7	2, 6	3, 3
4, 4	5, 1	4, 0	5, 5
6, 6	7, 3	6, 2	7, 7

E=	F=	G=	H=
0, 2	1, 7	0, 6	1, 3
2, 4	3, 1	2, 0	3, 5
4, 6	5, 3	4, 2	5, 7
6, 0	7, 5	6, 4	7, 1

Figure 3.6: The trellis diagram of a rate 4/6 4-state 8-PSK MTCM

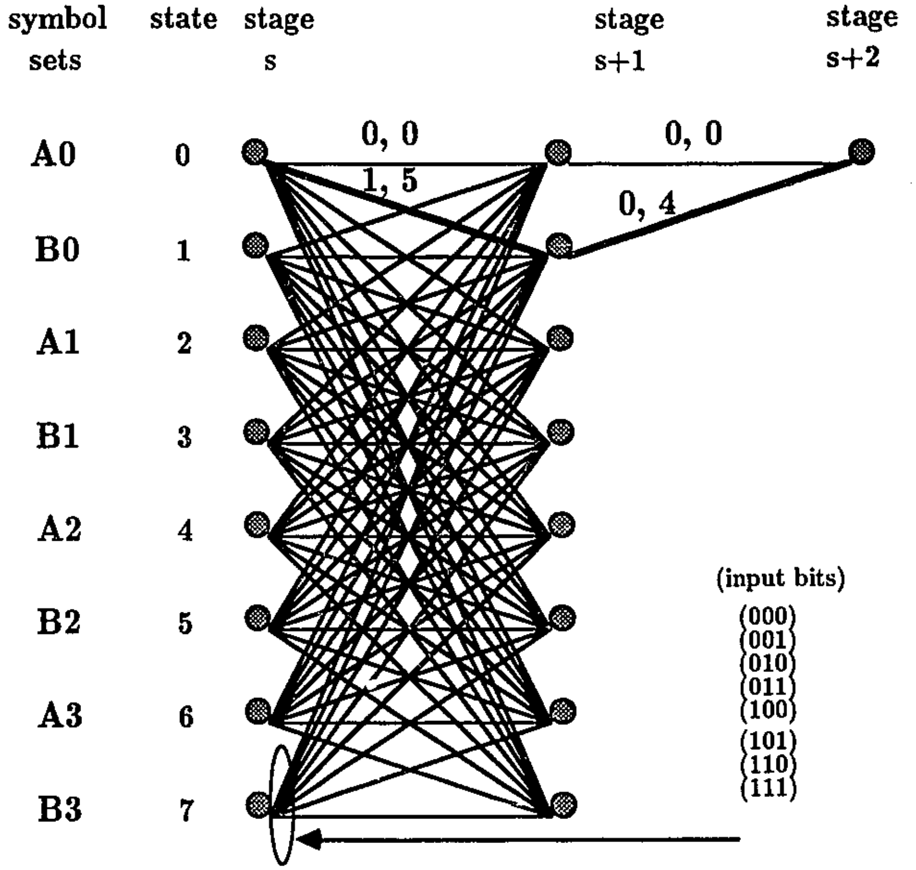

A0=	A1=	A2=	A3=
0, 0	1, 5	2, 2	3, 7
1, 5	2, 2	3, 7	4, 4
2, 2	3, 7	4, 4	5, 1
3, 7	4, 4	5, 1	6, 6
4, 4	5, 1	6, 6	7, 3
5, 1	6, 6	7, 3	0, 0
6, 6	7, 3	0, 0	1, 5
7, 3	0, 0	1, 5	2, 2

B0=	B1=	B2=	B3=
0, 4	1, 1	2, 6	3, 3
1, 1	2, 6	3, 3	4, 0
2, 6	3, 3	4, 0	5, 5
3, 3	4, 0	5, 5	6, 2
4, 0	5, 5	6, 2	7, 7
5, 5	6, 2	7, 7	0, 4
6, 2	7, 7	0, 4	1, 1
7, 7	0, 4	1, 1	2, 6

Figure 3.7: The trellis diagram of a rate 3/6 8-state 8-PSK MTCM

Step 1: Calculate all the branch metrics.

In the trellis diagram of a TCM encoder, every branch associated with a transition is assigned with a symbol for conventional TCM or several symbols for multiple TCM. The branch metric for conventional TCM can be obtained by calculating the Euclidean distance between the received symbol and the corresponding branch symbol at that stage. For multiple TCM, the branch metric is the sum of the Euclidean distances between the received symbols and their corresponding branch symbols within the two stages.

Step 2: Compute the partial metrics for all the paths through each state

The partial metric for a path entering a state is calculated by adding the branch metric, entering the state, to the metric of the connecting survivor path at the preceding stage.

Step 3: For each state, select and store the surviving path and its metric.

The survivor path for each state is simply the path with the smallest partial metric.

Step 4: Repeat step 1, 2, 3 until received sequence ends.

Step 5: Make decision.

By comparing the metrics of all the surviving paths at different states, the surviving path with the smallest metric is decoded as the transmitted sequence.

Due to the time delay and memory problems, it is generally not possible to make decision at the end of the whole transmission. In practice, a truncated Viterbi algorithm is applied. In this case, a decision is made after each truncation length, which is also referred as decoding depth. By using the truncation technique, the Viterbi algorithm loses its optimality and increases the error probability. However, this increase can be negligible if the truncation length is chosen sufficiently large. It is suggested [40] that 5 to 6 times of the code constraint length is needed to reach almost all the theoretical coding gain.

3.5 Design Criteria for TCM on Fading Channels

The design criterion for trellis-coded modulation on the AWGN channel is the maximization of the squared free Euclidean distance d^2_{free} [16, 24].

For fading channels, the criteria for designing an optimum TCM scheme are quite different. Under the conditions of ideal interleaving and deinterleaving, the TCM code designed for a Rician fading channel with small values of K is mainly determined by the following two factors [22]:

- L: length of the shortest error event path, and
- P: branch distance product along the shortest error event path.

For a Rician fading channel with small K, the free Euclidean distance is treated as a secondary consideration. Therefore, under the conditions mentioned above, the optimum TCM code design criteria are to maximize the length L (also referred as effective length) and the product P. L actually represents the number of non-zero distances between the shortest error event path and the correct path while P is the product of all these non-zero distances. At different signal-to-noise ratios (SNR), these two factors have different effects on the performance of a code. At low SNR, the product P has a major impact on the code performance, while at high SNR, the length L plays a more important role.

However, when channel conditions change, the design criteria also change. On the Rician fading channel, if the ratio K is very large, then the performance of the code is affected by all three factors: L, P and d^2_{free}. For the EHF mobile satellite channel, the line-of-sight signal power would be very small due to the severe shadowing effect, which corresponds to small K values. The optimum TCM code design for EHF mobile satellite channels should be guided by the effective length L and the product P.

With respect to the effective length L, the multiple TCM shows some potential advantages in the optimum code design for fading channels, when compared to the conventional TCM. Since the conventional TCM has only one M-ary output symbol corresponding to each trellis branch, the shortest error event path is that error event path with the fewest number of branches having non-zero pairwise distance from the correct path. This also corresponds to the shortest length (in branches) error event in most cases. Therefore, L is just the number of branches on this path [22]. For multiple TCM, there are more than one M-ary symbol corresponding to each trellis branch. The effective length L of the shortest error event path is always equal to, or greater than, the number of branches along the shortest error event path [22].

From the properties of the conventional TCM and multiple TCM, it is reasonable to conclude that the parallel transitions in the trellises should be avoided in the design of a conventional TCM scheme for fading channel, but it is acceptable for the design of multiple TCM. This is because the minimum distance of error event path for conventional TCM scheme is often the parallel path and, thus, the length L has to be equal to 1. This limits the possibilities for the improvement of the error performance. However, a multiple TCM has more than one non-zero Euclidean distance along the parallel transitions and the length L is greater than 1. Therefore, the performance of a multiple TCM is not restricted by the parallel transitions.

Based on above design principles, a set partitioning method for designing an optimum multiple TCM codes used over the Rician fading channel is proposed by Divsalar and Simon [23]. In this method, q fold cartesian products of the same M-ary PSK signal sets are partitioned in such a way that guarantees:

1. Within each of the M partitioned sets, any q-tuple signal element is distinct from other q-tuple signal elements;

2. The minimum product of the Euclidean distance between any q-tuple elements in a partitioned set is maximized.

By using this design method, the shortest error event length L is at least q. This method can also be used to design the conventional TCM codes [34].

3.6 TCM Schemes Considered for EHF Fading Channels

Based on the design criteria mentioned above, six TCM schemes are considered for the EHF mobile satellite channels to investigate the impairment mitigating effect of these codes.

First, a class of the conventional rate 2/3 8-PSK TCM schemes are selected. These include 4-state, 8-state, 16-state and 64-state codes. The corresponding coding schemes are illustrated in Figures 3.2 - 3.4 and Table 3.1. As shown in Figures 3.2, the 4-state TCM does not have parallel transitions. Although this code is designed for AWGN channel, it demonstrates a good performance in Rayleigh fading channel [27]. The other three codes are constructed by maximizing the L and P according to the design criteria for fading channels [25]. The optimum codes of the 8-state and 16-state conventional TCM for fading channel, coincidentally, have the same structures as their counterparts for AWGN in [16], which made these two codes potentially robust on both fading and AWGN channels.

Secondly, two multiple TCM schemes, designed for fading channels by using Divsalar and Simon's set partitioning methods, are considered [23]. These are rate 4/6 4-state multiple 8-PSK TCM and rate 3/6 8-state multiple 8-PSK TCM codes. Their trellis diagrams are shown in Figures 3.6 and 3.7.

According to the code structures of these TCM schemes, the corresponding effective lengths and minimum squared Euclidean distance products (P_{min}) can be calculated, as listed in Table 3.2. In Figures 3.2 - 3.4 and Figure 3.7, the shortest error event paths corresponding to the minimum squared Euclidean distances are indicated. For the rate 4/6 4-state multiple TCM scheme, the shortest error event paths are the parallel transitions.

As shown in Table 3.2, the 64-state conventional TCM has the largest effective length. This indicates that the 64-state TCM should have the best performance

Table 3.2: List of effective length and product of TCM schemes

code	L	P_{min}
TCM2/3_4s	2	1.172
TCM2/3_8s	2	8
TCM2/3_16s	3	4.68
TCM2/3_64s	4	8
MTCM4/6_4s	2	4
MTCM3/6_8s	3	8

among all six TCM schemes on fading channel, especially at high signal-to-noise ratio. The 4-state multiple TCM and the 4-state conventional TCM schemes do have the same effective lengths of 2 but different minimum distance products. A better performance may be expected for the 4-state MTCM in comparison with its conventional counterpart since the former has a larger P_{min}. With the same effective length, the 16-state conventional TCM and the 8-state multiple TCM would demonstrate similar performances.

In the comparison of the different TCM schemes, the bandwidth occupancy and the complexity are the main aspects to be considered. As defined in [23], the normalized complexity per 2-dimensional signal is equal to $2^{\tilde{b}+\lambda}/q$, where the $\tilde{b}$ is the number of encoded input bits, Therefore, $2^{\tilde{b}}$ is the number of paths leaving a given node in the trellis except parallel paths, 2^{λ} is the total number of the encoder states, and q represents the multiplicity of MTCM. For conventional TCM, $q = 1$. The normalized complexity and throughput of the six TCM schemes are listed in Table 3.3.

Table 3.3: Normalized complexity and throughput of TCM schemes

Code	Complexity	Throughput (bits/symbol)
TCM2/3_4s	16	2
TCM2/3_8s	32	2
TCM2/3_16s	64	2
TCM2/3_64s	256	2
MTCM4/6_4s	8	2
MTCM3/6_8s	32	1.5

As is seen in the Table 3.3, the complexity of the TCM schemes increases with the number of encoder states.

3.7 Interleaver and Deinterleaver

In mobile satellite communications, the channel experiences fading and multipath distortions and exhibits burst error characteristics. Many efficient error control codes, such as TCM codes, perform well in correcting independent channel errors. To transform a burst error channel into a channel with statistically independent errors, an effective technique is to interleave the coded information data in a proper way. There are two kinds of interleavers: block interleavers and convolutional interleavers [39]. Both interleavers perform the same function but with different techniques. In this thesis, only block interleavers and deinterleavers are discussed and implemented.

The function of an interleaver is to scramble the order of the transmitted symbols' sequence, while a deinterleaver just performs the reverse operation to restore the original sequence order. A block interleaver can be constructed by using a buffer with D rows and S columns, where D is defined as the interleaving depth and S the interleaving span [21]. Thus the size of the interleaver is $D \times S$ (in symbols). The transmitting coded symbols are read into a memory buffer in successive rows and shifted out of the buffer column by column. At the receiving side, the block deinterleaver, with a buffer of the same size, stores and outputs the received symbols in their original order.

The ideal interleaver/deinterleaver size would be infinity. However, in practice, long transmission delays are intolerable. Practical limits must set for the memory buffer size of interleaver/deinterleaver. The interleaving depth should be chosen depending on the maximum fade depth expected on the channel [21], while the interleaving span should be determined by decoder buffer size. In our simulation, the interleaving depth is chosen as 16 symbols long and the span is 8 symbols wide.

3.8 Summary

Trellis-coded modulation is a power and bandwidth efficient coding/modulation technique, which is specially suited for mobile satellite communications. Compared with conventional TCM, multiple TCM shows some advantages in code design flexibility and the potential of performance improvement on fading channels. The factors that determine the performance of a TCM scheme on fading channel are different from that on the AWGN channel. The code design criterion for the AWGN channel is to maximize the free Euclidean distance d^2_{free}, while for fading channels, the criteria are to maximize the effective length L and the product P. According to the design criteria for fading channels, good TCM schemes are selected for the application on the EHF mobile satellite channels. The Viterbi algorithm is an optimal demodulation method for TCM signals. To tackle the burst error problem, the use of interleavers and deinterleavers provides an effective means.

Chapter 4

Performance Analysis of TCM Systems over Fading Channels

4.1 Introduction

In Chapter 2, the EHF mobile satellite channel is characterized by a fading process combining with AWGN corresponding to certain fading conditions. In this chapter, we discuss how trellis-coded modulation performs over fading channels. The emphasis is on the analysis of factors that determines the performance of TCM scheme over fading channels. These factors are very important to the design of trellis codes as described in Chapter 3. The performance analysis is based on Rician fading channel.

4.2 Coherent M-PSK TCM on Fading Channels

4.2.1 System Description

The baseband system model of a coherently detected trellis-coded modulation over fading channel is illustrated in Figure 4.1. In the block diagram, input data bits are first encoded by a trellis encoder. The encoded bits are then interleaved and properly mapped into M-ary PSK symbols. Passing through the channel, these transmitted symbols are distorted by the fading process and additive white Gaussian noise. At receiver side, the received symbols are deinterleaved and decoded by a soft decision

Viterbi decoder. To achieve a better performance, channel state information (CSI) may also be provided to the Viterbi decoder to optimize the decoding metrics. The channel state information provides a measure of the fading amplitude obtained from the channel and can be used as additional information for the Viterbi decoding procedure. In practice, dual pilot tone calibration technique, in which two pilot tones of same power are inserted on both sides of main data signal spectrum, can be implemented to assist a robust carrier recovery [41, 42]. The channel state information can therefore be obtained from the power of received pilot tones.

4.2.2 Performance Analysis

In the system model described above, several important assumptions are made for simplifying the theoretical performance analysis. First, we assume that perfect coherent detection is achieved. Under this condition, there will be no signal phase distortion and only the amplitude fading effect is involved. Secondly, theoretically infinite interleaving and deinterleaving are assumed so that the channel can be viewed as memoryless one. Thirdly, both encoded signal and fading amplitude over a symbol interval can be represented by a single sample.

Let us express $\mathbf{x}$ as the transmitted M-ary PSK symbol sequence of length L from the TCM transmitter to channel, $\mathbf{y}$ as the channel output sequence and $\hat{\mathbf{x}}$ ($\hat{\mathbf{x}} \neq \mathbf{x}$) as the decoded sequence from the Viterbi decoder. At time k, there is

$$y_k = r_k x_k + n_k \tag{4.1}$$

where r_k represents the normalized fading amplitude and n_k is a complex additive Gaussian white noise with zero mean and variance σ^2 in each dimension. The probability that the decoder selects $\hat{\mathbf{x}}$ as the decoded sequence instead of $\mathbf{x}$, when $\mathbf{x}$ is transmitted, is defined as the pairwise error probability. It is expressed as [25, 35]

$$P(\mathbf{x} \rightarrow \hat{\mathbf{x}}) = Pr[m(\mathbf{y}, \hat{\mathbf{x}}) \leq m(\mathbf{y}, \mathbf{x}) | \mathbf{x}] \tag{4.2}$$

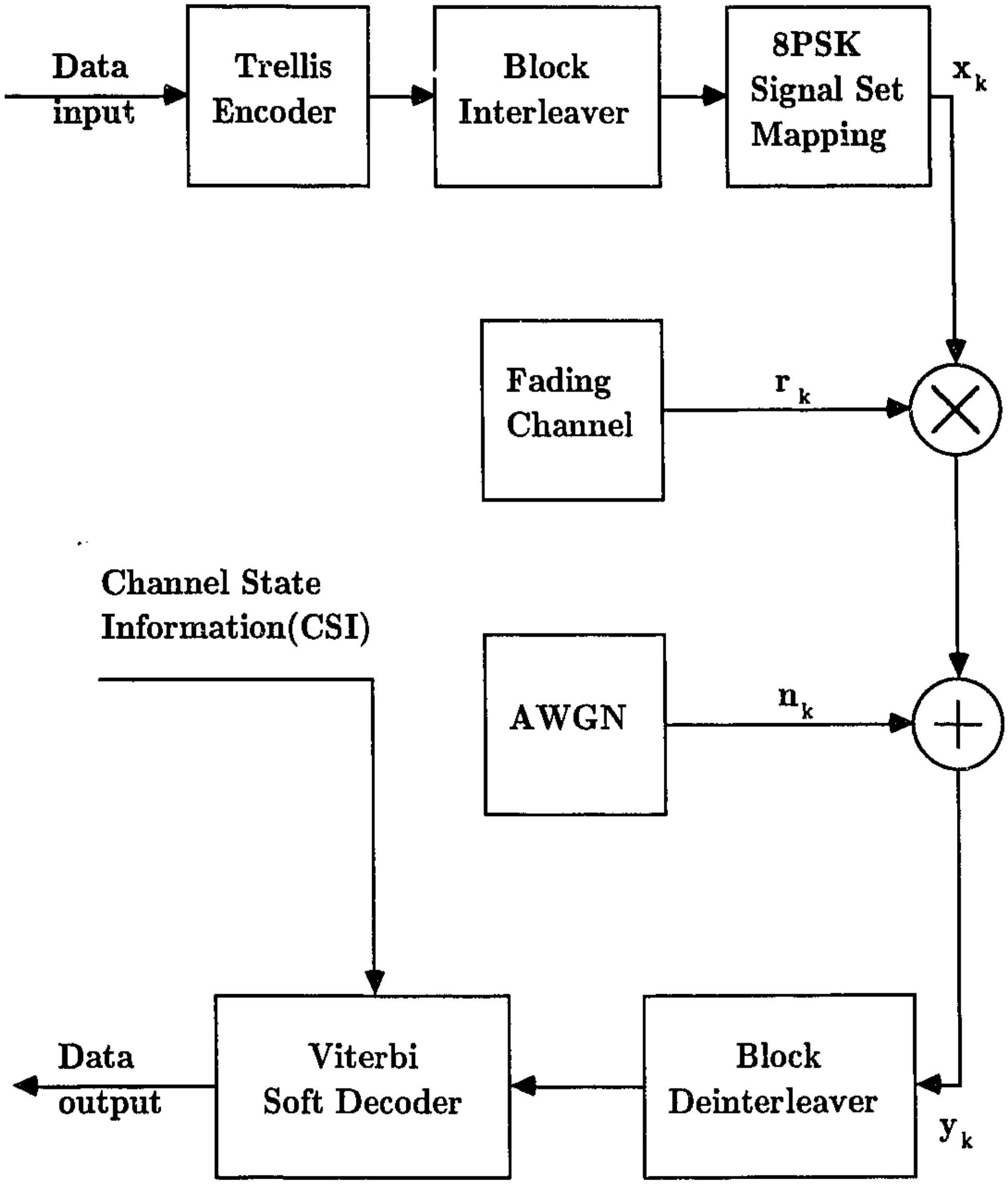

Figure 4.1: Baseband system diagram for coherent trellis-coded modulation over EHF mobile satellite channel

where

$$m(\mathbf{y}, \hat{\mathbf{x}}) = \sum_{k=1}^{L} m(y_k, \hat{x}_k) \tag{4.3}$$

$$m(\mathbf{y}, \mathbf{x}) = \sum_{k=1}^{L} m(y_k, x_k) \tag{4.4}$$

$$m(y_k, x_k) = \begin{cases} -|y_k - r_k x_k|^2, & \text{with CSI;} \\ -|y_k - x_k|^2, & \text{no CSI} \end{cases} \tag{4.5}$$

are the decoding metric depending on the availability of channel state information. Under the assumed conditions of the system model and by using union bound, the bit error probability of this system is upper bounded by [22]

$$P_b \leq \sum_{\mathbf{x}, \hat{\mathbf{x}}} \sum_{\in C} a(\mathbf{x}, \hat{\mathbf{x}}) P(\mathbf{x}) P(\mathbf{x} \rightarrow \hat{\mathbf{x}}) \tag{4.6}$$

where $a(\mathbf{x}, \hat{\mathbf{x}})$ represents the number of information bit errors that occur when symbol sequence $\mathbf{x}$ is sent and symbol sequence $\hat{\mathbf{x}}$ is decoded, $P(\mathbf{x})$ is a priori probability of transmitting $\mathbf{x}$, and C is the set of all possible coded sequences.

In order to evaluate the average bit error probability P_b, one has to determine the pairwise error probability $P(\mathbf{x} \rightarrow \hat{\mathbf{x}})$, which depends on the choice of the decoding metric and the presence of channel state information.

The Rician channel model discussed in Chapter 2 is considered. The Rayleigh fading model condition can simply be viewed as a special case of Rician model by letting the K-factor be equal to zero. The probability density function of the normalized Rician fading amplitude r is given by

$$P(r) = \begin{cases} 2r(K+1)\exp[-(K+1)r^2 - K] I_0(2r\sqrt{K(K+1)}), & r \geq 0; \\ 0, & r < 0. \end{cases} \tag{4.7}$$

A. Ideal Channel State Information

Here we assume that perfect CSI is provided and a Gaussian decoding metric is used. By substituting (4.1) into (4.2) and applying Chernoff bounding technique, the conditioned pairwise error probability is found to be [21]

$$P(\mathbf{x} \to \hat{\mathbf{x}}|\mathbf{r}) \leq \exp[-\frac{E_s}{4N_0} \sum_{k \in \eta} r_k^2 |x_k - \hat{x}_k|^2] \tag{4.8}$$

where r_k represents the normalized fading amplitude at kth symbol interval, E_s/N_0 stands for the ratio of M-ary PSK symbol energy to spectral density of noise, η is the set of all k for which $x_k \neq \hat{x}_k$, and $|x_k - \hat{x}_k|^2$ is defined as the squared pairwise distance that refers to the squared Euclidean distance between corresponding symbols on the compared paths.

By averaging the conditioned pairwise error probability (4.8) over the probability density function (4.7), the pairwise error probability is upper bounded by [22]

$$P(\mathbf{x} \to \hat{\mathbf{x}}) \leq \prod_{k \in \eta} \frac{K+1}{K+1+\frac{\bar{E}_s}{4N_0}|x_k - \hat{x}_k|^2} \exp[-\frac{K\frac{\bar{E}_s}{4N_0}|x_k - \hat{x}_k|^2}{K+1+\frac{\bar{E}_s}{4N_0}|x_k - \hat{x}_k|^2}] \tag{4.9}$$

where $\bar{E}_s/N_0$ is the ratio of average symbol energy to noise spectral density. For sufficiently high signal to noise ratio, i.e. $\bar{E}_s/N_0 \gg K$, the formula (4.9) can be simplified as

$$P(\mathbf{x} \to \hat{\mathbf{x}}) \leq \prod_{k \in \eta} \frac{e^{-K}}{\frac{\bar{E}_s}{N_0}\frac{|x_k - \hat{x}_k|^2}{4(K+1)}} = \frac{4^{L_\eta}[(K+1)e^{-K}]^{L_\eta}}{(\frac{\bar{E}_s}{N_0})^{L_\eta} \prod_{k \in \eta} |x_k - \hat{x}_k|^2} \tag{4.10}$$

where L_η is defined as the length of the error event path and its value is equal to the number of elements in the set η.

Therefore, the average bit error probability is bounded by

$$P_b \leq \sum_{\mathbf{x}, \hat{\mathbf{x}}} \sum_{\in C} a(\mathbf{x}, \hat{\mathbf{x}}) P(\mathbf{x}) \frac{4^{L_\eta}[(K+1)e^{-K}]^{L_\eta}}{(\frac{\bar{E}_s}{N_0})^{L_\eta} \prod_{k \in \eta} |x_k - \hat{x}_k|^2}. \tag{4.11}$$

B. No Channel State Information

With no CSI, we assume coherent detection system using Gaussian decoding metric. The corresponding expression for the pairwise error probability was derived by Divsalar and Simon in [22, 34]. For $\bar{E}_s/N_0 \gg K$, there is

$$P(\mathbf{x} \to \hat{\mathbf{x}}) \leq \frac{(\frac{2e}{L_\eta})^{L_\eta}}{(\frac{\bar{E}_s}{N_0})^{L_\eta}} (\prod_{k \in \eta} \frac{|x_k - \hat{x}_k|^2}{(\sum_{k \in \eta} |x_k - \hat{x}_k|^2)^{\frac{1}{2}}})^{-2} [(K+1)e^{-K}]^{L_\eta}. \quad (4.12)$$

The upper bound for bit error probability is given by

$$P_b \leq \sum_{\mathbf{x}, \hat{\mathbf{x}}} \sum_{\in C} a(\mathbf{x}, \hat{\mathbf{x}}) P(\mathbf{x}) \frac{(\frac{2e}{L_\eta})^{L_\eta}}{(\frac{\bar{E}_s}{N_0})^{L_\eta}} (\prod_{k \in \eta} \frac{|x_k - \hat{x}_k|^2}{(\sum_{k \in \eta} |x_k - \hat{x}_k|^2)^{\frac{1}{2}}})^{-2} [(K+1)e^{-K}]^{L_\eta}. \quad (4.13)$$

To evaluate the (4.11) and (4.13), a specific TCM coding scheme must be analyzed. However, looking at the P_b bounds of (4.11) and (4.13), we find that either of them is dominated by the term in summation which has the smallest number of elements in η. This corresponding path is referred to the shortest error event path and its length is represented by the effective length L. Thus, the generalized average bit error probability is approximately equal to [34]

$$P_b \cong \tfrac{1}{b} \beta (\tfrac{(K+1)e^{-K}}{\bar{E}_s/N_0})^L, \quad \bar{E}_s/N_0 \gg K \quad (4.14)$$

where b is the number of input bits to trellis encoder, β is a constant that is determined by the distance structure of a specific TCM coding scheme. Corresponding expressions of β are

$$\beta = \begin{cases} 4^L [\prod_{k \in \eta} |x_k - \hat{x}_k|^2]^{-1}, & \text{with CSI;} \\ (\frac{2e}{L})^L (\prod_{k \in \eta} \frac{|x_k - \hat{x}_k|^2}{(\sum_{k \in \eta} |x_k - \hat{x}_k|^2)^{\frac{1}{2}}})^{-2}, & \text{no CSI.} \end{cases} \quad (4.15)$$

Independent of CSI, the average bit error probability P_b in (4.14) varies inversely with $(\bar{E}_s/N_0)^L$, which shows some kind of diversity effect. L denotes the number of the implied diversity. Therefore, to achieve the optimal performance on Rician fading channel, it is important to design the TCM code with a maximum L. In addition, as shown in 4.15, the code design should also minimize β. This corresponds to maximizing the squared branch distance product of the shortest error event path $|x_k - \hat{x}_k|^2$, which is denoted as P in Chapter 3. This indicates that the design criteria for optimum TCM scheme on the Rician fading channel are to maximize both L and P.

C. No Interleaving and Deinterleaving

As we consider the system with coherent detection and a Gaussian decoding metric, but without interleaver and deinterleaver, the assumption of a memoryless channel condition is no longer valid. In this case, the average bit error probability is approximately [34]

$$P_b \cong C1 \frac{K+1}{K+1+d_{free}^2(\frac{\bar{E}_s}{4N_0})} \exp(-K \frac{d_{free}^2(\frac{\bar{E}_s}{4N_0})}{K+1+d_{free}^2(\frac{\bar{E}_s}{4N_0})}) \tag{4.16}$$

where $C1$ is a constant and d_{free}^2 is the squared free Euclidean distance of the TCM code

$$d_{free}^2 = \min_{\mathbf{x},\hat{\mathbf{x}}} \sum_{k\in\eta} |x_k - \hat{x}_k|^2. \tag{4.17}$$

For large $\bar{E}_s/N_0$, (4.16) can be simplified as

$$P_b \cong 4C1 \frac{K+1}{d_{free}^2(\frac{\bar{E}_s}{N_0})} e^{-K}. \tag{4.18}$$

In (4.18), the changing rate of P_b varies inversely with $\bar{E}_s/N_0$ if the TCM coding schemes keep unchanged. It is noted that, without interleaver and deinterleaver, the implicit diversity of a TCM code is equal to one and the performance is determined by maximizing the squared free Euclidian distance. Therefore, the trellis-coded modulation can not fully exhibit its potential without interleaving/deinterleaving.

4.3 Differential M–PSK TCM over Fading Channels

In Section 4.2, the discussion on coherent TCM systems is based on the idealistic assumption that perfect synchronization is achieved. To achieve this, a carrier recovery method must be used to track the synchronization reference. However, in practice, the tracking of the carrier reference is sometimes difficult, especially during the deep fades. In such cases, a differential TCM system might be a preferable choice.

4.3.1 System Description

As shown in Figure 4.2, the baseband model for differentially detected M–PSK TCM system over fading channels is similar to that for coherent TCM systems which is illustrated in Figure 4.1. The main difference between them is the addition of differential encoder and detector. As usual, the input bits are first encoded, interleaved and properly mapped into M-ary PSK symbols. Then, these M-PSK symbols are differentially encoded before being transmitted over the channel. Finally, at the receiving end, these corrupted symbols are differentially detected, deinterleaved and softly decoded. Over the channel, the transmitted signal suffers distortion from both amplitude and phase. Since carrier recovery technique is not needed in this case, there is no CSI available for Viterbi decoder.

4.3.2 Performance Analysis

Again for simplification, the assumption of infinite interleaving and deinterleaving is made. Since the optimum decoding metric derived by Divsalar and Simon in [22, 34] for differential M-PSK TCM on fading channels is quite complicated to implement and that it is rather difficult to analyze the error performance by using the optimum metric, the squared Euclidean distance is used as the decoding metric. Although this metric is only a suboptimum one for decoding on fading channels, its simplicity

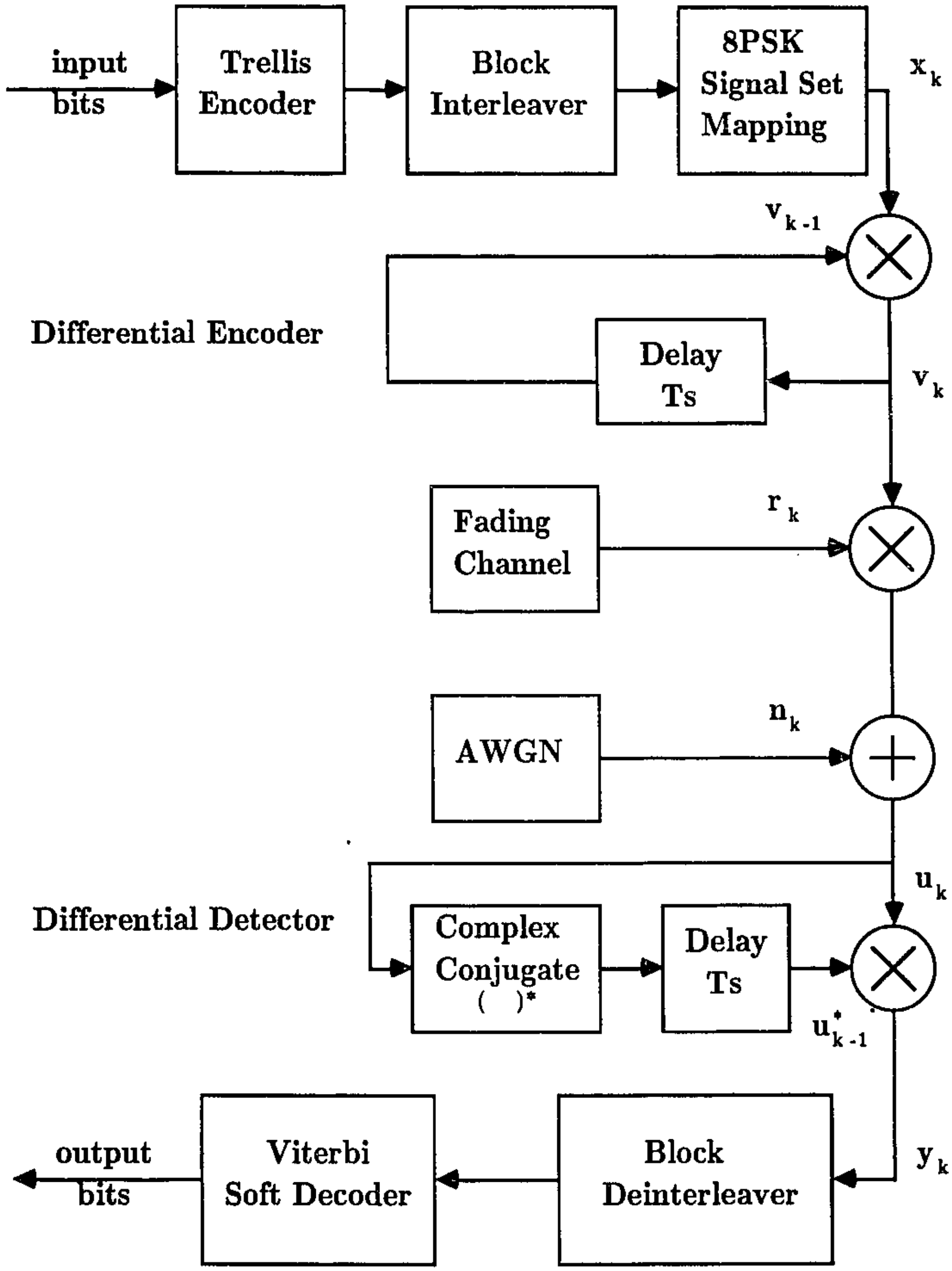

Figure 4.2: Baseband system diagram for differential trellis-coded modulation over EHF mobile satellite channel

and easy implementation are of much practical interest. From the system model, the analytical representations of the signals at different stages are expressed as follows. The transmitted signal from differential encoder is

$$v_k = x_k v_{k-1}. \tag{4.19}$$

At receiving end, received signal from channel becomes

$$u_k = r_k v_k + n_k. \tag{4.20}$$

The signal at the output of the differential detector is

$$y_k = u_{k-1}^* u_k = r_{k-1}^* r_k x_k + \text{noise terms} \tag{4.21}$$

where r_k and n_k represent the fading amplitude and white Gaussian noise at time k respectively.

Following similar procedures described in section 4.2.2, analogue expressions of the pairwise error probability and bit error upper bound for the differential M-PSK TCM system over Rician fading channel for sufficiently high SNR are derived in [22, 34].

A. On Slow Fading Channels

Since in a slow fading channel the speed variation of the fading process is much slower than the signal transmission rate, it is reasonable to assume that $r_k = r_{k-1}$. Under this assumption, there is

$$P(\mathbf{x} \to \hat{\mathbf{x}}) \le \prod_{k \in \eta} \frac{e^{-K}}{\frac{\bar{E}_s}{N_0} \frac{|x_k - \hat{x}_k|^2}{8(K+1)}} = \frac{8^{L_\eta}[(K+1)e^{-K}]^{L_\eta}}{(\frac{\bar{E}_s}{N_0})^{L_\eta} \prod_{k \in \eta} |x_k - \hat{x}_k|^2} \tag{4.22}$$

and

$$P_b \le \sum_{\mathbf{x}, \hat{\mathbf{x}}} \sum_{\in C} a(\mathbf{x}, \hat{\mathbf{x}}) P(\mathbf{x}) \frac{8^{L_\eta}[(K+1)e^{-K}]^{L_\eta}}{(\frac{\bar{E}_s}{N_0})^{L_\eta} \prod_{k \in \eta} |x_k - \hat{x}_k|^2}. \tag{4.23}$$

The approximate P_b at high signal-to-noise ratio is

$$P_b \cong \frac{8^L}{b} [\prod_{k \in \eta} |x_k - \hat{x}_k|^2]^{-1} (\frac{(K+1)e^{-K}}{\bar{E}_s/N_0})^L, \quad \bar{E}_s/N_0 \gg K. \tag{4.24}$$

This expression of P_b has similar form to that of coherent system illustrated in (4.14) and (4.15). It is obvious that the performance of the differential TCM on slow fading Rician channel is also determined by the effective length L and the product P.

B. On Fast Fading Channels

On a fast fading channel, the fading process varies rapidly over transmission signal intervals. In this case, the r_{k-1} and r_k are considered to be correlated. The expression and computation of the pairwise error probability for the Rician fading channel are very complicated as described in [34]. However, for the Rayleigh channel, a special case of the Rician channel with $K = 0$, the asymptotic pairwise error probability and bit error probability bound are given by [34]

$$P(\mathbf{x} \rightarrow \hat{\mathbf{x}}) \leq \prod_{k \in \eta} \frac{1}{1 + \frac{|x_k - \hat{x}_k|^2}{4} \frac{\xi^2}{(1-\xi^2)}} \tag{4.25}$$

and

$$P_b \leq \sum \sum_{\mathbf{x}, \hat{\mathbf{x}} \in C} a(\mathbf{x}, \hat{\mathbf{x}}) P(\mathbf{x}) \prod_{k \in \eta} \frac{1}{1 + \frac{|x_k - \hat{x}_k|^2}{4} \frac{\xi^2}{(1-\xi^2)}} \tag{4.26}$$

where ξ is a constant and $0 \leq |\xi| < 1$.

From the upper bounds (4.25) and (4.26), we note that the expression of the pairwise error probability does not related to the $\bar{E}_s/N_0$. This means that despite the increase of the signal to noise ratio, there is always an irreducible error probability.

4.4 Asymptotic Performances of the Considered TCM Schemes

Based on the expressions of (4.14), (4.15) and (4.24) as well as the TCM code structures described in Chapter 3, the asymptotic results on average bit error probability at high $\bar{E}_s/N_0$ can be calculated. For performance comparison, the asymptotic BERs for the six considered TCM schemes on Rician fading channel are simplified as functions of K and $\bar{E}_b/N_0$.

4.4.1 BERs for Coherent TCM Systems

Under the condition of ideal interleaving, the bit error probabilities of the coherent TCM systems on Rician fading channel can be approximately expressed as follows.

1. Rate 2/3 4-state conventional TCM scheme

$$P_b \cong \begin{cases} 1.71(\frac{(K+1)e^{-K}}{E_b/N_0})^2, & \text{with CSI;} \\ \\ 4.50(\frac{(K+1)e^{-K}}{E_b/N_0})^2, & \text{no CSI.} \end{cases} \tag{4.27}$$

2. Rate 2/3 8-state conventional TCM scheme

$$P_b \cong \begin{cases} 0.25(\frac{(K+1)e^{-K}}{E_b/N_0})^2, & \text{with CSI;} \\ \\ 0.52(\frac{(K+1)e^{-K}}{E_b/N_0})^2, & \text{no CSI.} \end{cases} \tag{4.28}$$

3. Rate 2/3 16-state conventional TCM scheme

$$P_b \cong \begin{cases} 0.85(\frac{(K+1)e^{-K}}{E_b/N_0})^3, & \text{with CSI;} \\ \\ 4.83(\frac{(K+1)e^{-K}}{E_b/N_0})^3, & \text{no CSI.} \end{cases} \tag{4.29}$$

4. Rate 2/3 64-state conventional TCM scheme

$$P_b \cong \begin{cases} 1.0(\frac{(K+1)e^{-K}}{E_b/N_0})^4, & \text{with CSI;} \\ \\ 6.82(\frac{(K+1)e^{-K}}{E_b/N_0})^4, & \text{no CSI.} \end{cases} \tag{4.30}$$

5. Rate 4/6 4-state multiple TCM scheme

$$P_b \cong \begin{cases} 0.50(\frac{(K+1)e^{-K}}{E_b/N_0})^2, & \text{with CSI;} \\ \\ 0.92(\frac{(K+1)e^{-K}}{E_b/N_0})^2, & \text{no CSI.} \end{cases} \tag{4.31}$$

6. Rate 3/6 8-state multiple TCM scheme

$$P_b \cong \begin{cases} 0.79(\frac{(K+1)e^{-K}}{E_b/N_0})^3, & \text{with CSI;} \\ \\ 4.7(\frac{(K+1)e^{-K}}{E_b/N_0})^3, & \text{no CSI.} \end{cases} \tag{4.32}$$

As demonstrated by the above expressions, the bit error probabilities of the considered coherent TCM schemes at high $\bar{E}_b/N_0$ are determined by their effective lengths. Among these TCM schemes, the rate 2/3 64-state conventional TCM has the lowest bit error probabilities due to its largest effective length $L = 4$.

From (4.27) - (4.32), it is observed that the performances of the TCM schemes are improved with CSI. By comparing (4.27) and (4.31), it is shown that the 4-state multiple TCM has a better performance than the 4-state conventional TCM scheme. The performance of the 16-state conventional TCM is almost the same as that of the 8-state multiple TCM scheme as shown in (4.29) and (4.32).

4.4.2 BERs for Differential TCM systems

For differential TCM systems with ideal interleaving and deinterleaving, the approximations of the bit error probabilities on the slow Rician fading channel are given by the following expressions.

1. Rate 2/3 4-state conventional TCM scheme

$$P_b \cong 6.83(\frac{(K+1)e^{-K}}{\bar{E}_b/N_0})^2. \tag{4.33}$$

2. Rate 2/3 8-state conventional TCM scheme

$$P_b \cong 1.0(\frac{(K+1)e^{-K}}{\bar{E}_b/N_0})^2. \tag{4.34}$$

3. Rate 2/3 16-state conventional TCM scheme

$$P_b \cong 6.84(\frac{(K+1)e^{-K}}{\bar{E}_b/N_0})^3. \tag{4.35}$$

4. Rate 2/3 64-state conventional TCM scheme

$$P_b \cong 16(\frac{(K+1)e^{-K}}{\bar{E}_b/N_0})^4. \tag{4.36}$$

5. Rate 4/6 4-state multiple TCM scheme

$$P_b \cong 2.0(\frac{(K+1)e^{-K}}{\bar{E}_b/N_0})^2. \tag{4.37}$$

6. Rate 3/6 8-state multiple TCM scheme

$$P_b \cong 6.3(\frac{(K+1)e^{-K}}{\bar{E}_b/N_0})^3. \tag{4.38}$$

When compared to coherent case, the BER performance obtained with differential TCM is slightly worse than that of coherent TCM without CSI. The bit error probabilities of the differential TCM schemes on slow fading channels at high $\bar{E}_b/N_0$ are also determined by their effective lengths. As shown in (4.33) - (4.38), on slow fading channel, the 64-state conventional TCM has the best performance. The 4-state multiple TCM performs better than the 4-state conventional TCM. Similar BER performances are found for the 16-state conventional and 8-state multiple TCM schemes.

4.5 Summary

In this chapter, the performances of coherent and differential TCM systems over Rician fading channel are analyzed in the form of asymptotic expressions. From these expressions, it is obvious that over the Rician fading channel the performance of TCM with interleaving/deinterleaving is mainly determined by the length of the shortest error event path L and the branch distance product $\prod_{k\in\eta}|x_k - \hat{x}_k|^2$ along that path. These results lead to the design criteria for TCM on fading channel as described in Chapter 3. However, without interleaving/deinterleaving, the performance of the TCM is determined by the free Euclidean distance. On the fast Rayleigh fading condition, the differential TCM systems always have the irreducible error probabilities. To compare the performances of the considered TCM schemes on Rician fading channel, the asymptotic bit error probabilities are derived in the functions of K and $\bar{E}_b/N_0$.

Chapter 5

Communication System Simulation

5.1 Introduction

To assess the performance of a communication system, there are two commonly used methods in addition to on-site testing. The first one consists in deriving the mathematical solutions to determine the system performance bounds. The other relies on computer simulation to evaluate the system performance. As described in Chapter 4, the derivation of the analytical results for TCM system is quite tedious, especially when the number of states in the trellis diagram is large. In such a case, a computer simulation constitutes a more expedient way to determine the performance.

A general description of the simulation platform used is given in the next section. The third section describes the simulation of the different components of the EHF mobile satellite communication system. It also provides the design and programming details of the key system modules.

5.2 Overview of the Computer Simulation Tool

The EHF mobile satellite communication system is simulated by using a computer simulation tool called Signal Processing WorkSystem (SPW), which is a software package developed by Comdisco System Inc. for digital signal processing and communication system simulation [43].

SPW software provides an interactive environment for simulation design and analysis with graphical capabilities. It consists of a collection of general-purpose DSP and communication function blocks. Each of these blocks performs a signal processing operation that corresponds to a specific system device or function. One of the advantages to use SPW is that user can program his own function blocks in C language and build them into the SPW block library. A simulation system can be established by using both the SPW function blocks and the user-defined blocks. In SPW platform, the simulation process is conducted in time domain.

The SPW framework consists of two separate programs, Block Diagram Editor (BDE) and Signal Display Editor (SDE). BDE is used to construct and edit the block diagrams of a simulated system. All the necessary function blocks or modules and their connections are graphically displayed on the screen of the workstation. After editing, this finished block diagram can be simulated or used as another module to build more complicated systems. The results of a simulation can be viewed by using SDE. The SDE can also be used to perform signal analysis and transformation in both time and frequency domains.

5.3 Simulation of the Communication System Components

There are several basic considerations for the simulation systems. It is assumed that system is perfectly synchronized and there is no intersymbol interference. To reduce the time for running the simulations, only one sample is used to represent a transmitted 8-PSK symbol. Corresponding to each 8-PSK symbol, the fading and AWGN processes are represented respectively by one sample following the desired distribution.

In our simulation, two types of systems, coherent and differential TCM 8-PSK systems, are implemented. As shown in Figures 4.1 and 4.2, their baseband models are primarily made up by modules for the encoders, channels, interleavers, deinterleavers, Viterbi decoders, differential encoders and detectors. The representative SPW block diagrams of the coherent and differential TCM baseband systems are given in Figures A.5 - A.8 (see Appendix A).

In coherent TCM system, perfect coherent detection is assumed, and therefore only amplitude distortion is considered. Taking into account different conditions such as channel models, conventional or multiple TCM, number of trellis states, decoding with or without the reference of CSI, as well as the utilization of interleaving, there are several communication system configurations. Each configuration also has its own parameters such as truncation length and interleaver size. In differential TCM system, both amplitude and phase distortions are included in the performance evaluations. CSI is not provided in differential TCM system configurations.

Several basic system modules used in the system implementations, such as TCM encoder, interleaver, deinterleaver, and Viterbi soft decoder with availability of CSI, are programmed in C language and built into SPW library for our specific usage. Some other system modules, such as the AWGN and fading channels, are built using the existing SPW function blocks.

5.3.1 Average White Gaussian Noise Module

The average white Gaussian noise (AWGN) module generates complex Gaussian white noise samples with zero mean and variance adjusted to provide the desired signal-to-noise ratio. This module is constructed by making use of the existing SPW function blocks, which is shown in Figure A.1 of Appendix A.

The complex noise samples are produced by following method. As illustrated in the block diagram, the AWGN module first takes the average signal power as reference and calculates the values of the desired noise variance coefficient based on the given module parameter $\bar{E}_b/N_0$ (in dB). Then, to obtain the necessary noise power, these calculated coefficient values are used to multiply the complex noise samples with zero mean and unit variance, which are generated by a complex white Gaussian noise generator.

The calculation of the variance value is based on the following expressions [44]. We assume that x_k represents a complex signal sample and n_k is a noise sample generated by this module. Therefore, the average signal-to-noise ratio SNR is given by

$$\mathrm{SNR} = \frac{E\{|x_k|^2\}}{E\{|n_k|^2\}} = \frac{E\{|x_k|^2\}}{2\sigma^2} \tag{5.1}$$

where $E\{\}$ denotes expectation, $E\{|x_k|^2\}$ represents the average signal power and $E\{|n_k|^2\}$ the average noise power. $\sigma^2 = N_0/2$ is the variance of the complex noise samples along each of the noise dimensions.

Since the average signal-to-noise ratio is equivalent to the average symbol energy to spectral noise power density ratio $\bar{E}_s/N_0$, the equation (5.1) can also be rewritten as

$$\bar{E}_s/N_0 = \frac{E\{|x_k|^2\}}{2\sigma^2}. \tag{5.2}$$

The values of variance coefficient can be derived from equation (5.2).

$$\sigma^2 = \frac{E\{|x_k|^2\}}{2\bar{E}_s/N_0}. \tag{5.3}$$

Two different values of σ^2 are used in the computer simulation, that is:

$$\sigma^2 = \begin{cases} \frac{E\{|x_k|^2\}}{4\bar{E}_b/N_0}, & \bar{E}_s = 2\bar{E}_b; \\ \\ \frac{E\{|x_k|^2\}}{3\bar{E}_b/N_0}, & \bar{E}_s = \frac{3}{2}\bar{E}_b \end{cases} \tag{5.4}$$

where $\bar{E}_s = 2\bar{E}_b$ corresponds to the case of using rate 2/3 conventional TCM and rate 4/6 multiple TCM, while the $\bar{E}_s = \frac{3}{2}\bar{E}_b$ corresponds to rate 3/6 multiple TCM system.

5.3.2 Fading Channel Modules

Based on the computer models described in Chapter 2, the Rayleigh, Rician and log-normally shadowed Rician channel modules are implemented by using the existing SPW function blocks. The block diagrams of these three modules are given in Figures A.2 - A.4 of Appendix A. In these fading channel modules, the third-order Butterworth lowpass filters are used to shape the fading spectrum of the models [10]. The bandwidth of these filters is adjusted according to the normalized fading bandwidth BT used in the simulation, which is defined in Chapter 2. The other channel parameters are chosen from Table 3.1 for the EHF channel according to the different channel conditions.

5.3.3 TCM Encoders/Modulators

The TCM encoder block encodes the input random data bits and produces coded complex output symbols. The complex symbols can be thought of as the complex envelope representation of a modulated signal. There are two classes of TCM 8-PSK encoders used in our simulation systems. One is the conventional TCM encoder. The other is the multiple TCM encoder. Details of both encoders are discussed in Chapter 3. In each of the two classes, there are also many different encoder structures according to the code rate and number of states. In our simulation, the 4-state, 8-state, 16-state and 64-state rate 2/3 conventional 8-PSK TCM encoders, the 4-state rate 4/6 multiple 8-PSK TCM as well as the 8-state rate 3/6 multiple 8-PSK TCM encoders are simulated. The signal constellation and state transition diagrams of these encoders are shown in Figures 3.2 - 3.4, Figures 3.6 - 3.7 and Table 3.1. Since the TCM encoder is an encoder with memory, the encoder output symbols are determined by both the current input bits and the preceding input bits. At any moment in time, the encoder is in one of a number of states. The current state of the encoder is therefore a function of the previous history together with current input stimuli. With the change from one state to another, the encoder outputs the appropriate branch symbol or symbols according to the state transition diagram. From its characteristics, a TCM encoder is described as a finite state machine in our programming. First, an input file is edited based on the state transition diagram of a specific encoder. This file is then read in by the encoder program and transformed in two tables, a state table and an action table. After initialization of these tables, a driven program is executed and the complex symbols are output with respect to the input bit combinations.

Based on the above design method, three general-purpose encoder blocks are constructed. One is for the conventional rate 2/3 8-PSK TCM. The other two are for rate 4/6 and rate 3/6 multiple 8-PSK TCMs respectively. With each of the three blocks, an encoder with any number of states and 8-PSK symbol partition, but with same code rate, can be simulated by changing only the encoder input file.

5.3.4 Viterbi Soft Decoder

The Viterbi soft decoder block performs the TCM decoding function. This block decodes the incoming complex symbols and produces the decoded bits at the output. For the three TCM encoder blocks mentioned above, three general-purpose Viterbi soft decoder blocks are programmed. For each of the three blocks, a specific decoding procedure is performed by selecting the corresponding decoding input file, which is the same as the input file of the associated encoder. The VA decoding procedure is as described in Chapter 3. The computation of branch metrics for conventional TCM and multiple TCM are different. Since the knowledge of channel state information (CSI) is taken into account in the decoding process for the coherent demodulation case, the decoding metrics are weighted by the fading information.

For conventional TCM decoder, the branch metrics M_b at stage s are computed as

$$M_b = \begin{cases} |y_s - r_s x_s|^2, & \text{with CSI;} \\ \\ |y_s - x_s|^2, & \text{no CSI} \end{cases} \tag{5.5}$$

where y_s represents the received and corrupted symbol at stage s, x_s is the branch symbol of the associated encoder, and r_s denotes the estimate of channel fading amplitude at stage s.

For multiple TCM decoder with multiplicity q equal to 2, the branch metric at stage s is calculated by

$$M_b = \begin{cases} |y_s^{(1)} - r_s^{(1)} x_s^{(1)}|^2 + |y_s^{(2)} - r_s^{(2)} x_s^{(2)}|^2, & \text{with CSI;} \\ |y_s^{(1)} - x_s^{(1)}|^2 + |y_s^{(2)} - x_s^{(2)}|^2, & \text{no CSI} \end{cases} \tag{5.6}$$

where $y_s^{(1)}$ and $y_s^{(2)}$ represent the two received symbols within the time unit from one stage to another stage, $x_s^{(1)}$ and $x_s^{(2)}$ represent the corresponding two symbols on the branch, and $r_s^{(1)}$ and $r_s^{(2)}$ denote the channel amplitudes corresponding to the two received symbols in the same time unit.

For differential TCM system, the minimum distance metric used for VA decoding is not an optimum metric as discussed in Chapter 4 and is used as a suboptimum solution, which is given by

$$M_b = \begin{cases} |y_s - x_s|^2, & \text{conventional TCM;} \\ |y_s^{(1)} - x_s^{(1)}|^2 + |y_s^{(2)} - x_s^{(2)}|^2, & \text{multiple TCM.} \end{cases} \tag{5.7}$$

5.3.5 Block Interleaver and Deinterleaver

The block interleaver and deinterleaver are developed according to the interleaving rules described in Chapter 3. The Figure 5.1 illustrates the interleaving procedure for an interleaver with interleaving depth $D = 3$ and span $S = 7$ symbols.

As demonstrated in Figure 5.1, the interleaver reads in the incoming symbols and stores them sequentially into the buffer positions $1, 2, 3, 4, 5, 6, 7, 8, 9, \ldots$. When the buffer is full, the interleaver reads out these symbols from buffer positions in the order of $1, 8, 15, 2, 9, 16$, and so on. The deinterleaver reads in the received symbols and put them into the buffer positions $1, 8, 15, 2, 9, 16, \ldots$. Once the buffer is full, the deinterleaver reads out symbols sequentially from positions $1, 2, 3, 4, 5, 6, 7, 8, 9, \ldots$. Since a symbol is represented by a complex value, each of the buffer positions actually

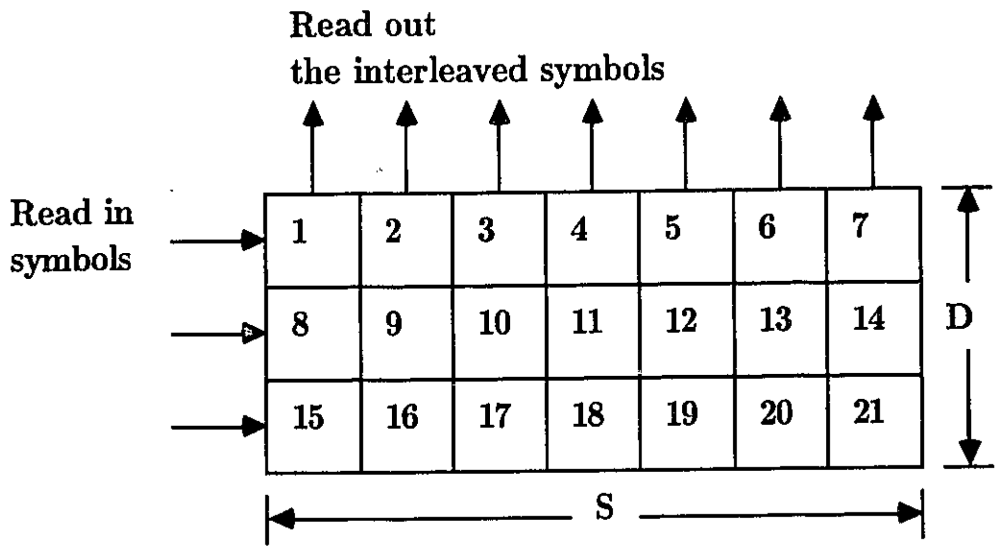

Figure 5.1: Example of a block interleaver of size 3×7 symbols

consists of real and imaginary components.

5.4 Summary

In this chapter, the simulation platform SPW is briefly introduced. The EHF mobile satellite communication link components are described and their implementations in the SPW simulation software package are presented in detail. The simulation systems are set up by the existing SPW function blocks and the self-programmed component modules. The key link component modules like the TCM encoder, block interleaver/ deinterleaver and Viterbi soft decoder are programmed in C language.

Chapter 6

Simulation Results and Discussion

6.1 Introduction

In this chapter, the performance results obtained by computer simulation are presented. In order to make comparison between conventional TCM and multiple TCM schemes, all the selected TCM schemes in the simulation are designed based on an 8-PSK signal constellation. The signal transmission rate of the simulation system is 4800 symbols per second. For Viterbi decoder, the truncation length is set with 32 symbols. The block interleaver takes the size of 16×8 symbols.

During the simulation, to obtain the bit error probability P_b under given signal-to-noise ratios, the total number of the transmitted data bits (N) is chosen according to the magnitude of the resulting BER P_b. By using a normal approximation [44], the confidence intervals for each of the calculated bit error probability P_b can be computed. For those values of P_b above 10^{-4}, the total number of the transmitted bits N is chosen to be at least 100 divided by the oder of magnitude of P_b, which produces a 95% confidence interval of about $[0.8P_b,\ 1.25P_b]$. For instance, if the order of magnitude of P_b is 10^{-3}, then the number of transmitted bits N is at least 10^5. For those bit error rates of the order of 10^{-5}, N is chosen as $10/10^{-5}$,i.e., 10^6, which gives a 95% confidence interval of about $[0.55P_b,\ 1.8P_b]$.

6.2 Performance of Coherent TCM Systems

The general model for a coherent TCM simulation system is illustrated in Figure 4.1. Based on this model, six TCM schemes, as described in Chapter 3, are evaluated over the AWGN, Rayleigh, Rician and log-normally shadowed Rician channels. All the performance results are obtained from the simulation system implemented under the assumption that perfect coherent detection is achieved, i.e., only amplitude fading distortion is considered. In the simulations, the normalized fading bandwidth BT is chosen as 0.25 or 0.5.

6.2.1 Coherent TCM Schemes on AWGN Channel

In Figure 6.1, the BER performances of the six coherent TCM schemes on the AWGN channel are presented. The curves obtained for the 4-state, 8-state and 16-state rate 2/3 conventional TCM schemes conform well to the published simulation results in [21, 26, 31]. This verifies that our TCM simulation systems are properly calibrated. From this figure, it is observed that: (1) the performance of the conventional TCM schemes improve as the number of the encoder states increases; (2) with the same code rate and the same number of states, 4-state conventional TCM has the same performance as 4-state multiple TCM at low $\bar{E}_b/N_0$, but performs better than 4-state MTCM as the $\bar{E}_b/N_0$ is beyond 6 dB (the reason for this is that the 4-state MTCM code is optimized for fading channels instead of AWGN); (3) the 16-state and 8-state conventional TCM schemes demonstrate robust performances since they are optimized for both fading and AWGN channels [25]; (4) it is also observed that the rate 3/6 8-state MTCM scheme shows a strong performance at low $\bar{E}_b/N_0$.

6.2.2 Coherent TCM on EHF Fading Channels

A. General Performance of Coherent TCM Schemes

The results in Figures 6.2 - 6.4 are obtained from the evaluation of the coherent

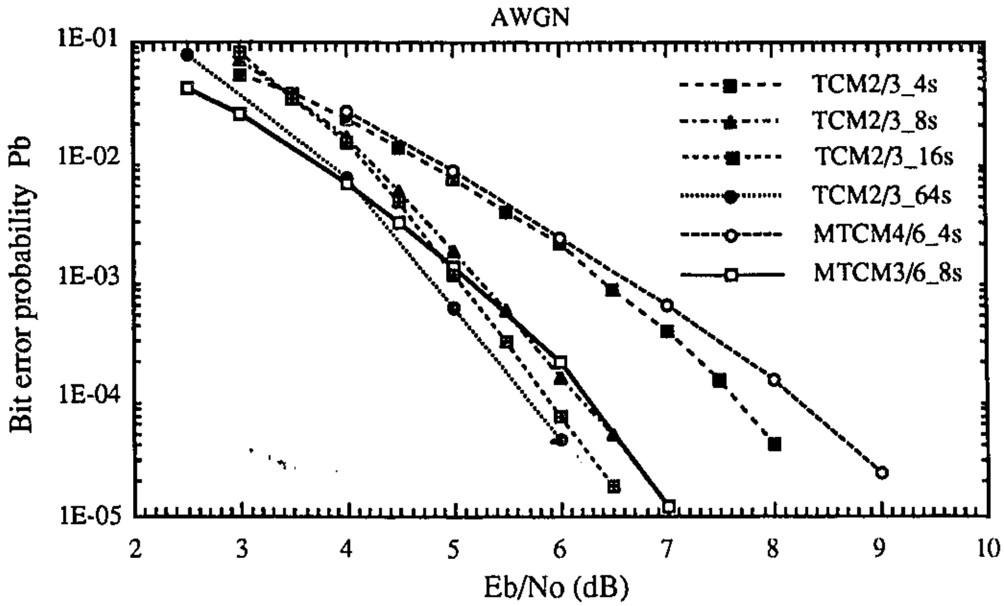

Figure 6.1: BER performances of coherent TCM schemes on AWGN channel.

TCM system, with interleaving and channel state information, on the log-normally shadowed Rician model in the presence of white Gaussian noise. The performances of the coherent TCM schemes over the light, average and heavy shadowed Rician channels demonstrate a similar performance behavior.

In Figures 6.2 - 6.4, it is shown that the performances of the TCM schemes on the fading channel are determined by their effective lengths and distance products, as listed in Table 3.2 of Chapter 3. The 64-state conventional TCM demonstrates the best performance in the fading channel since it has the largest effective length ($L = 4$) and minimum distance product ($P_{min} = 8$) among the six considered TCM schemes. However, this code has the largest complexity as shown in Table 3.3 of Chapter 3.

Contrary to the case on AWGN channel, the performance of the 4-state MTCM scheme is better than its counterpart, the conventional 4-state TCM scheme, on the fading channels. This indicates that the 4-state MTCM scheme is more suitable for fading channels than the 4-state conventional scheme. This can be explained by the impact of effective length L and product P_{min} on the performances of the

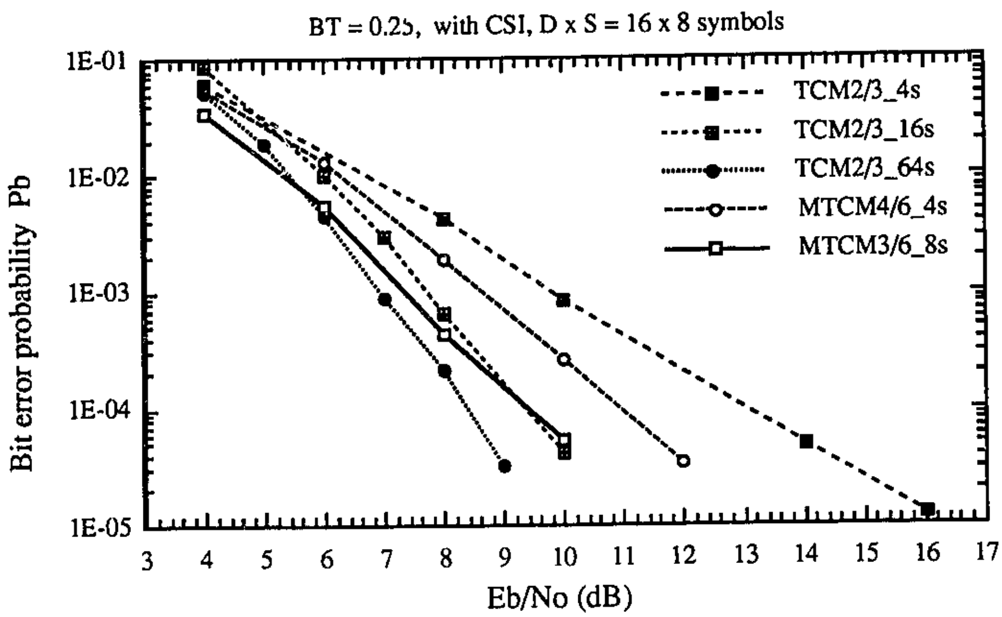

Figure 6.2: BER performances of coherent TCM schemes on light shadowed EHF channel with interleaving and CSI.

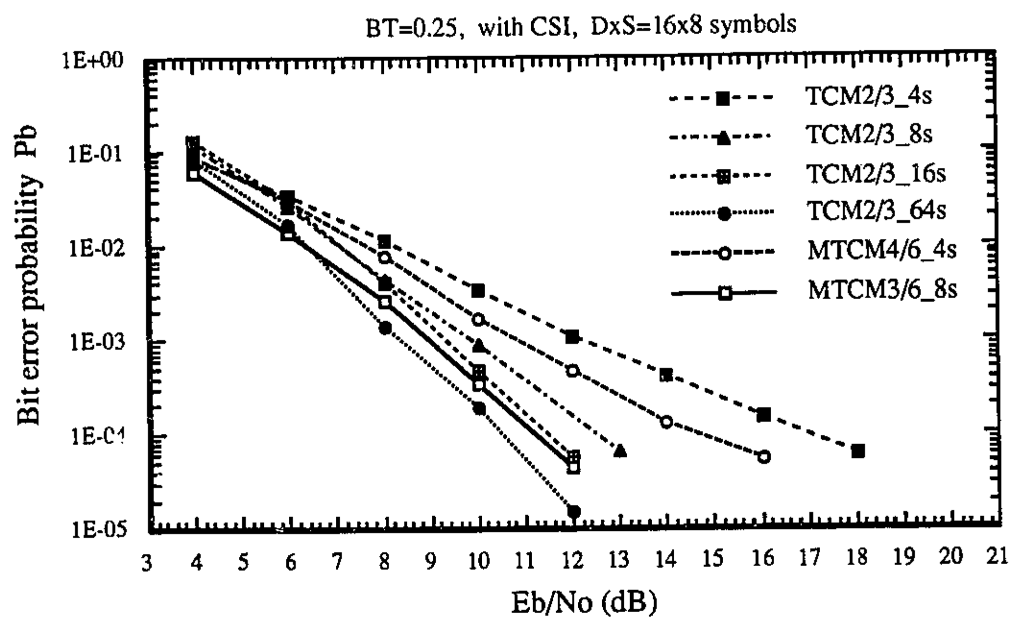

Figure 6.3: BER performances of coherent TCM schemes on average shadowed EHF channel with interleaving and CSI.

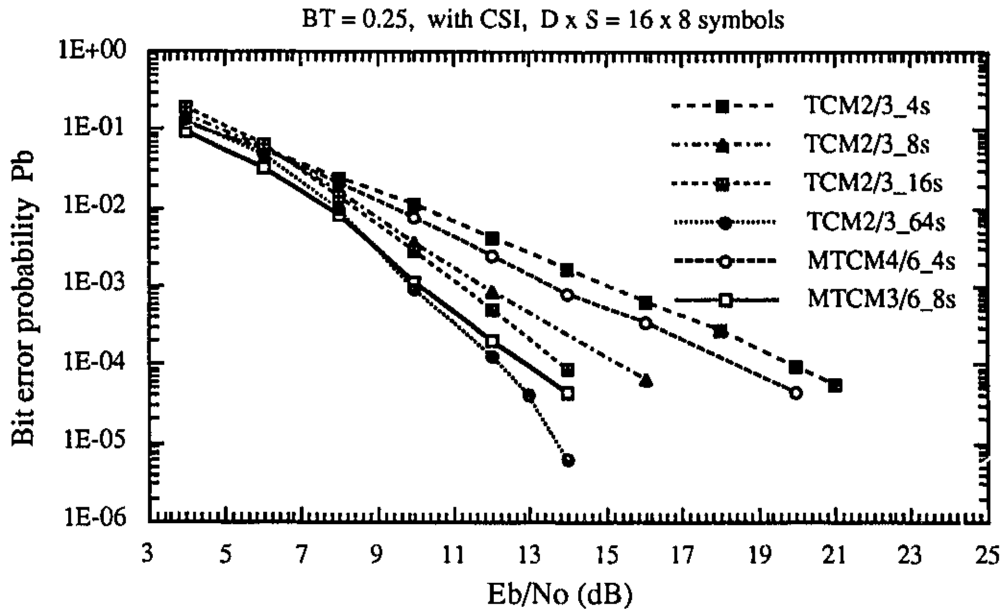

Figure 6.4: BER performances of coherent TCM schemes on heavy shadowed EHF channel with interleaving and CSI.

TCM schemes. The 4-state MTCM has $L = 2$ and $P_{min} = 4$, while the 4-state TCM has $L = 2$ and $P_{min} = 1.172$. Both schemes have the effective length of 2. Since the P_{min} of the 4-state MTCM is larger than that of the 4-state conventional TCM, the performance of the 4-state MTCM should be better according to the code design criteria for fading channels. In addition, as shown in Figures 6.2 - 6.4, at $P_b = 10^{-4}$, the performances of the 4-state MTCM are 2 dB, 1.8 dB and 1 dB better than that of the conventional 4-state TCM corresponding to the light, average and heavy shadowing conditions. This demonstrates that the performance improvement decreases as the shadowing effect increases.

Compared to the 16-state conventional TCM, the rate 3/6 8-state MTCM scheme demonstrates a better performance at low $\bar{E}_b/N_0$, but almost the same performance at high $\bar{E}_b/N_0$, on the fading channels. This is because both schemes have the same effective length ($L = 3$), but the 8-state MTCM has a larger minimum branch product value ($P_{min} = 8$) than that of the 16-state TCM ($P = 4.68$) scheme. As described in

Chapter 3, the performance of a TCM code is mainly determined by the product P at low $\bar{E}_b/N_0$, and by the effective length L at high $\bar{E}_b/N_0$. From Figures 6.2 - 6.4, it has been seen that the theoretical analysis is verified by the simulation results with respect to the 8-state MTCM and the 16-state conventional TCM schemes. It is also noted that the effects of the type of shadowing on the performances of the 8-state MTCM and the 16-state TCM are quite different.

Table 6.1: Performance degradation as compared with AWGN due to the fading effect.

channel	P_b	TC4s	TC8s	TC16s	TC64s	MTC4s	MTC8s
light	10^{-3}	3.5 dB	N/A	2.8 dB	2.3 dB	2.0 dB	2.4 dB
shadowing	10^{-4}	5.3 dB	N/A	3.5 dB	2.7 dB	2.7 dB	3.1 dB
average	10^{-3}	5.8 dB	4.5 dB	4.4 dB	3.7 dB	5.3 dB	3.9 dB
shadowing	10^{-4}	9.3 dB	6 4 dB	5.7 dB	4.9 dB	6.8 dB	5.0 dB
heavy	10^{-3}	8.8 dB	6.4 dB	6.3 dB	5.3 dB	6.9 dB	5.1 dB
shadowing	10^{-4}	12.3 dB	9.4 dB	5.9 dB	6.7 dB	10.3 dB	6.8dB

The performance degradations caused by the fading effects under certain shadowing conditions compared to AWGN condition are summarized in Table 6.1. From these results, it can be seen that the performance degradation is quite severe due to the fading distortion. For example, the 4-state conventional TCM scheme needs an additional 9.3 dB to combat fading in order to keep the bit error probability at $P_b = 10^{-4}$ for the average shadowed channel. For all the TCM schemes, the performance degradation increases as the shadowing effect becomes more severe. At a bit error rate of 10^{-4}, the performance degradation of the 4-state TCM is 5.3 dB on light shadowed channel and 12.3 dB on heavy shadowed channel in comparison with the AWGN environment.

Table 6.2 lists the actual values of $\bar{E}_b/N_0$, at which bit error rates of 10^{-3} and 10^{-4} are achieved, for different TCM schemes with interleaving and CSI under the conditions of light, average and heavy shadowing. It indicates that: (1) as channel changes from the light to average shadowing, the schemes generally have around 1 to 2 dB degradation except for the two 4-state schemes, which have up to 4 dB losses.

This means that the performances of both 4-state schemes are strongly affected by shadowing; (2) the degradation for all schemes is about 2 to 3 dB when channel changes from the average to heavy shadowing, which demonstrates severe distortion caused by the heavy shadowing condition.

Table 6.2: Corresponding $\bar{E}_b/N_0$ for a given BER performance.

channel	P_b	TC4s	TC8s	TC16s	TC64s	MTC4s	MTC8s
light	10^{-3}	9.9 dB	N/A	7.8 dB	7.0 dB	8.7 dB	7.5 dB
shadowing	10^{-4}	13.0 dB	N/A	9.4 dB	8.4 dB	10.9 dB	9.4 dB
average	10^{-3}	12.2 dB	9.8 dB	9.4 dB	8.4 dB	11.0 dB	9.0 dB
shadowing	10^{-4}	17.0 dB	12.6 dB	11.6 dB	10.6 dB	15.0 dB	11.3 dB
heavy	10^{-3}	15.2 dB	11.7 dB	11.3 dB	10.0 dB	13.6 dB	10.2 dB
shadowing	10^{-4}	20.0 dB	15.6 dB	13.8 dB	12.4 dB	18.5 dB	13.1 dB

As can be expected, the stronger the LOS component is, the better the TCM codes perform. This can also be shown for the cases on the Rayleigh and Rician fading conditions with $BT = 0.5$, as illustrated on Figure 6.5 - 6.7. Taking the Rayleigh channel as a reference (i.e., no LOS), the performances of the TCM schemes on the Rician channel improve as the K factor increases. This is clearly shown on Figure 6.8, which presents the performances of the 4-state MTCM scheme over different channel conditions. It is noted that the code has almost the same performance on both Rayleigh and heavy shadowed Rician channels. This phenomenon conforms to the statistic results of the simulated channel models, which demonstrated similar statistics for both channels as presented in Figures 2.5 - 2.7.

B. Effects of Interleaving and CSI

To evaluate the effects of channel state information and interleaving technique, simulations are conducted with following configurations:

- TCM scheme without interleaving and without CSI,
- TCM scheme with interleaving and without CSI,

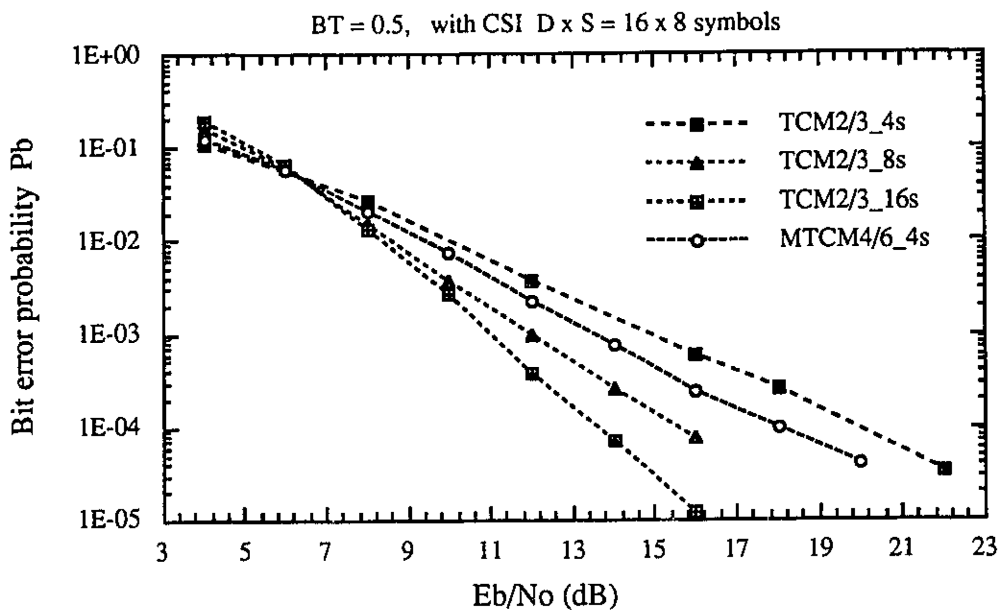

Figure 6.5: BER performances of coherent TCM schemes on Rayleigh channel with interleaving and CSI.

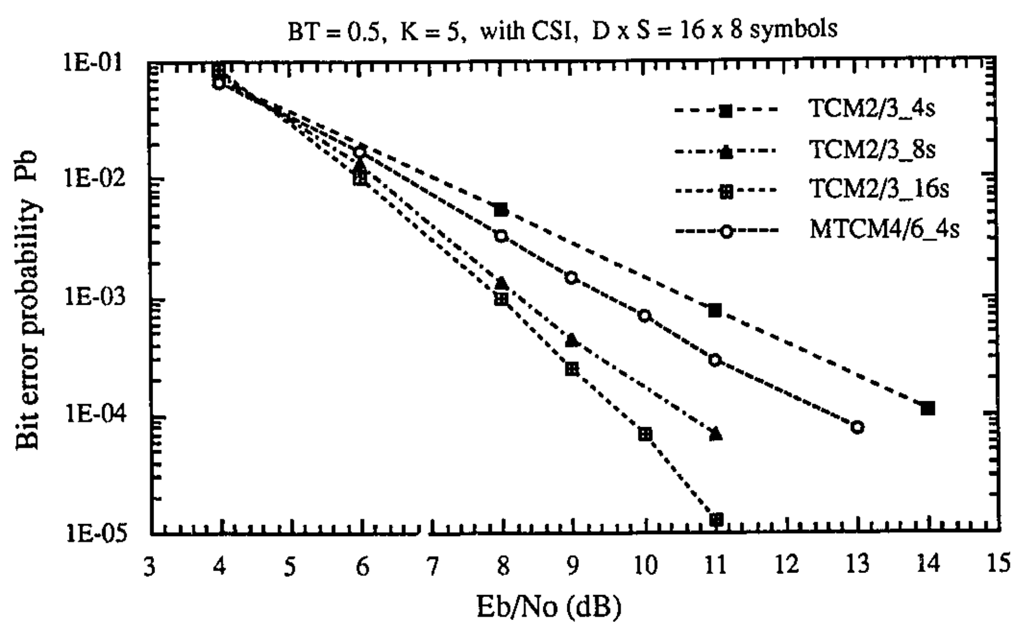

Figure 6.6: BER performances of coherent TCM schemes on Rician channel (K = 5) with interleaving and CSI.

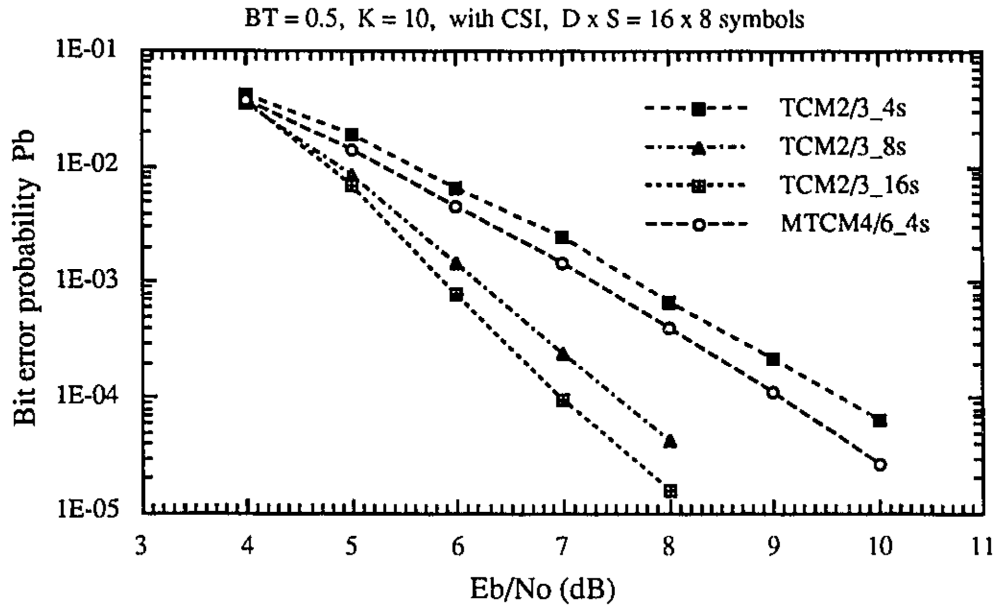

Figure 6.7: BER performances of coherent TCM schemes on Rician channel (K = 10) with interleaving and CSI.

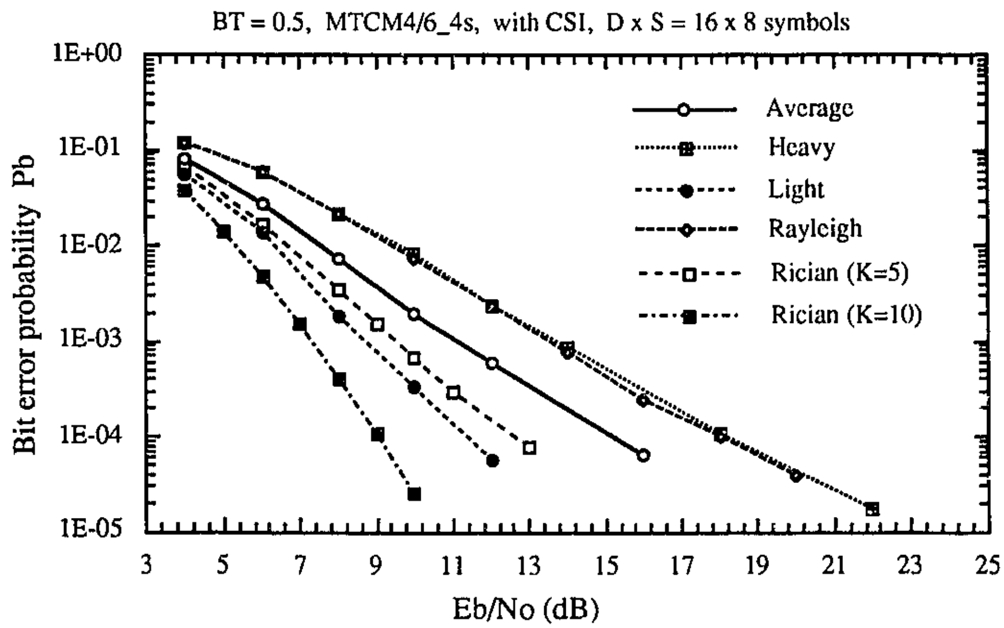

Figure 6.8: Performance comparison of coherent rate 4/6 4-state MTCM on Rayleigh, Rician, and shadowed Rician EHF channels.

- TCM scheme with interleaving and CSI.

The simulation results for showing the impact of interleaving and CSI are obtained by applying different TCM schemes on various channel conditions.

Figures 6.9 - 6.11 gives the results of the 4-state conventional TCM on the light, average and heavy shadowed EHF channels respectively. It is shown in Figure 6.9 that, without interleaving and CSI, to achieve a BER of 10^{-4} over the light shadowed EHF channel, $\bar{E}_b/N_0$ of more than 16 dB is required for the 4-state TCM scheme. When interleaving is added, only 14.4 dB $\bar{E}_b/N_0$ is needed. Therefore, 1.6 dB improvement is achieved by interleaving under this condition. If the ideal CSI is used, another 1 dB gain is obtained. When shadowing becomes heavier, as illustrated in Figures 6.10 and 6.11, the effect of the interleaving is reduced. However, the CSI still plays an important role in the performance improvement (i.e., about 0.5 dB improvement).

The effects of interleaving and CSI on the 4-state MTCM scheme are shown in Figures 6.12 - 6.14. It is shown that the interleaving technique is more effective, especially at higher $\bar{E}_b/N_0$, on the performance improvement of the 4-state MTCM than the conventional 4-state TCM. As an example, at the BER of 10^{-4}, the interleaving provides about 3 dB of improvement for light shadowing. The interleaving effect is diminishing as the shadowing increases. CSI provides similar improvement for the 4-state MTCM as in the case of the 4-state conventional TCM.

When applied to the conventional 8-state and 16-state TCM, symbol interleaving and CSI have the similar effects on the BER performances as to the 4-state TCM and MTCM schemes. As shown in Figures 6.15 - 6.19, the interleaving provides almost no improvement at low $\bar{E}_b/N_0$, but at high $\bar{E}_b/N_0$, the improvement is significant. Under the heavy shadowing condition, interleaving provides no improvement to the 16-state TCM except at very high $\bar{E}_b/N_0$, and very little improvement to the 8-state TCM. However, the CSI can give significant improvement to both of these two schemes.

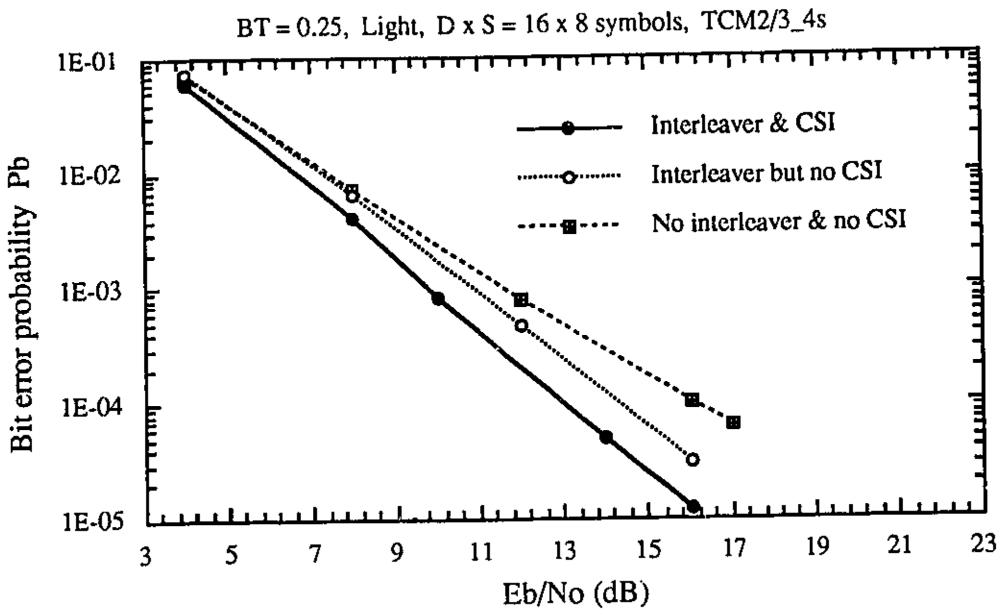

Figure 6.9: Comparison of coherent rate 2/3 4-state TCM on light shadowed EHF channel with different system configurations.

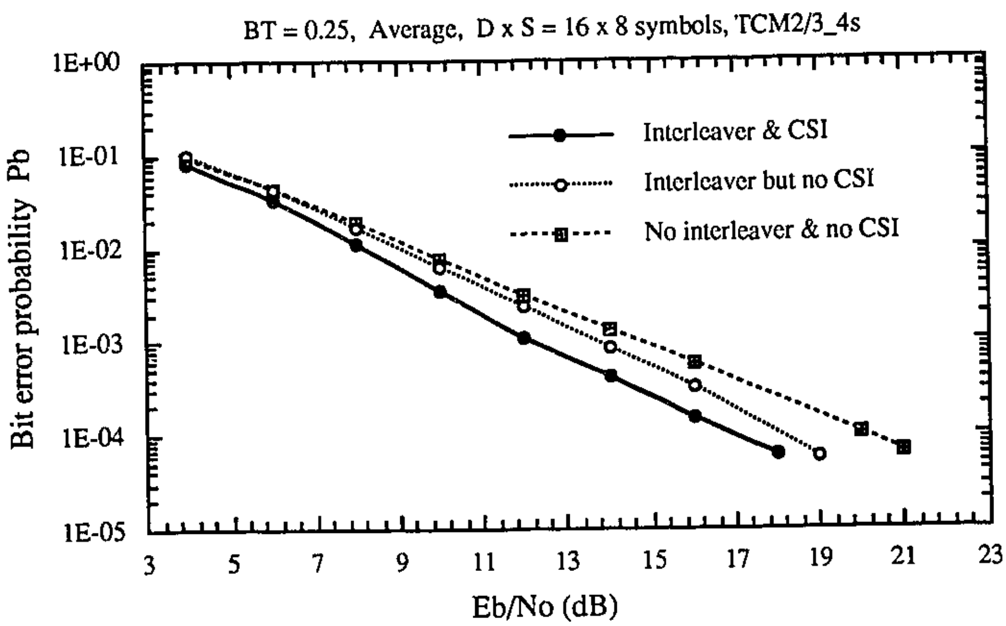

Figure 6.10: Comparison of coherent rate 2/3 4-state TCM on average shadowed EHF channel with different system configurations.

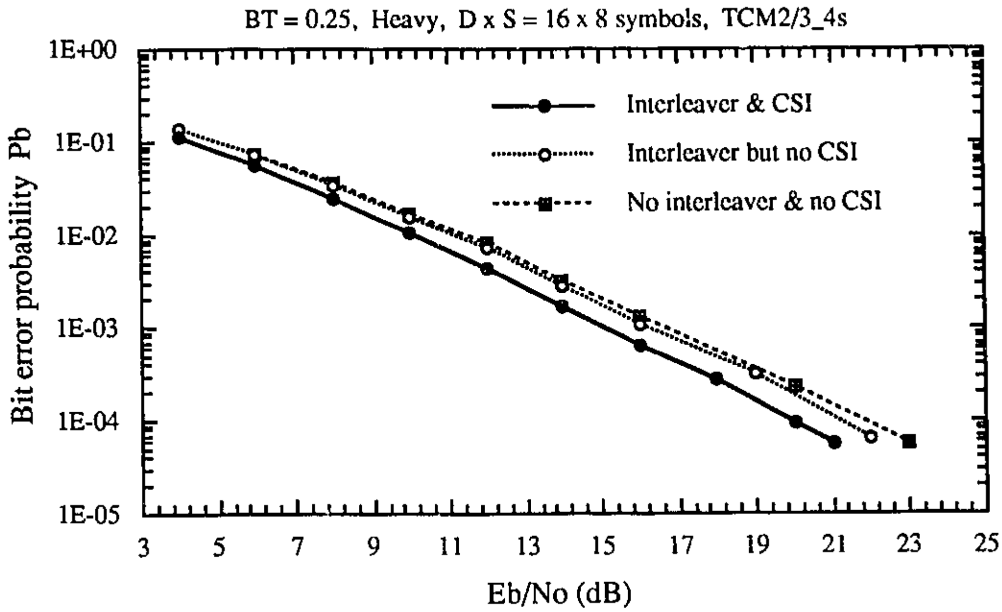

Figure 6.11: Comparison of coherent rate 2/3 4-state TCM on heavy shadowed EHF channel with different system configurations.

Figures 6.20 - 6.25 present the effects of CSI and interleaving on the performances of the 8-state MTCM and 64-state conventional TCM schemes. Both CSI and interleaving provide significant improvement to the performance even under the heavy shadowed condition. This demonstrates a strong error control capability of these two schemes.

Figures 6.26 - 6.32 present the performances of the TCM schemes on the Rayleigh and Rician channels under the condition of normalized fading bandwidth $BT = 0.5$. These figures demonstrate that interleaving has almost no effect on the performances of the TCM schemes under high BT. This is because that, as BT becomes larger, the fading amplitudes changes faster. For fast fading channel, the effect of the interleaving is limited. On the other hand, the CSI still has a strong effect on the performance improvement of the TCM scheme. Comparing the Figures 6.26, 6.27 and 6.28, it shows that, for 16-state conventional TCM, the performance improvement that results from CSI increases as the LOS signal decreases (i.e., K decreases). For example, at

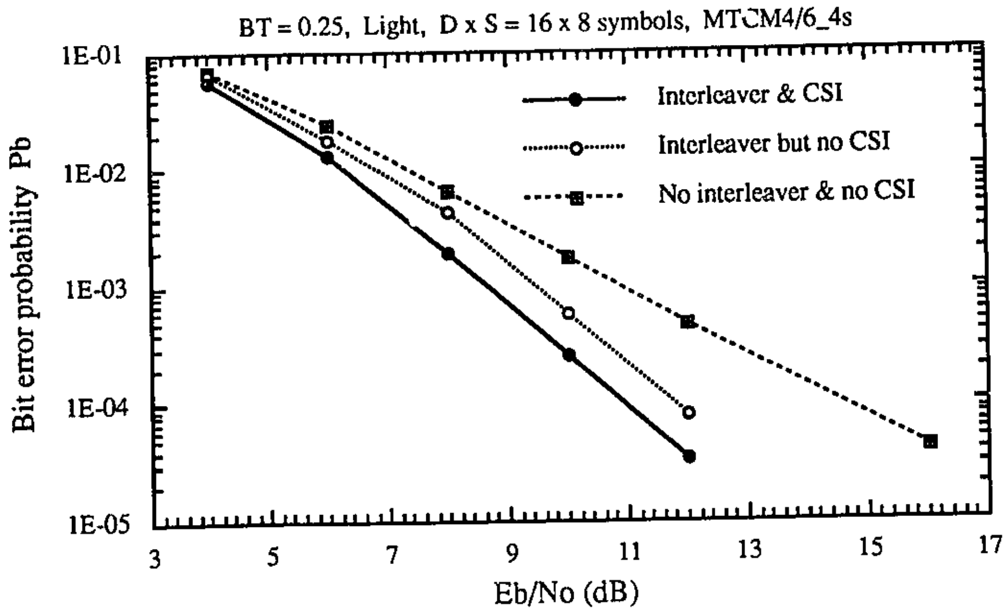

Figure 6.12: Comparison of coherent rate 4/6 4-state MTCM on light shadowed EHF channel with different system configurations.

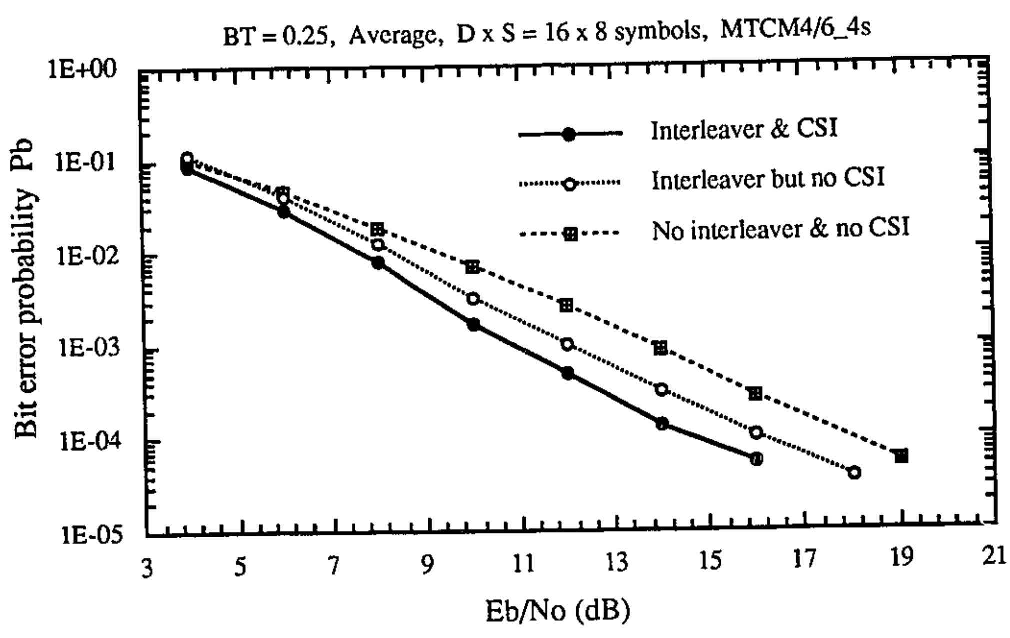

Figure 6.13: Comparison of coherent rate 4/6 4-state MTCM on average shadowed EHF channel with different system configurations.

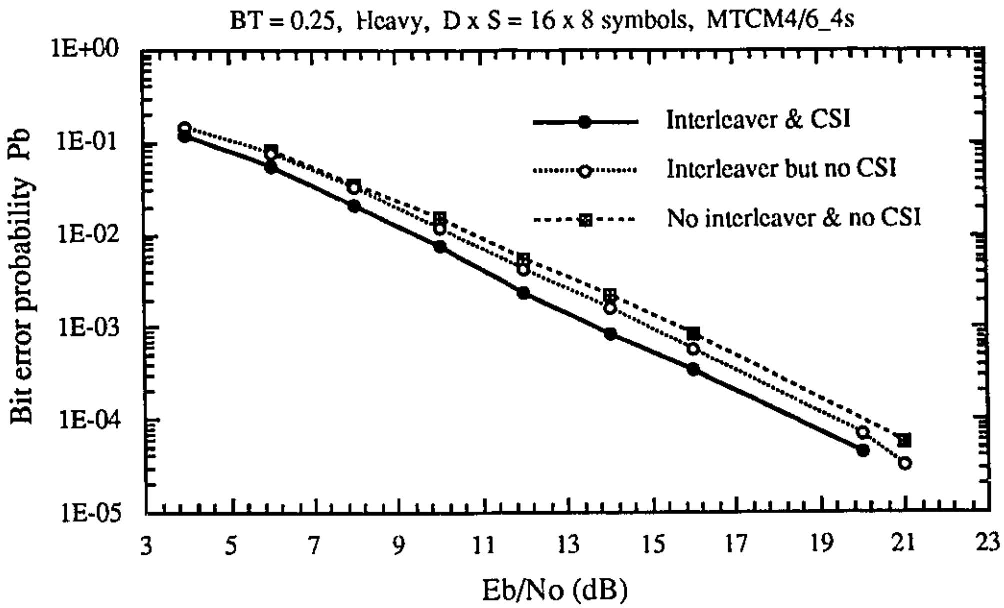

Figure 6.14: Comparison of coherent rate 4/6 4-state MTCM on heavy shadowed EHF channel with different system configurations.

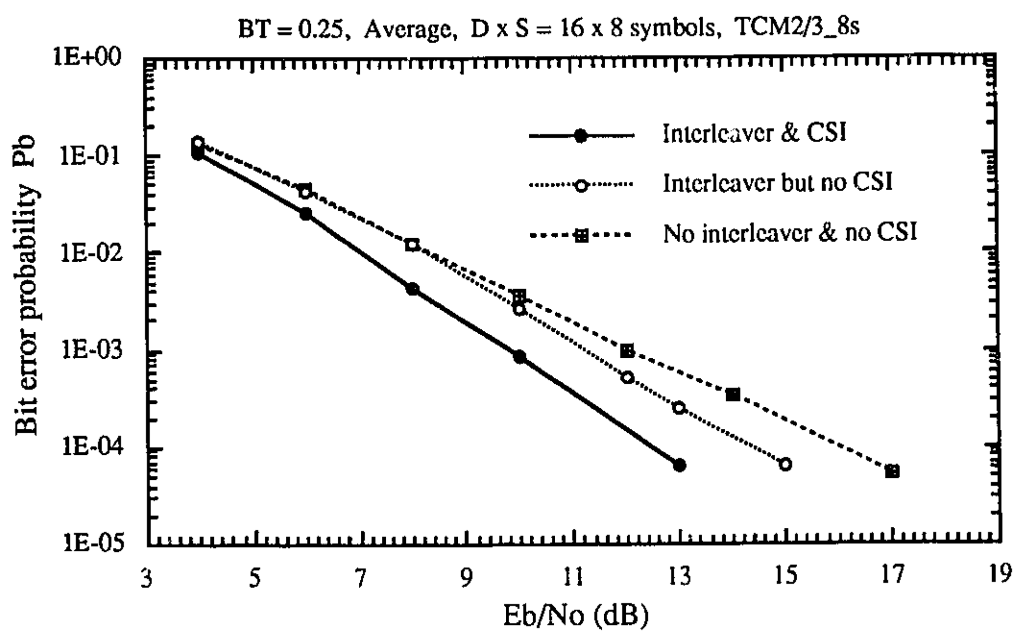

Figure 6.15: Comparison of coherent rate 2/3 8-state TCM on average shadowed EHF channel with different system configurations.

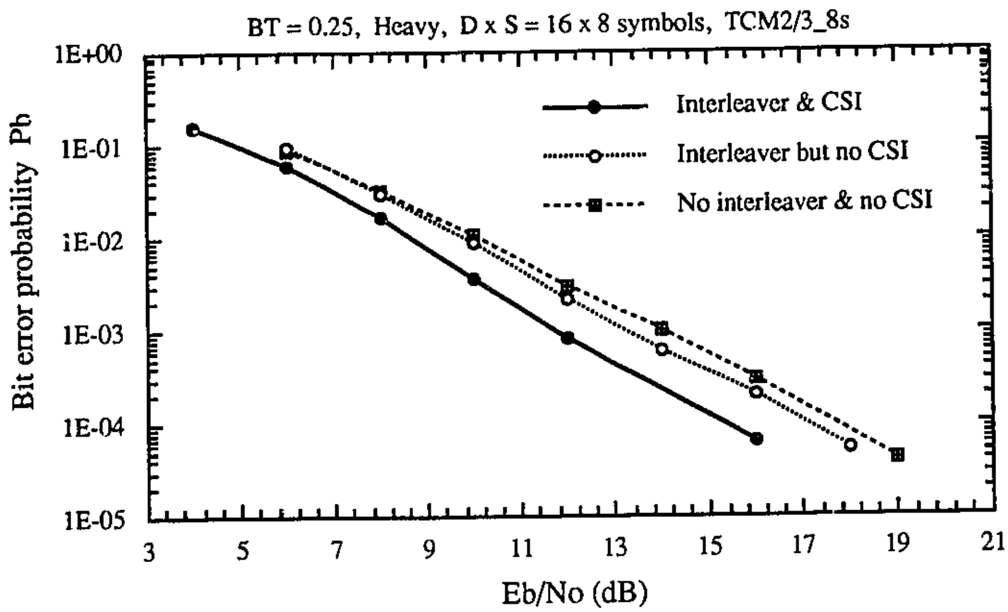

Figure 6.16: Comparison of coherent rate 2/3 8-state TCM on heavy shadowed EHF channel with different system configurations.

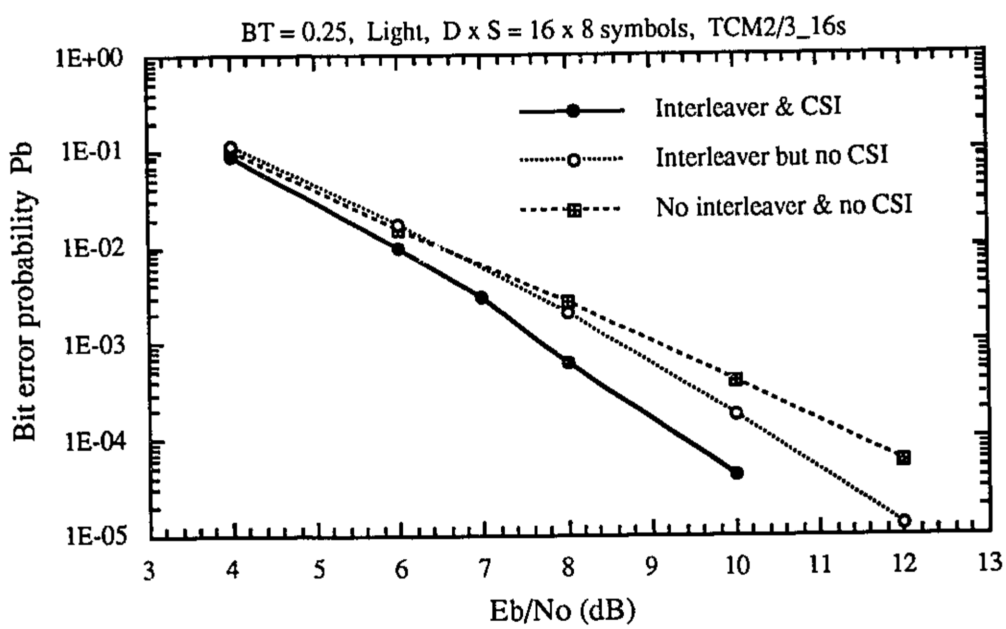

Figure 6.17: Comparison of coherent rate 2/3 16-state TCM on light shadowed EHF channel with different system configurations.

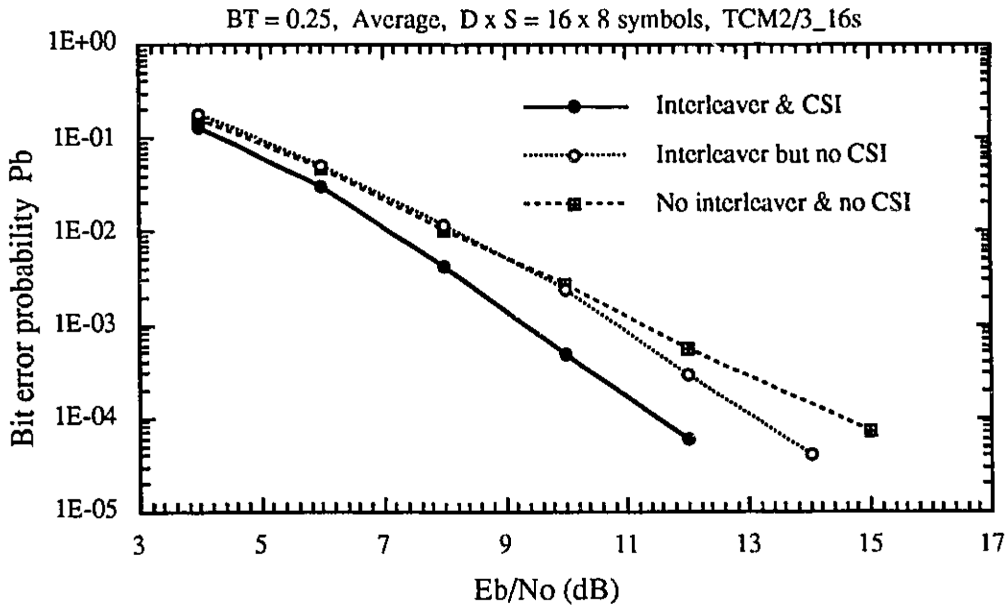

Figure 6.18: Comparison of coherent rate 2/3 16-state TCM on average shadowed EHF channel with different system configurations.

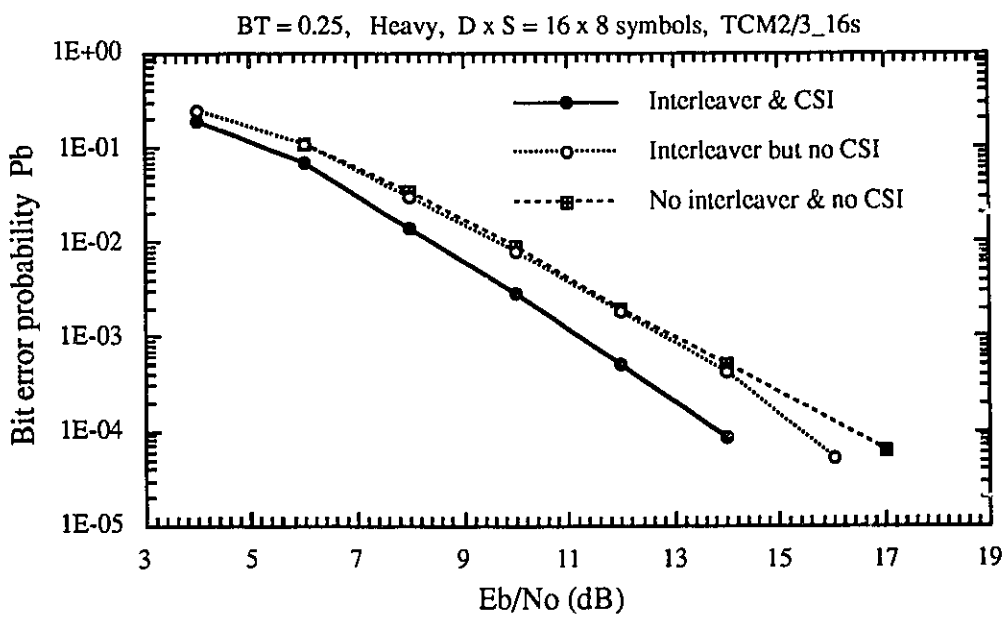

Figure 6.19: Comparison of coherent rate 2/3 16-state TCM on heavy shadowed EHF channel with different system configurations.

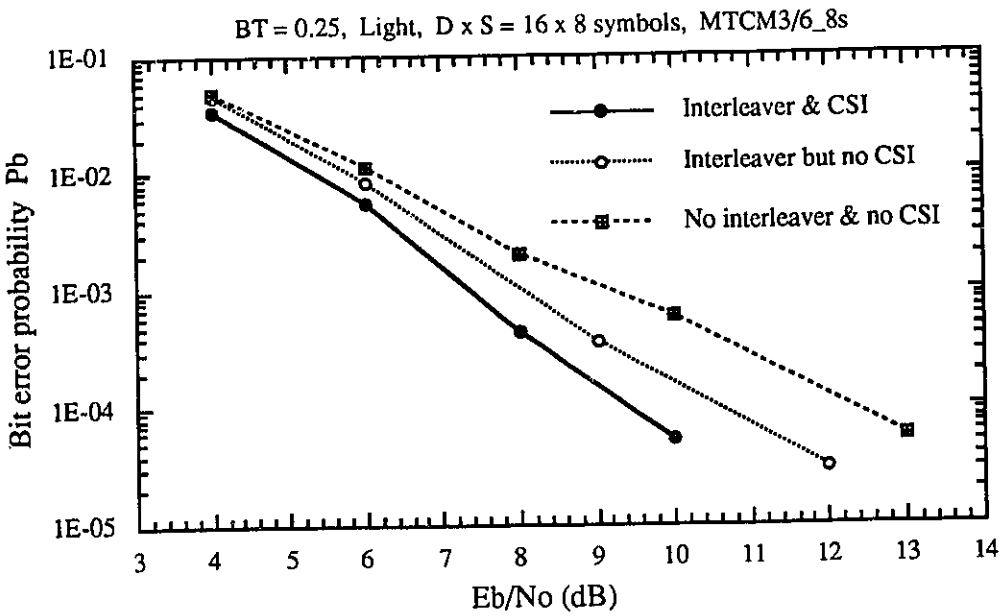

Figure 6.20: Comparison of coherent rate 3/6 8-state MTCM on light shadowed EHF channel with different system configurations.

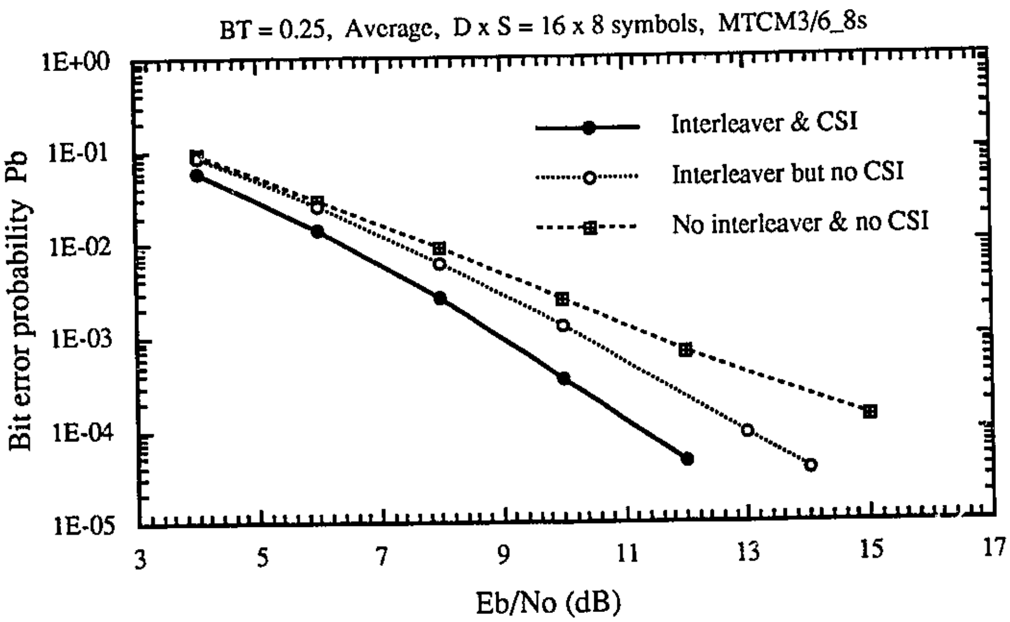

Figure 6.21: Comparison of coherent rate 3/6 8-state MTCM on average shadowed EHF channel with different system configurations.

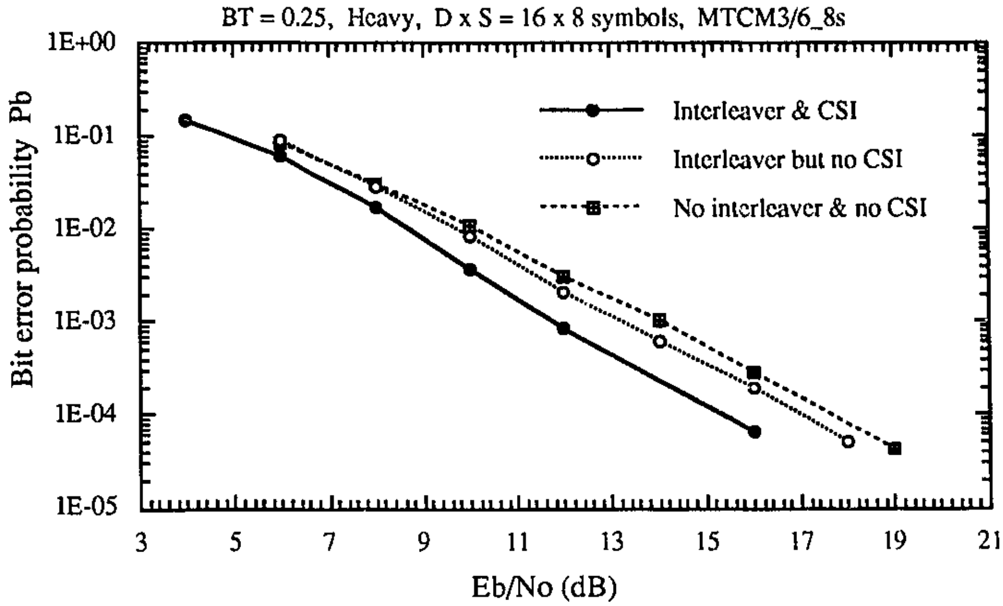

Figure 6.22: Comparison of coherent rate 3/6 8-state MTCM on heavy shadowed EHF channel with different system configurations.

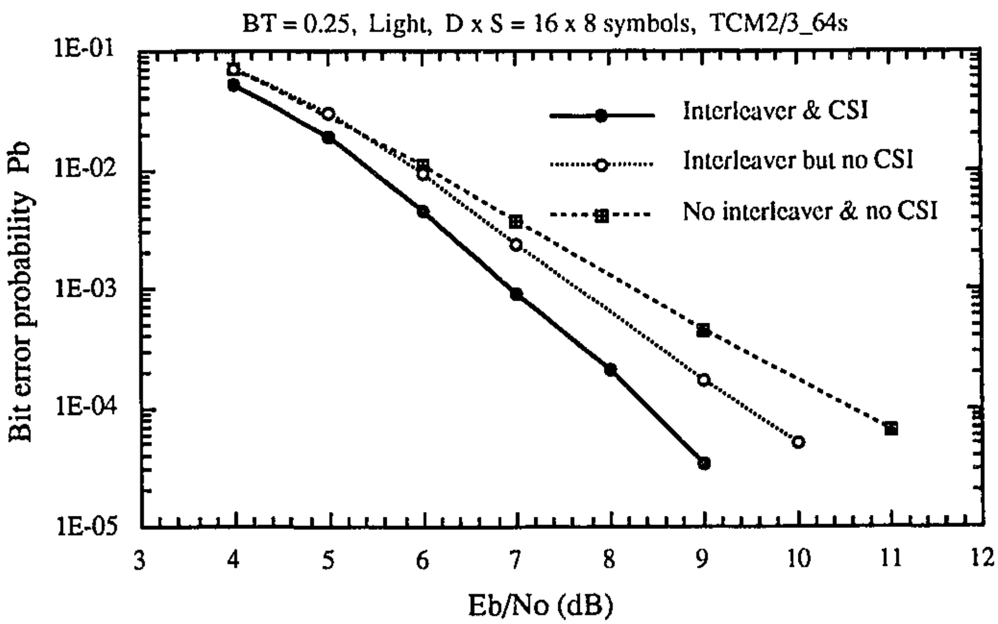

Figure 6.23: Comparison of coherent rate 2/3 64-state TCM on light shadowed EHF channel with different system configurations.

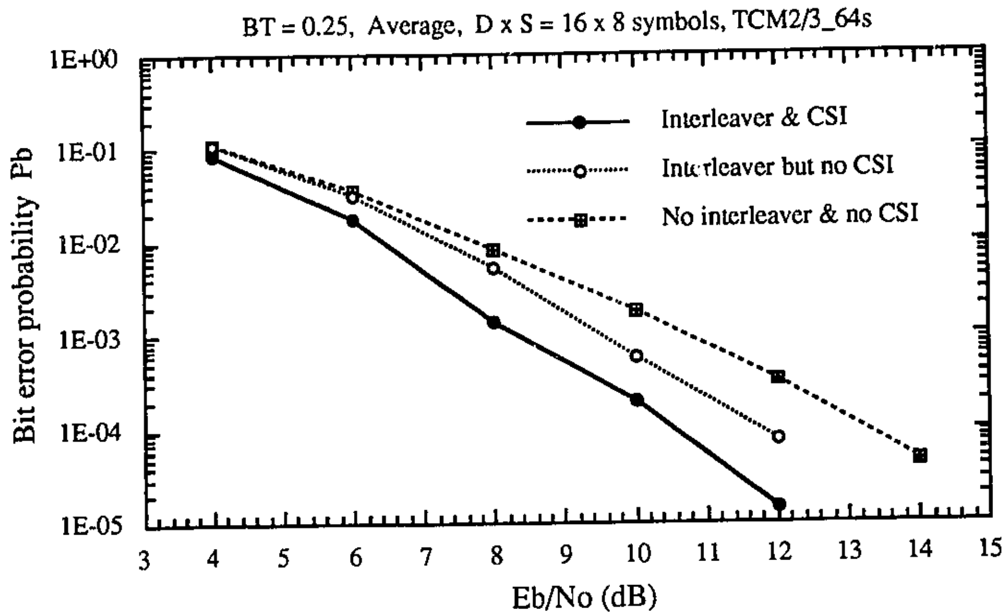

Figure 6.24: Comparison of coherent rate 2/3 64-state TCM on average shadowed EHF channel with different system configurations.

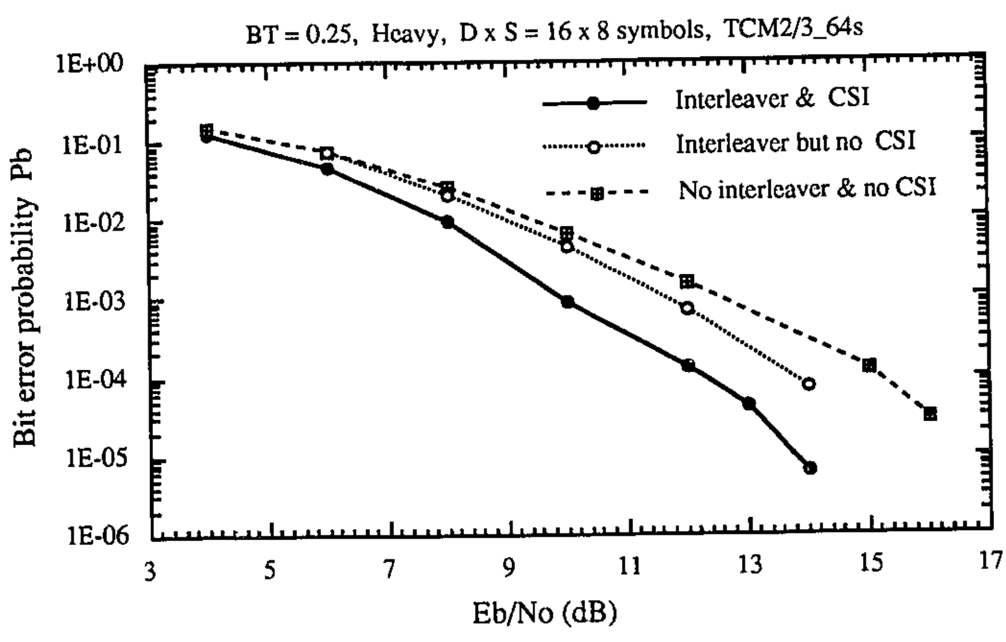

Figure 6.25: Comparison of coherent rate 2/3 64-state TCM on heavy shadowed EHF channel with different system configurations.

a BER of 10^{-4}, the 16-state TCM scheme produces about 0.5 dB, 1.3 dB and 2 dB improvement for K-factors equal to 10 dB, 5 dB and 0 dB (i.e., the Rayleigh channel) respectively. Similar property is observed on Figures 6.29, 6.30 and 6.31 for the 8-state conventional TCM. Figure 6.32 shows that almost no improvement is made by using interleaving for the 4-state multiple TCM scheme on Rayleigh channel with BT equal to 0.25.

In order to evaluate the effect of the interleaving depth and span on the performance of a TCM scheme, the BER performances of the 4-state MTCM scheme on the average shadowed Rician channel with different interleaver sizes ($D \times S$) are presented in Figure 6.33. The results show that the changes of the interleaving depths and spans do not have much effect on the performance of the 4-state MTCM. This is because the fading rate becomes fast under larger BT and larger interleaving depths and spans do not lead to better BER performances on fast fading channels [45].

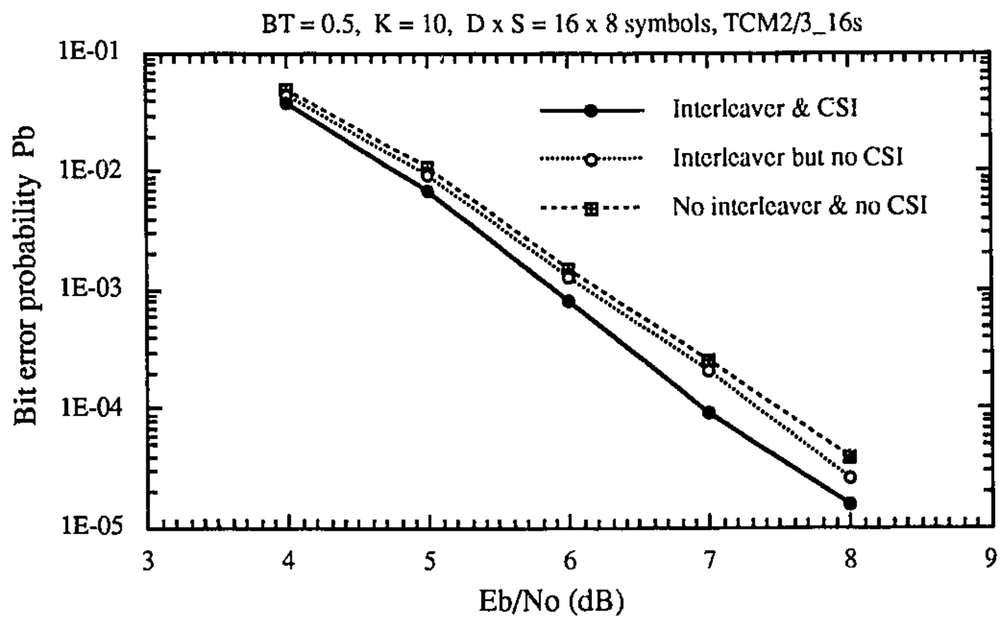

Figure 6.26: Comparison of coherent rate 2/3 16-state TCM on Rician (K = 10) channel with different system configurations ($BT = 0.5$).

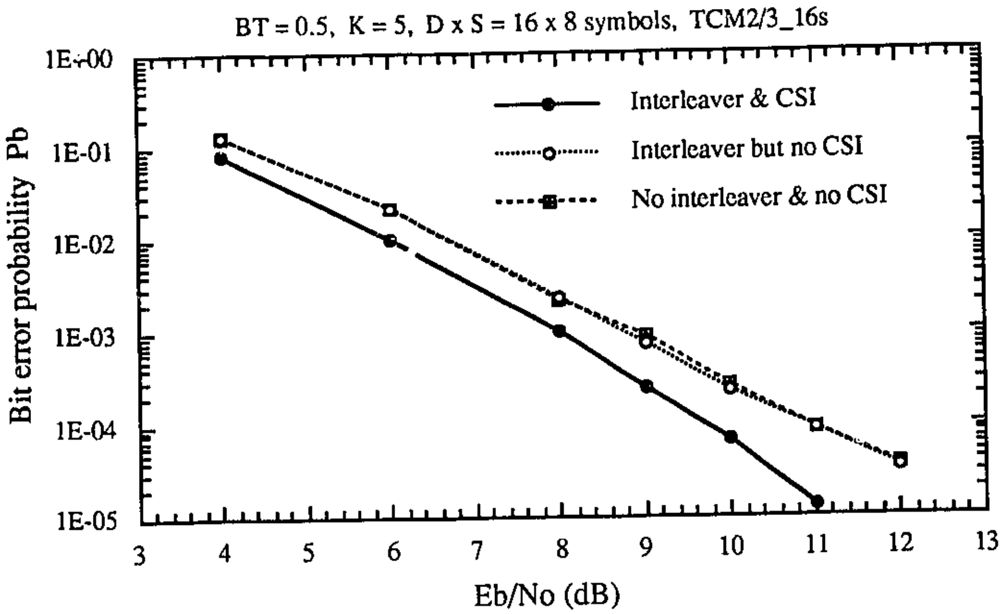

Figure 6.27: Comparison of coherent rate 2/3 16-state TCM on Rician ($K = 5$) channel with different system configurations ($BT = 0.5$).

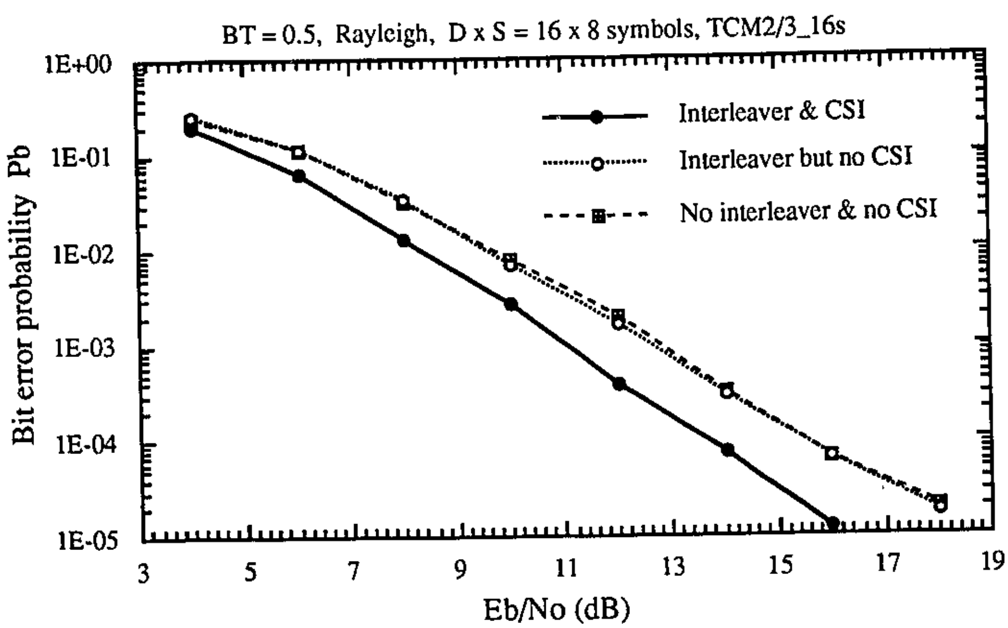

Figure 6.28: Comparison of coherent rate 2/3 16-state TCM on Rayleigh channel with different system configurations ($BT = 0.5$).

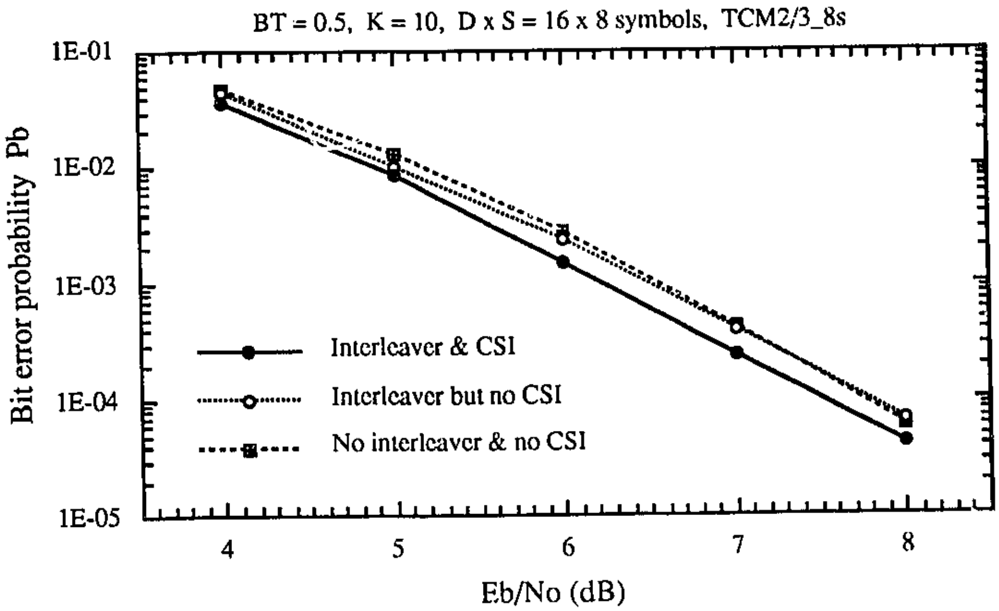

Figure 6.29: Comparison of coherent rate 2/3 8-state TCM on Rician ($K = 10$) channel with different system configurations ($BT = 0.5$).

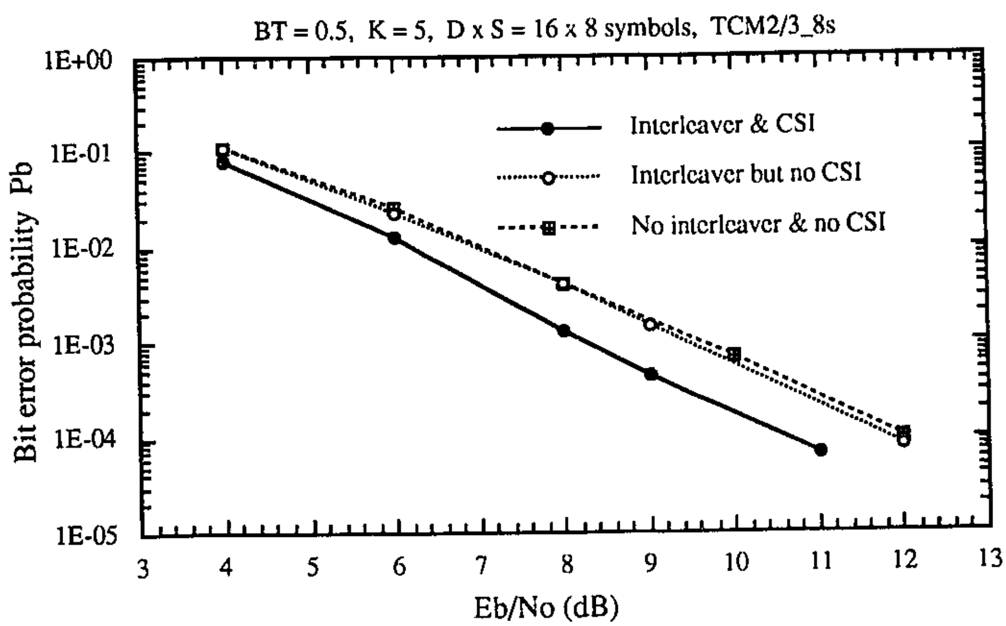

Figure 6.30: Comparison of coherent rate 2/3 8-state TCM on Rician ($K = 5$) channel with different system configurations ($BT = 0.5$).

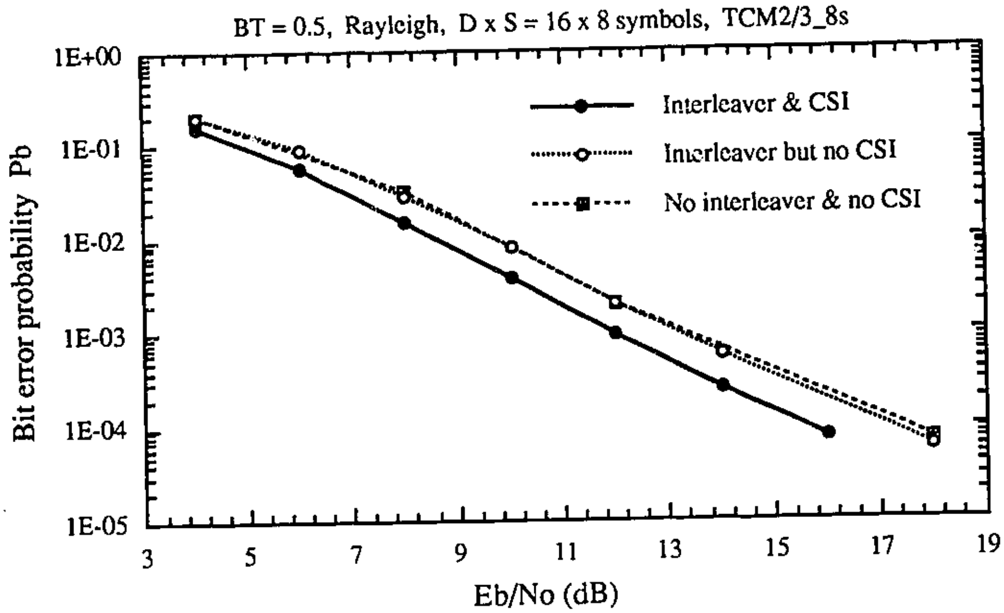

Figure 6.31: Comparison of coherent rate 2/3 8-state TCM on Rayleigh channel with different system configurations ($BT = 0.5$).

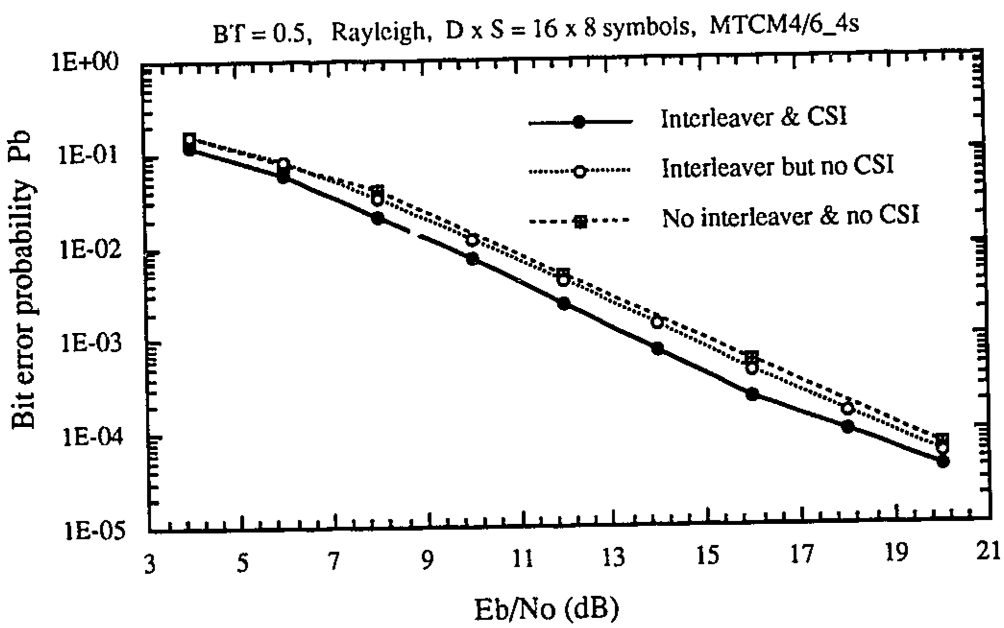

Figure 6.32: Comparison of coherent rate 4/6 4-state MTCM on Rayleigh channel with different system configurations ($BT = 0.5$).

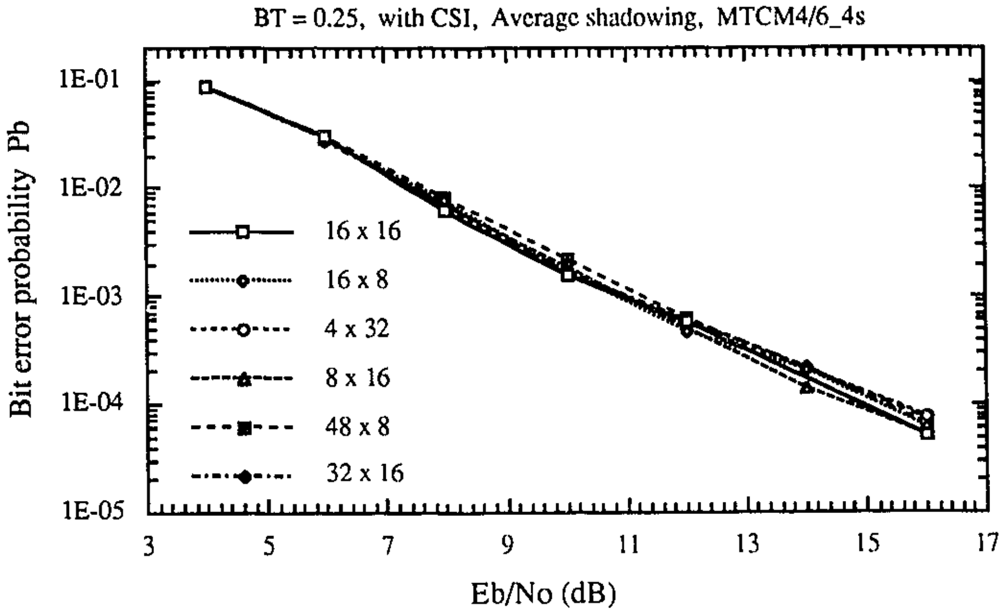

Figure 6.33: Effect of interleaver size on coherent 4-state MTCM system.

6.3 Performance of Differential TCM Systems

In practice, differential detection is often used for mobile satellite communication systems. The simulation model for the differential TCM system was shown in the Figure 4.2 of Chapter 4 and the corresponding SPW block diagrams are illustrated in Appendix A. In this section, the performance results of the simulated TCM systems are presented. For differential detection, it is assumed that the receiving signals suffer both amplitude and phase distortions due to the fading process and white Gaussian random noise. Interleaver and deinterleaver with memory size of 16×8 symbols are also used throughout the simulations. Since carrier recovery is not needed in the differential detection, there is no channel state information available for TCM decoder. Therefore, CSI is not considered in the simulation of the differential TCM system.

6.3.1 Differential TCM Schemes on AWGN Channel

Figure 6.34 presents the performances of the six considered differential TCM schemes on an AWGN channel. The simulation system is calibrated by comparing the performance result of the rate 2/3 8-state TCM code with that published in reference [31]. It is observed that: (1) the performance of the 4-state MTCM scheme is worse than the 4-state conventional TCM scheme at high $\bar{E}_b/N_0$; (2) the 8-state conventional TCM has almost the same performance as the 8-state MTCM; (3) the 16-state and 8-state conventional TCM schemes demonstrate much better performances in comparison with the 4-state TCM; (4) the performance of the 64-state conventional TCM scheme is even worse than 16-state TCM at high $\bar{E}_b/N_0$. The observation shows that the differential 4-state, 8-state and 16-state conventional TCM schemes have better performances than their counterparts in terms of the number of states and complexity in the AWGN environment since these schemes are optimized for the AWGN channel too.

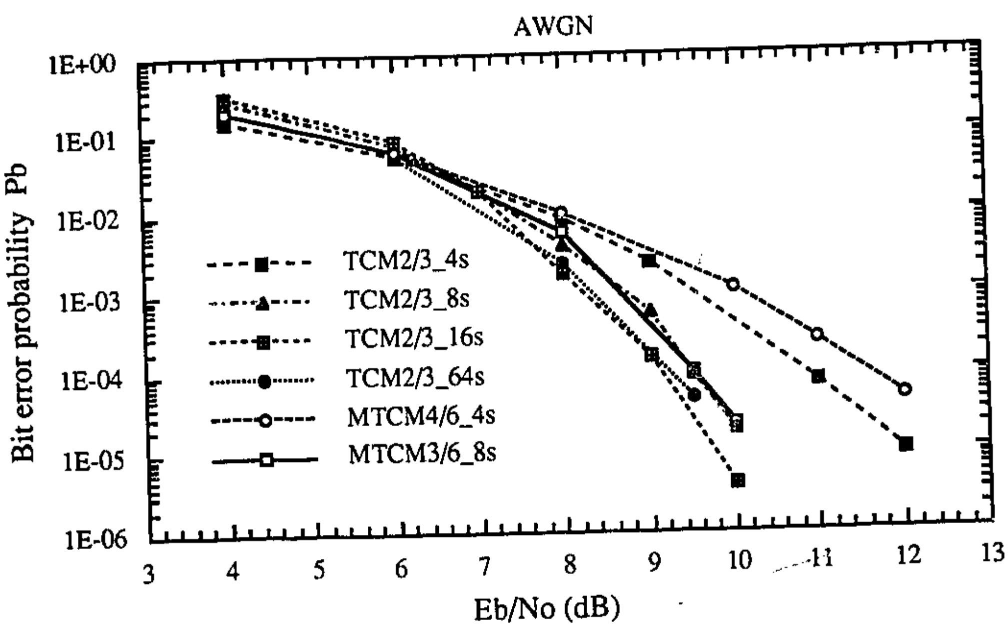

Figure 6.34: Performances of DTCM schemes on AWGN channel.

6.3.2 Differential TCM on Light Shadowed EHF Channel

The performances of the differential TCM schemes over light shadowed Rician model with different fading bandwidth in the presence of white Gaussian noise are illustrated in Figures 6.35 - 6.37.

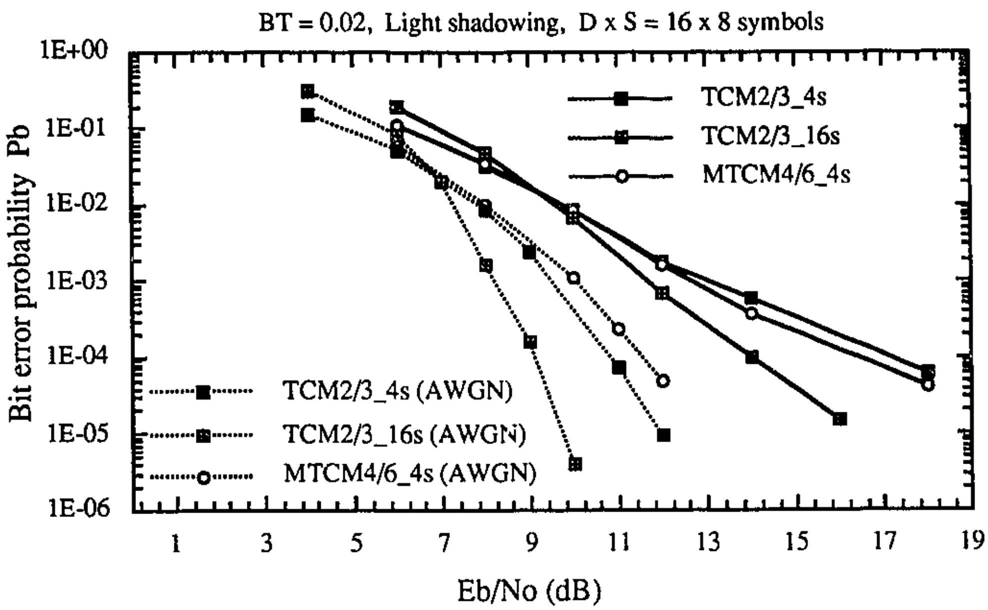

Figure 6.35: Performances of DTCM schemes on light shadowed EHF channel ($BT = 0.02$).

In Figure 6.35, the performances of the differential 4-state and 16-state conventional TCM and 8-state MTCM schemes under the condition of $BT = 0.02$ are compared to the corresponding performances on AWGN channel. At a bit error rate of $P_b = 10^{-4}$, the performances of the differential 4-state, 16-state TCM and 8-state MTCM schemes on light shadowed EHF channel are worse by 6.4 dB, 4.8 dB and 4.9 dB respectively, than with AWGN channel. It shows that the differential 4-state TCM has about 1.5 dB more degradation in performance than the other two schemes. This indicates that the differential 4-state TCM is more sensitive to fading. In this figure, it is also shown that the differential 4-state MTCM scheme has a better performance than its 4-state conventional counterpart when the $\bar{E}_b/N_0$ is high. At $P_b = 10^{-4}$, the

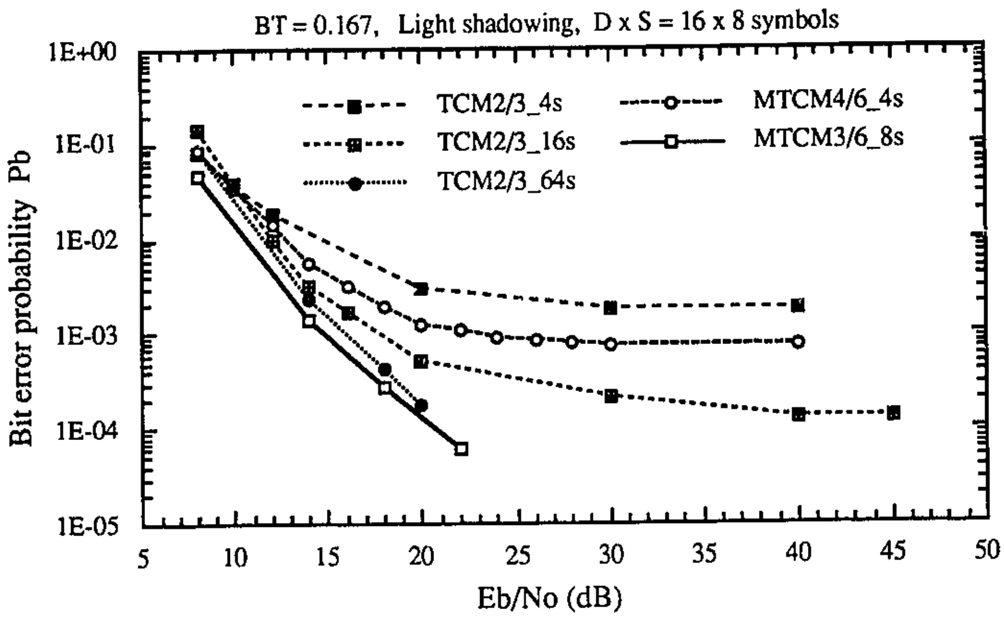

Figure 6.36: Performances of DTCM schemes on light shadowed EHF channel ($BT = 0.167$).

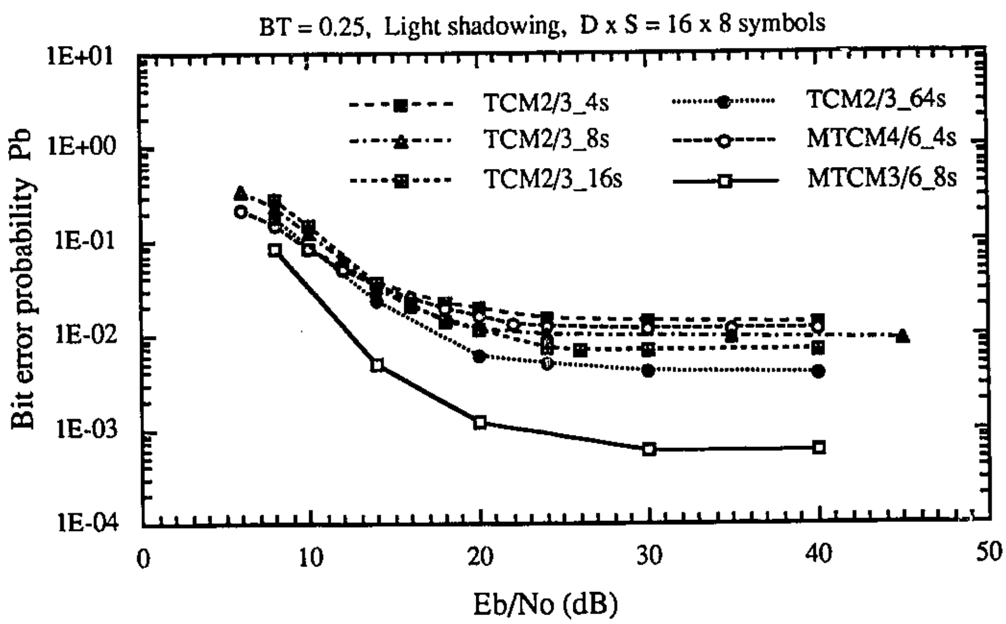

Figure 6.37: Performances of DTCM schemes on light shadowed EHF channel ($BT = 0.25$).

differential 4-state MTCM and 16-state TCM schemes offer about 0.8 dB and 3.4 dB improvement respectively over the differential 4-state conventional TCM scheme.

Figure 6.36 presents the BER performances of the differential TCM schemes on the light shadowed EHF model with $BT = 0.167$. It is seen that most of the schemes under this condition have irreducible error floors. It is noted that the performance of the differential 8-state MTCM is even 1 dB better than that of the 64-state TCM scheme at $P_b = 10^{-3}$.

As is seen in Figure 6.37, error floors occur on all considered differential TCM schemes when the normalized fading bandwidth BT is increased up to 0.25. 8-state MTCM still demonstrates the best performance over other schemes, which has an error floor that is approximately one order of magnitude lower than that of the 64-state conventional TCM.

Figures 6.38 - 6.40 provide BER performance comparison for the TCM schemes under different fading bandwidths.These figures show that the bit error performance of the differential TCM is greatly degraded as the normalized fading bandwidth BT of the EHF fading channel is increased from 0.02 to 0.25 (see Figure 6.38 for 16-state differential TCM scheme on light shadowed EHF channel). This is because the fading bandwidth determines the variation rate of the fading process. The larger of the product BT is, the faster the fading process changes. The phase distortion becomes more severe with the increase of the BT and this phase variation directly affects the bit error performance of the differentially detected TCM system. Similar performances are demonstrated by the 4-state and 64-state conventional TCM as well as the 4-state and 8-state multiple TCM schemes, as shown in Figures 6.39 and 6.40. The better performance of the 8-state MTCM scheme indicates that the multiple TCM is less sensitive to the phase variation than the conventional TCM due to properties of the multidimensional signal.

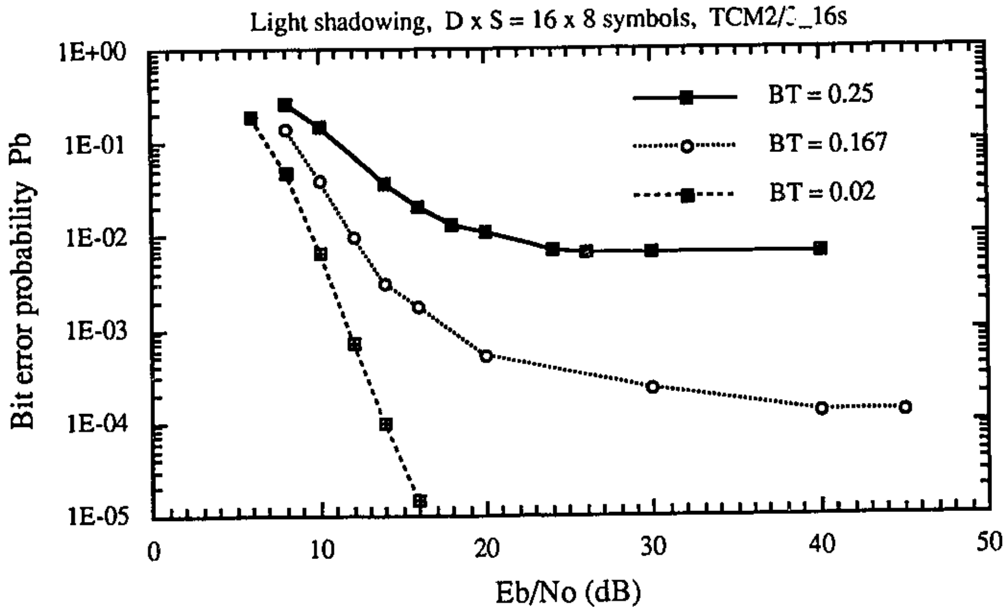

Figure 6.38: Performance of the rate 2/3 16-state DTCM on light shadowed EHF channel for different values of the BT product.

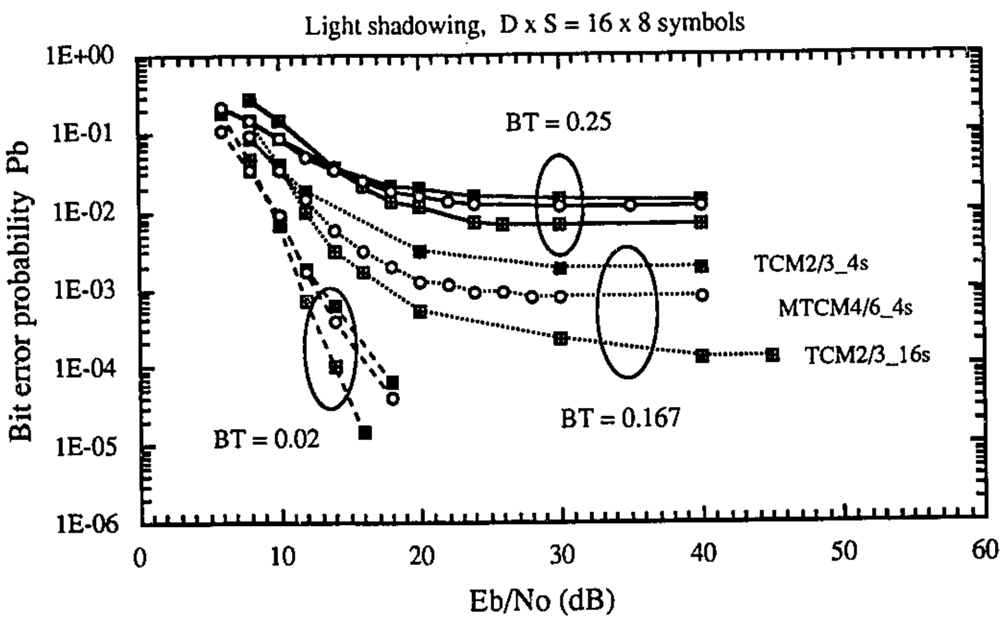

Figure 6.39: Performances of DTCM schemes on light shadowed EHF channel for different values of the BT product (I).

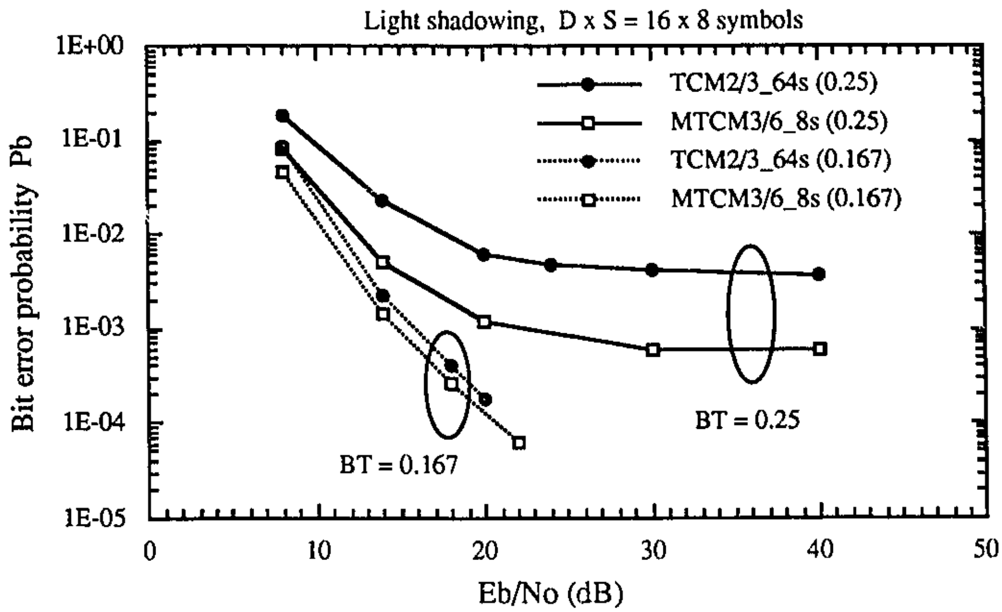

Figure 6.40: Performances of DTCM schemes on light shadowed EHF channel for different values of the BT product (II).

6.3.3 Differential TCM on Average and Heavy Shadowed EHF Channels

The performance results of the differential TCM schemes over the average and heavy shadowed EHF mobile satellite channels in the presence of white Gaussian noise are illustrated in Figures 6.41 and 6.42. It is observed that the error floor occurs when BT is equal to 0.1 for the average shadowed condition. On the heavy shadowed EHF channel, the differential TCM schemes perform poorly even when the product BT is only 0.05. 8-state MTCM provides a better performance than the 16-state and 64-state conventional TCM schemes. The results demonstrate that the combined effect of the Doppler shift and shadowing causes serious degradation on the performance of the differential TCM.

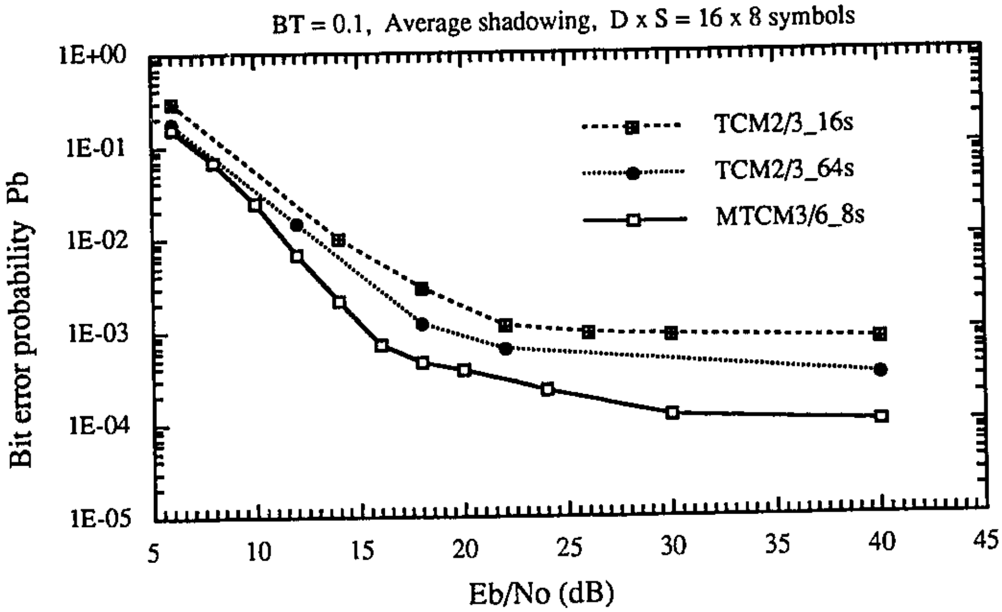

Figure 6.41: Performances of DTCM schemes on average shadowed EHF channel ($BT = 0.1$).

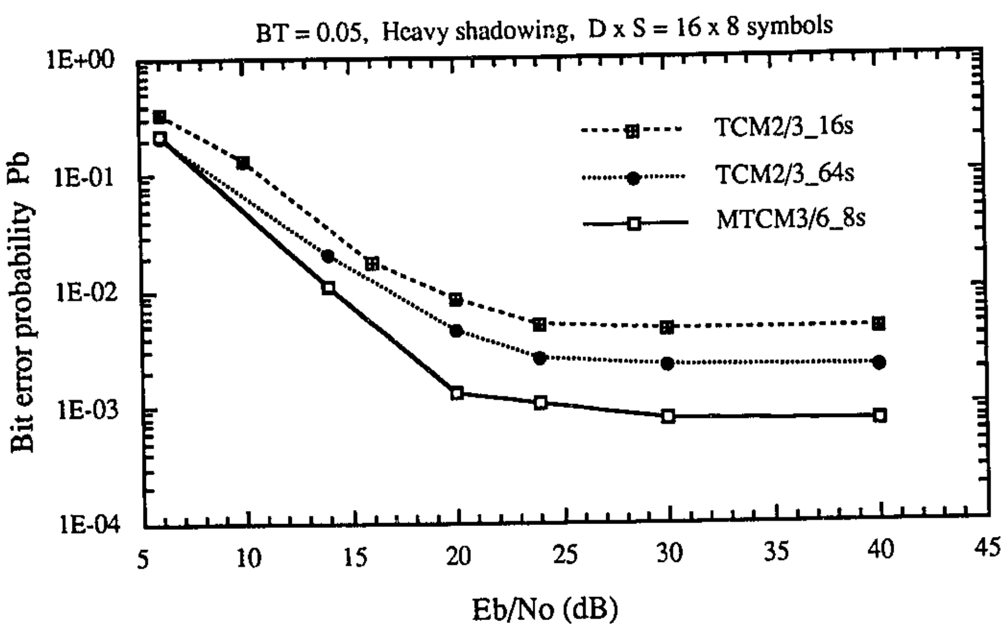

Figure 6.42: Performances of DTCM schemes on heavily shadowed EHF channel ($BT = 0.05$).

6.4 Summary

In this chapter, the simulation results of the coherent and differential TCM systems over the EHF mobile satellite channels are presented and discussed. The emphasis is given on the evaluation and analysis of the coherent TCM schemes based on 8-PSK modulation. The effects of the CSI and interleaving on TCM performance are extensively explored.

From the analysis of the simulation results, the performances of the coherent TCM schemes can be summarized as follows.

- For the EHF fading channels, the performance of a TCM scheme is primarily determined by its effective length L and the product P. The larger the values of L and P, the better the performance of the TCM scheme.
- In comparison with their performances on AWGN channel, the performances of the TCM schemes under consideration degrade significantly on the EHF fading channels.
- With the same code rate and similar complexity, the 4-state multiple TCM demonstrates a better performance than its 4-state conventional counterpart on the EHF fading channels.
- The system performance can be improved by providing the interleaving and CSI. CSI is shown to be always effective in improving the system performance. However, in the case of heavy shadowing and large fading bandwidth BT, the effect of the interleaving is limited.
- On the Rician channel with smaller K value, the CSI is shown to be more effective in improving the TCM performance.
- The interleaver size does not show much impact on the performances of the coherent TCM schemes over the EHF fading channel with large BT.

The performance of the differential TCM is seriously degraded by the severe phase and amplitude distortions that are typically encountered in the EHF mobile satellite communication channel. For the fast fading conditions, the performances of the differential TCM schemes are characterized with irreducible bit error probabilities. As discussed in Chapter 4, the optimum code under the fast fading condition is no longer determined by the effective length and branch distance product. From the performance behavior of the 8-state MTCM scheme, it is shown that this scheme is quite insensitive to the phase jitter and provides the best BER performances among these considered TCM schemes.

Chapter 7

Conclusions and Suggestions

7.1 Thesis Summary

The main objective of this thesis is to investigate the propagation impairments on EHF (30/20 GHz) mobile satellite communication channels, and to study the corresponding error control and modulation techniques to combat these impairments.

Corresponding to the different signal propagation environments, the behavior of the EHF mobile satellite communication channel is represented by Rayleigh, Rician and log-normally shadowed Rician statistical models. The channel fading impairments expected at the 30/20 GHz EHF frequency band are dominated by the effects of multipath fading as well as vegetative shadowing. By rescaling L-band (1.6/1.5 GHz) mobile satellite channel parameters, a set of modified parameters is derived for the log-normally shadowed EHF fading model. With these parameters, the log-normally shadowed Rician fading process is identified by light, average and heavy shadowed conditions.

The bandwidth and power efficient coding and modulation technique, trellis-coded modulation, is considered to be a good choice to mitigate the severe propagation impairments on EHF mobile satellite channel. The interleaving technique is shown to be an effective means to combat the burst errors. In conjunction with the interleaving and the provision of channel state information, trellis-coded modulation exhibits a significant error control capability on the fading channels. Multiple TCM schemes have been shown to improve the code design flexibility and performance results.

The performance of a TCM scheme on fading channels is primarily determined by the effective length L and the product P of the code. The free Euclidean distance, which is the major criterion for optimum TCM code on AWGN, is only of secondary importance for the fading channel context. Six TCM schemes, optimized for fading channels, are presented and their properties based on 8-PSK modulation are discussed in detail.

The performances of the coherent and differential trellis-coded modulation systems are analyzed as error probability upper bounds for the Rician fading channel.

Due to the complexity in deriving the analytical performance expressions, computer simulation method is used to investigate the TCM schemes. Based on the proposed EHF channel models, computer simulation systems are set up for both the coherently detected and the differentially detected TCM strategies. The performances of the selected TCM schemes are evaluated extensively in the presence of the different fading conditions.

The results obtained from the simulations show the behavior of TCM systems over the modeled EHF fading channels. Through analysis of these simulation results, the performances of these TCM schemes are appraised. This assessment should provide a useful insight for the design and implementation of the EHF mobile satellite modems.

7.2 Concluding Remarks

Based on the performance analysis and computer simulation of the trellis-coded modulation technique over the EHF mobile satellite channel, following conclusions can be drawn:

A. Coherent Trellis-coded Modulation System

- the coherent TCM schemes demonstrate good performance on the EHF fading models, even under Rayleigh and heavy shadowed Rician channel conditions. The performance of the TCM scheme is improved as the code effective length increases;
- with interleaving and channel state information, the applied TCM schemes demonstrate their best performances over the fading channel; a 2 to 3 dB gain is achieved at BER of 10^{-4} over TCM schemes without CSI and interleaving;
- the interleaving effect on the performance improvement of the TCM schemes depends on the fading bandwidth, shadowing condition, and the code error correcting capability;
- the 4-state multiple TCM scheme outperforms the 4-state conventional counterpart by 1 to 2 dB at a bit error rate of 10^{-4} under the different fading conditions; the 4-state multiple TCM appears as a good modulation scheme if the code complexity is the primary consideration;

B. Differential Trellis-coded Modulation System

- the performances of the differential TCM schemes degrade significantly with the increase of the normalized fading bandwidth BT and shadowing effects; under large BT and severe shadowing conditions, the performances of the differential TCM schemes are affected by the irreducible error probability floors;
- the performance of a TCM code is not determined by the effective length L under the fast fading condition;
- the rate 3/6 8-state multiple TCM scheme is less sensitive to the phase jitter than the other TCM schemes.

7.3 Suggestions for Future Research

With respect to this subject, several aspects are of interest for further study.

1. Since the frequency scaling factor used in deriving the EHF channel model parameters is obtained from a conditioned propagation environment [3], therefore, further modification would be necessary once actual EHF mobile satellite propagation statistics are made available.

2. Diversity techniques such as antenna diversity can be applied to further improve the performance of the TCM schemes.

3. For differential TCM system, multiple symbol differential detection would achieve better performance results.

4. Other TCM techniques such as multidimensional TCM and multi-level trellis coding methods can also be considered for EHF mobile satellite channels.

Appendix A

SPW Block Diagrams of Simulation Systems and Modules

This appendix contains the SPW block diagrams of the simulation systems and modules developed for our performance evaluations. Since there are a lot of variations of the system implementation with respect to different system conditions, a limited number of typical system configurations are chosen for demonstrative purpose.

The average Gaussian channel module used in TCM system simulations is shown in Figure A.1. By taking $\bar{E}_b/N_0$ as the signal to noise parameter, the corresponding complex Gaussian white noise is generated at the output of this module.

In Figure A.2 - A.4, the block diagrams of SPW for Rayleigh, Rician and log-normally shadowed Rician channel modules are presented. These modules are used as system components throughout the simulations.

Figures A.5 - A.8 present some typical block diagrams of the simulated systems, including the coherent and differential system, as well as the conventional and multiple TCM examples. All the other system diagrams are similar to these but with different configurations and parameters.

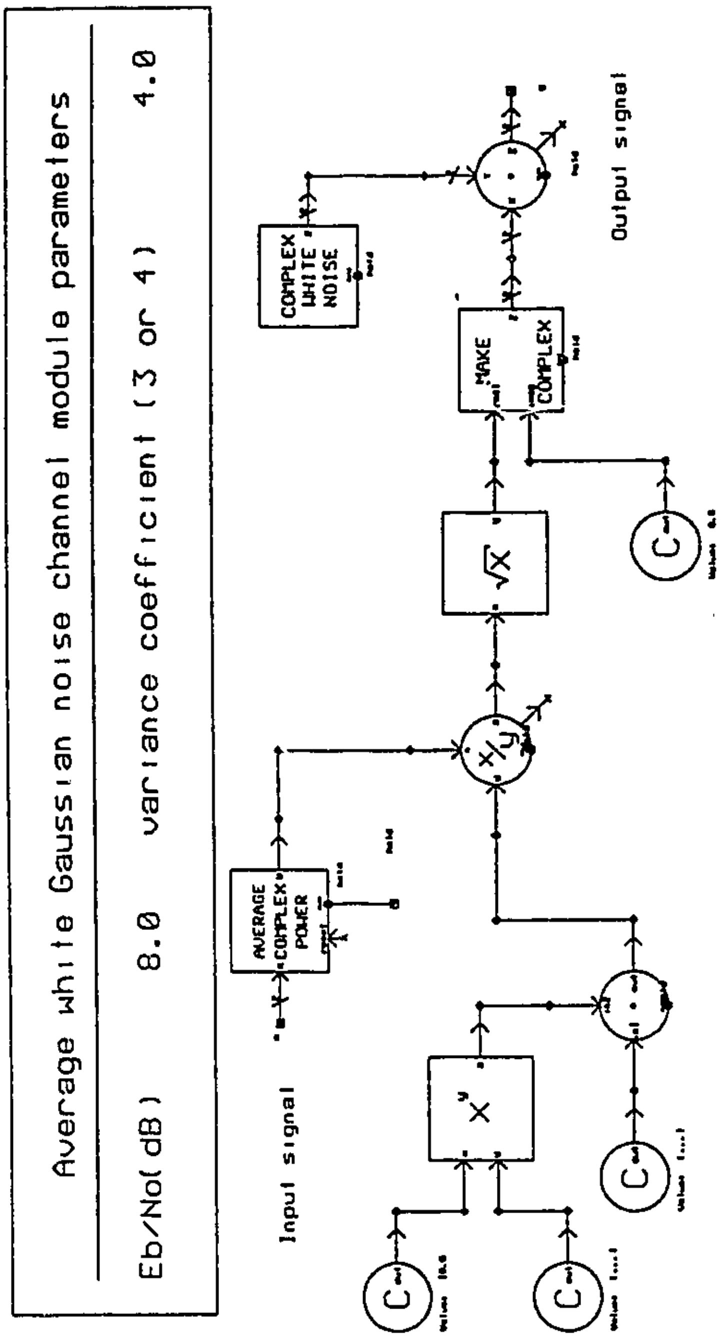

Figure A.1: Block diagram of SPW for AWGN channel module.

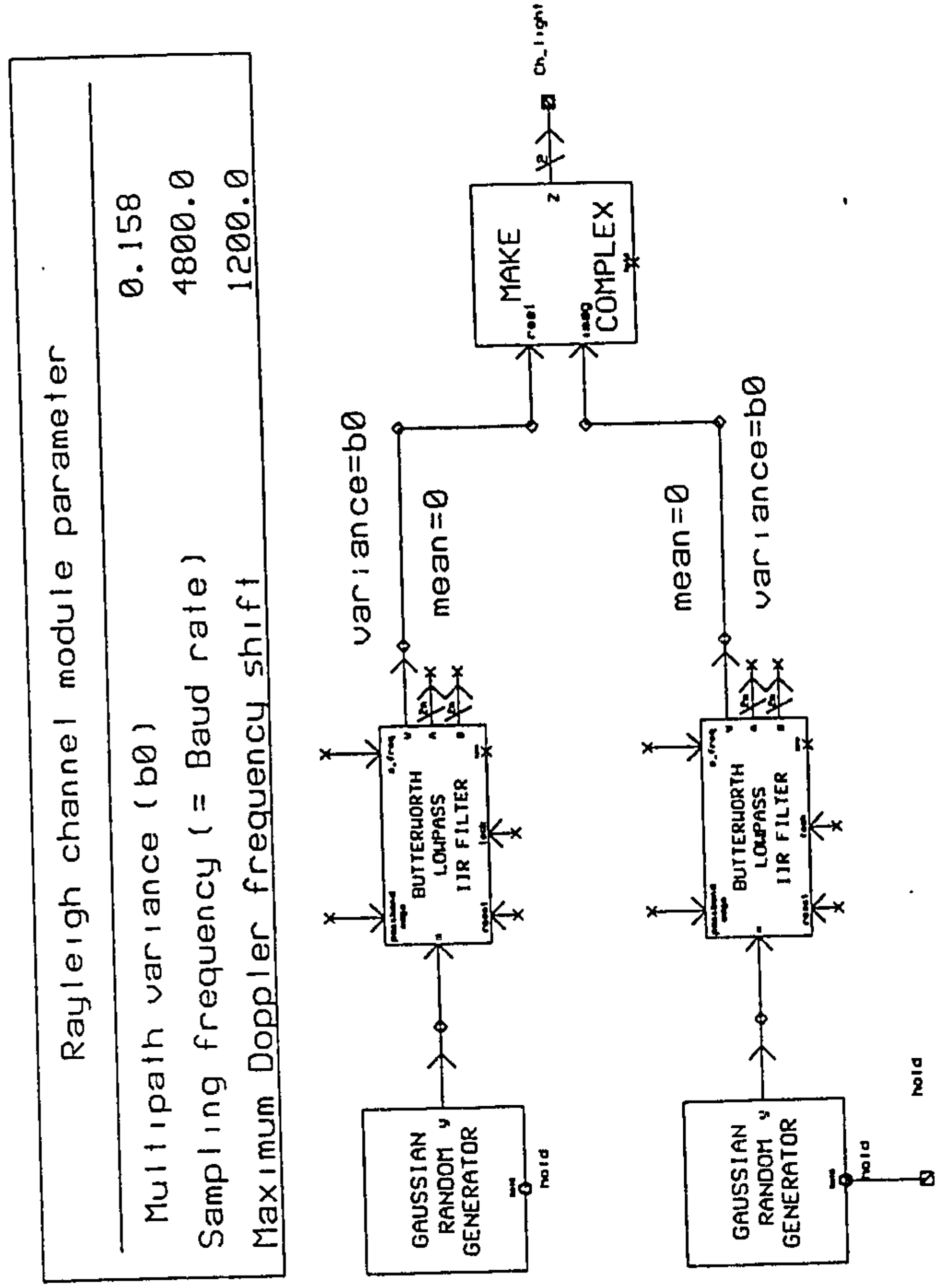

Figure A.2: Block diagram of SPW for Rayleigh channel module.

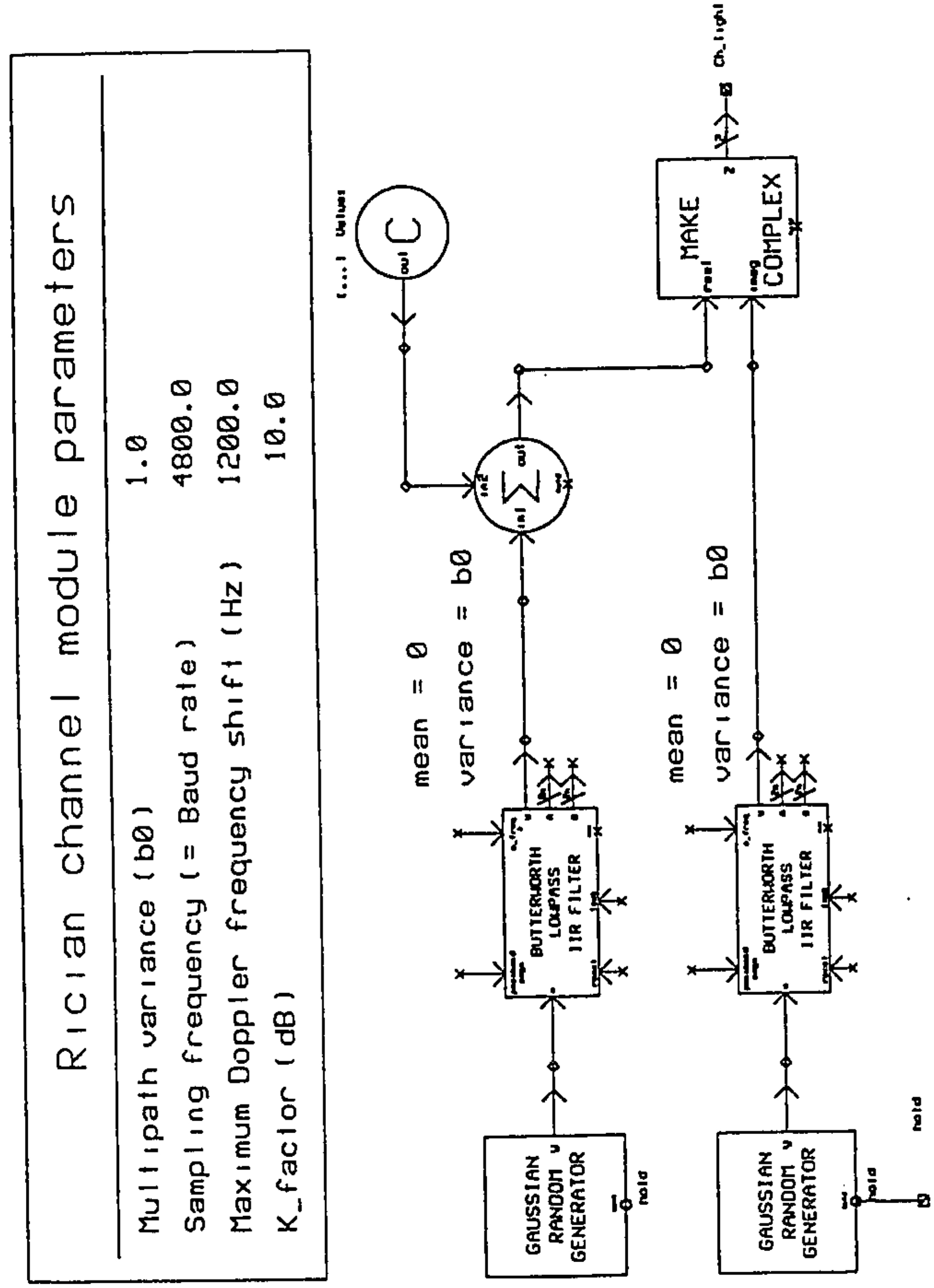

Figure A.3: Block diagram of SPW for Rician channel module.

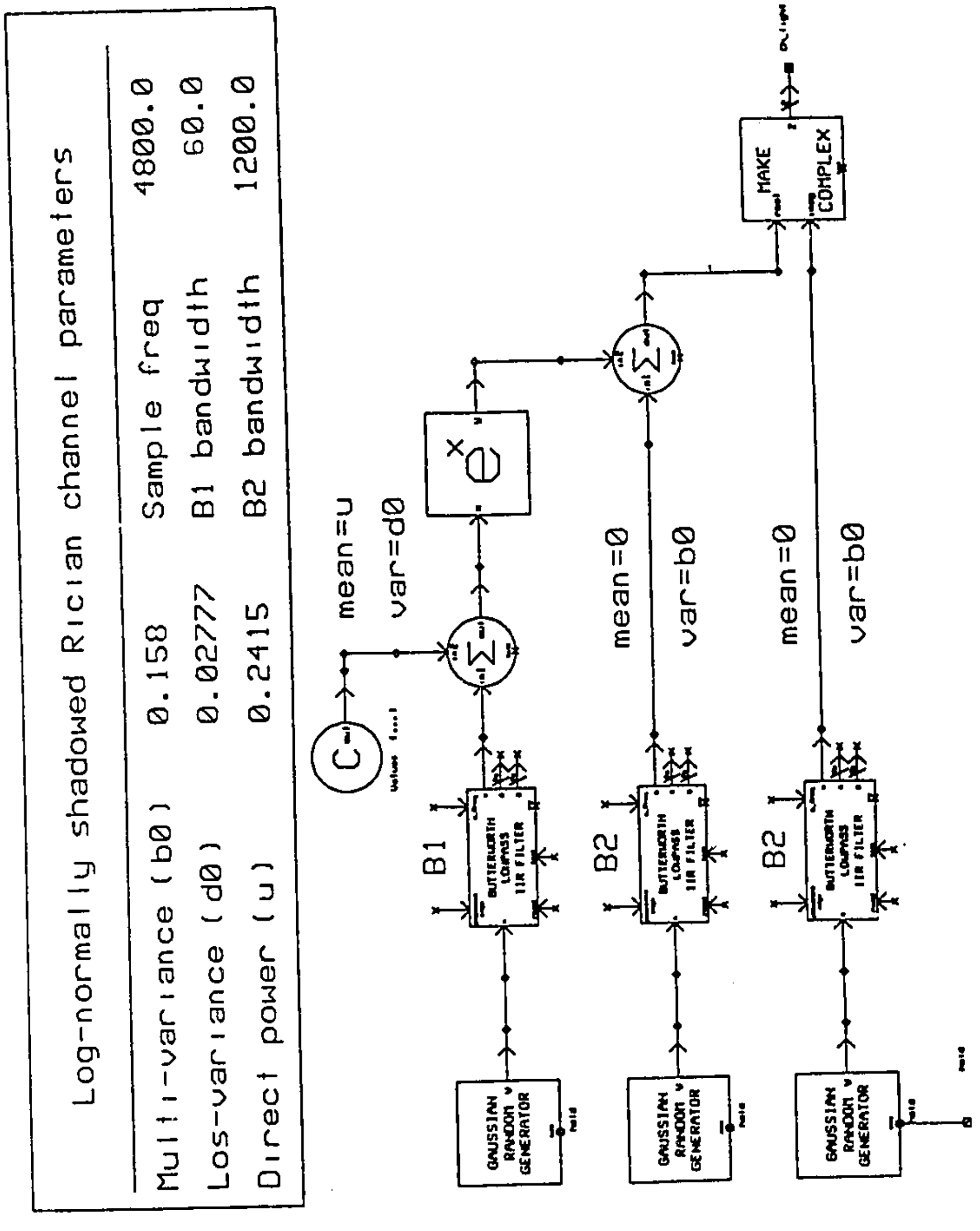

Figure A.4: Block diagram of SPW for log-normally shadowed Rician channel module.

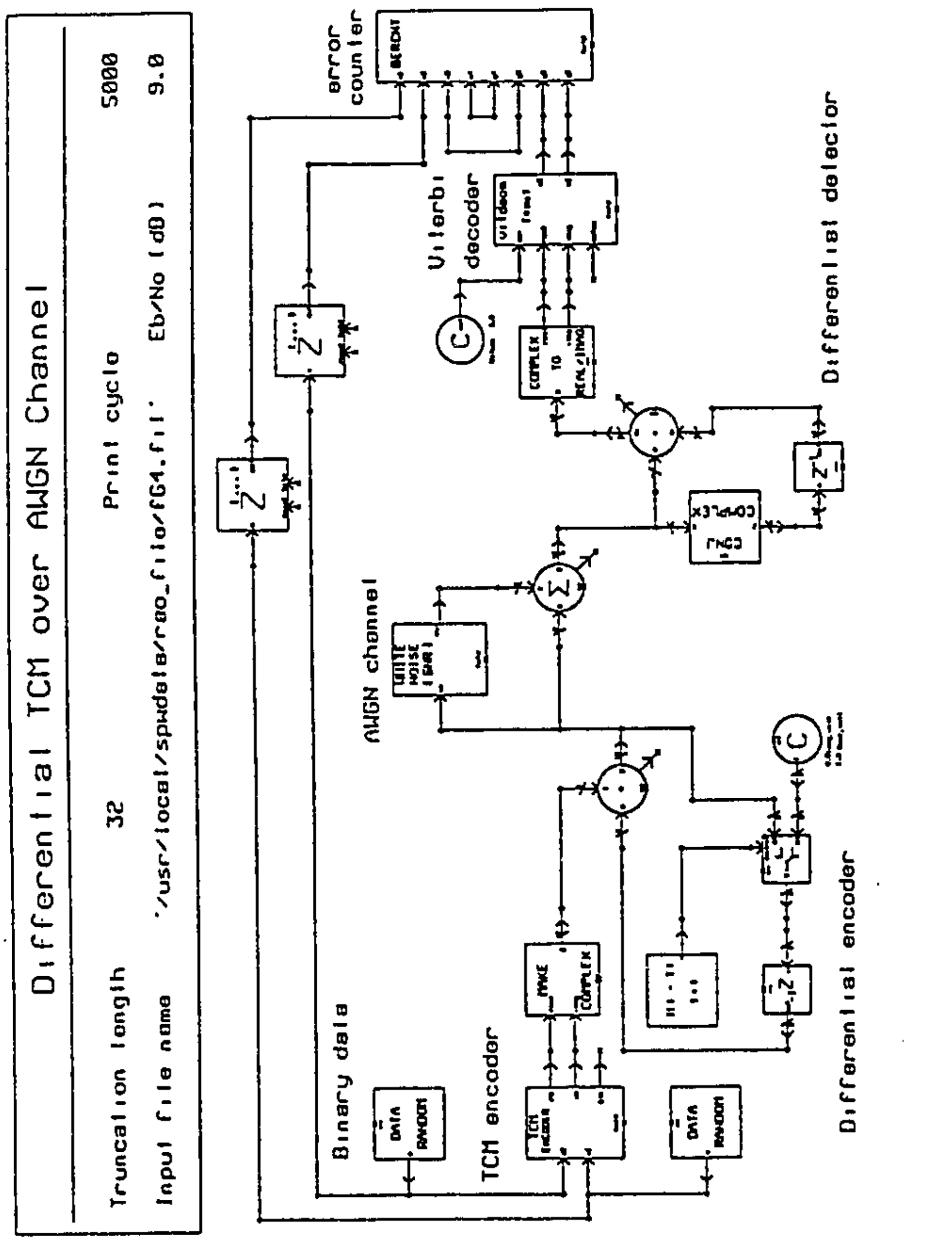

Figure A.5: Block diagram of SPW for rate 2/3 differential TCM system.

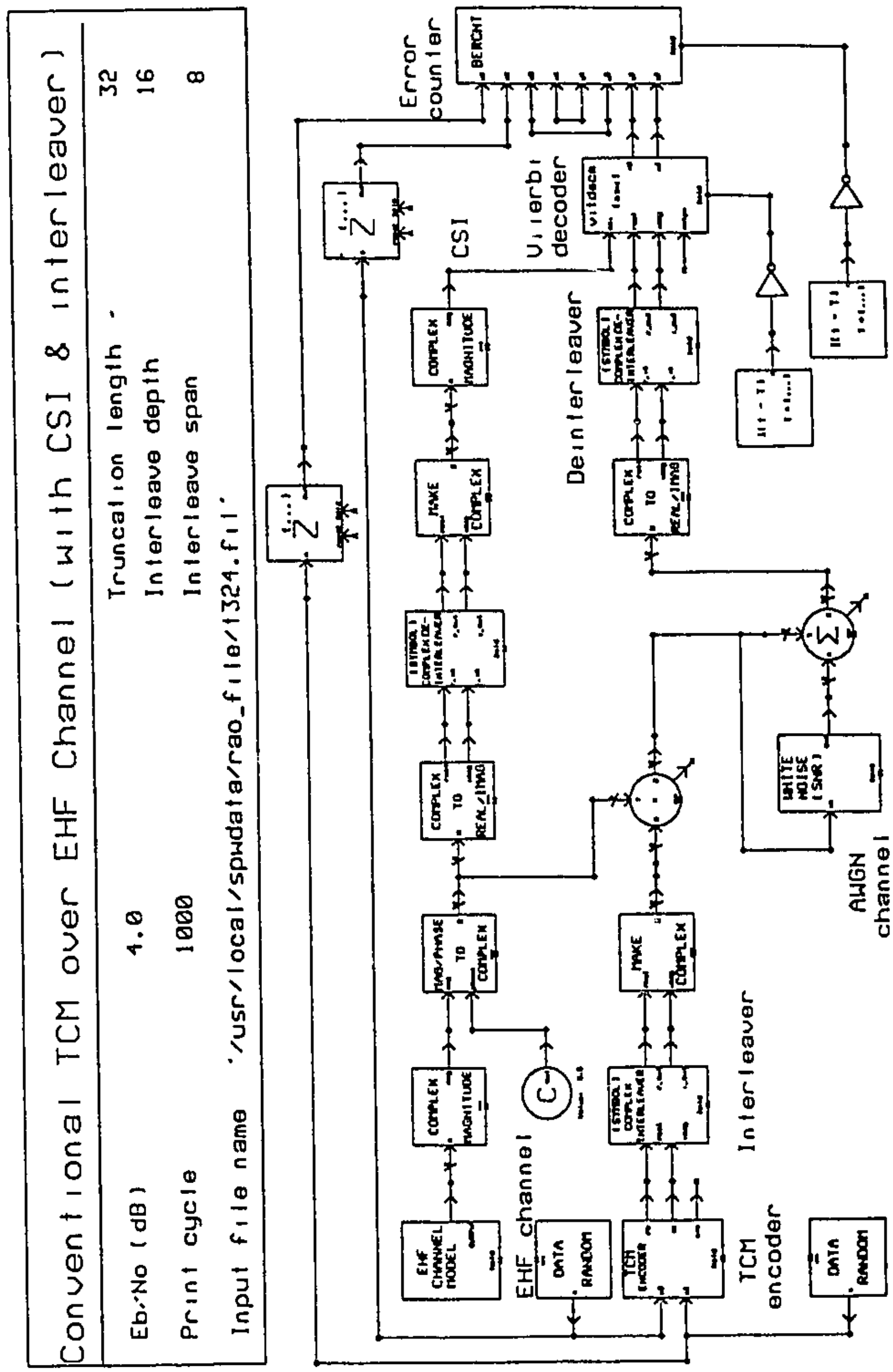

Figure A.6: Block diagram of SPW for coherent conventional TCM system with interleaver and CSI.

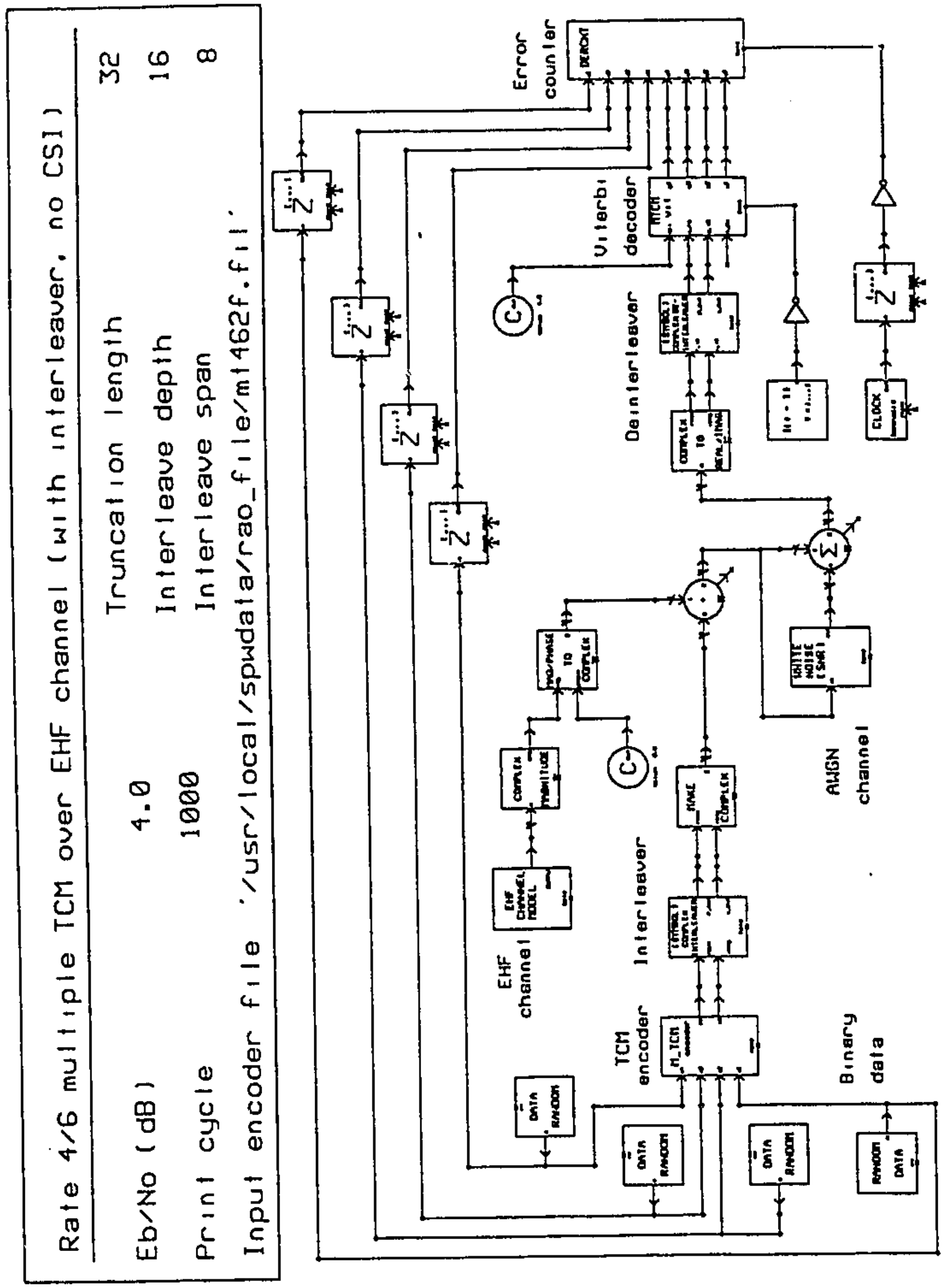

Figure A.7: Block diagram of SPW for coherent rate 4/6 MTCM system with interleaver and without CSI.

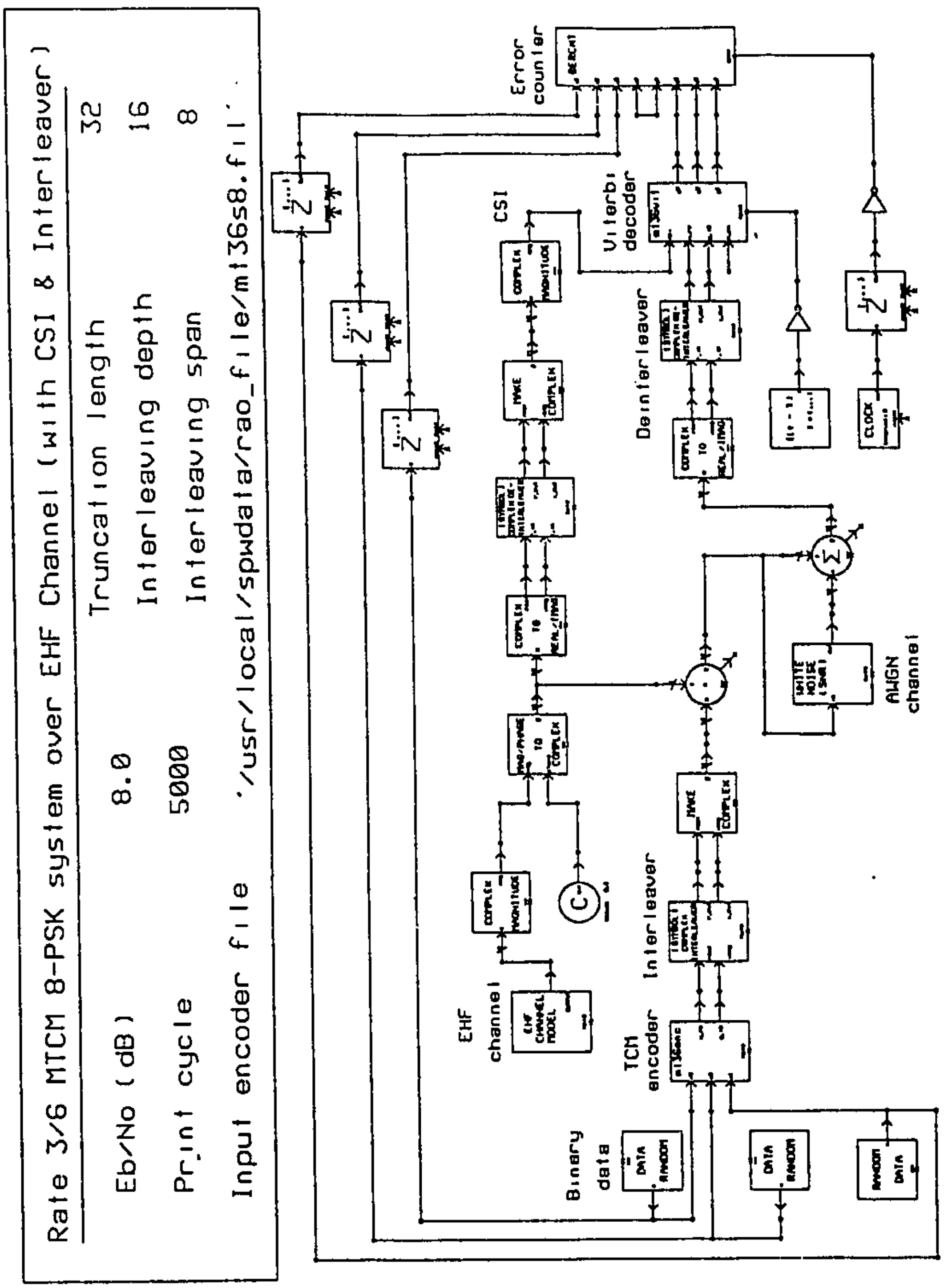

Figure A.8: Block diagram of SPW for coherent rate 3/6 MTCM system with interleaver and CSI.

Bibliography

[1] J. H. Lodge, "Mobile satellite communications systems: Toward global personal communications," *IEEE Comm. Magazine*, Vol. 29, No. 11, pp. 14-12, Nov. 1991.

[2] S. K. Barton and J. R. Norbury, "Future mobile satellite communication concepts at 20/30 GHz," *Proc. Int. Mobile Satellite conf.*, Ottawa, pp. 64-69, 1990.

[3] J. Fortuny, J. Benedicto and M. Sforza, " Mobile satellite system at Ku and Ka-band," pp. 55-62, *Proceeding of Second European Conference on Satellite Communication,* Belgium, Oct. 1991.

[4] L. J. Ippolito, "Propagation effects and system performance considerations for satellite communications above 10 GHz," in *Proc. GLOBECOM'90,* San Diego, pp. 302.1.1-302.1.6, 1990.

[5] William C. Y. Lee, *Mobile Communications Engineering,* New York, McGraw-Hill, 1982.

[6] W. C. Jakes, *Microwave Mobile Communication* , New York, Wiley, 1974.

[7] Chun Loo, "A statistical model for a land mobile satellite link," *IEEE Trans. on Veh. Technol.*, Vol. VT-34, pp. 122-127, Aug. 1985.

[8] C. Loo, E. E. Matt, J. S. Butterworth and M. Dufour, "Measurements and Modeling of land mobile satellite signal statistics," *Proc. of Vehicular Technology Conference* , Dallas, Texas, May,1986.

[9] C. Loo, "Digital transmission through a land mobile satellite channel," *IEEE Trans. Commun.*, Vol. 38, pp. 693-697, May 1990.

[10] C. Loo and N. Secord, "Computer model for fading channel with applications to digital transmission," *IEEE Trans. Veh. Technol.*, Vol. VT-40, No. 4, pp. 700-707, Nov. 1991.

[11] R. M. Barts and W. L. Stutzman, "Modeling and simulation of mobile satellite propagation," *IEEE Trans. on Antenna and Propagation*, Vol. 40, No. 4, pp. 375-382, Apr. 1992.

[12] B. Vucetic and Jun Du, "Channel modeling and simulation in satellite mobile communication systems," *IEEE J. Select. Areas Commun.*, Vol. 10, No. 8, pp. 1209-1218, Oct. 1992.

[13] J. P. Castrao, "Statistical observations of data transmission over land mobile satellite channels," *IEEE J. Select. Areas Commun.*, Vol. 10, No. 8, pp. 1227-1235, Oct. 1992.

[14] W. Zhuang, J.-Y. Chouinard and A. Yongacoglu, "Transmission over EHF mobile satellite channels," *Proc. Int. Mobile Satellite conf.* , Pasadena, California, June 1993.

[15] W. Zhuang, A. Yongacoglu, J.-Y. Chouinard and D. Makrakis, "Performance analysis of EHF land mobile satellite system - Part I: EHF channel modeling and performance of coherent PSK systems," Technical Report No. 1, Department of Electrical Engineering, University of Ottawa, Sept. 1992.

[16] G. Ungerboeck, "Channel coding with multilevel/phase signals," *IEEE Trans. Inform. Theory*, Vol. IT-28, pp. 56-66, Jan. 1982.

[17] G. Ungerboeck, "Trellis-coded modulation with redundant signal set, Part II: State of the art," *IEEE Commun. Mag.*, Vol. 25, No. 2, pp. 12-21, Feb. 1987.

[18] G. D. Forney, R. G. Gallager, G. R. Lang, F. M. Longstaff and S. U. Qureshi, "Efficient modulation for band-limited channel," *IEEE J. Select. Areas Commun.*, Vol. SAC-2, No. 5, pp. 632-645, Sept. 1984.

[19] L. F. Wei, "Trellis-coded modulation with multidimensional constellations," *IEEE Trans. Inform. Theory*, Vol. IT-33, pp. 483-501, July 1987.

[20] D. Divsalar and M. K. Simon, "Multiple trellis coded modulation (MTCM)," *IEEE Trans. Commun.*, Vol. 36, No. 4, pp. 410-419, Apr. 1988.

[21] D. Divsalar and M. K. Simon, "Trellis coded modulation for 4800-9600 bit/s transmission over a fading mobile satellite channel," *IEEE J. Select. Areas Commun.*, Vol. SAC-5, pp. 162-175, No. 2, Feb. 1987.

[22] D. Divsalar and M. K. Simon, "The design of trellis coded modulation for MPSK for fading channel: Performance criteria," *IEEE Trans. Commun.*, Vol. 36, pp. 1004-1012, Sept. 1988.

[23] D. Divsalar and M. K. Simon, "The design of trellis coded MPSK for fading channels: Set partitioning for optimum code design," *IEEE Trans. Commun.*, Vol. 36, pp. 1013-1021, Sept. 1988.

[24] G. Ungerboeck, "Trellis-coded modulation with redundant signal set, Part I: Introduction," *IEEE Commun. Mag.*, Vol. 25, No. 2, pp. 5-11, Feb. 1987.

[25] C. Schlegel and D. J. Costello, "Bandwidth efficient coding for fading channels: Code construction and performance analysis," *IEEE J. Select. Areas Commun.*, Vol. 7, No. 9, pp. 1356-1368, Dec. 1989.

[26] S. H. Jamali and T. Le-Ngoc, "A new 4-state 8PSK TCM scheme for fast fading, shadowed mobile radio channels," *IEEE Trans. Inform. Theory.*, Vol. 40, No. 1, pp. 216-222,, Feb. 1991.

[27] S. G. Wilson and Y. S. Leung, "Trellis-coded phase modulation on Rayleigh channels," *ICC'87 Conf. Rec.*, Seattle, WA, pp. 21.3.1-21.3.5, June 1987.

[28] E. Zehavi, "8PSK trellis codes for a Rayleigh channel," *IEEE Trans. Commun.*, Vol. 40, No. 5, pp. 873-884, May 1992.

[29] M. Bertelsmeier and G. Komp, "Trellis-coded 8PSK with embedded QPSK," *IEEE J. Select. Areas Commun.*, Vol. 7, No. 9, pp. 1296-1306, Dec. 1989.

[30] F. Edbauer, "Performance of interleaved trellis-coded differential 8-PSK modulation over fading channels," *IEEE J. Select. Areas Commun.*, Vol. 7, No. 9, pp. 1340-1346, Dec. 1989.

[31] A. C. M. Lee and P. J. Mclane, "Convolutionally interleaved PSK and DPSK trellis codes for shadowed, fast fading mobile satellite communication channels," *IEEE Trans. Veh. Technol.*, Vol. 39, No. 1, pp. 37-47, Feb. 1990.

[32] P. J. Mclane, P. H. Wittke, P. K. -M. Ho and C. Loo, "PSK and DPSK trellis codes for fast fading, shadowed mobile satellite communication channels," *IEEE Trans. Commun.*, Vol. 36, No. 11, pp. 1242-1246, Nov. 1988.

[33] M. K. Simon and D. Divsalar, "The performance of trellis coded multilevel DPSK on a fading mobile satellite channels," *IEEE Trans. Veh. Technol.*, Vol. 37, No. 2, pp. 78-91, May 1988.

[34] E. Biglieri, D. Divsalar, P. J. McLane and M. K. Simon, *Introduction to Trellis-coded Modulation with Applications*, New York, Macmillan Publishing Company, 1991.

[35] R. G. McKay, P. J. Mclane and E.Biglieri, "Error bounds for trellis-coded MPSK on a fading mobile satellite channel," *IEEE Trans. Commun.*, Vol. 39, No. 12, pp. 1750-1761, Dec. 1991.

[36] J. K. Cavers and P. Ho, "Analysis of the error performance of trellis-coded modulations in Rayleigh fading channels," *IEEE Trans. Commun.*, Vol. 40, No. 1, Jan. 1992.

[37] J. Huang and L. L. Campbell, "Trellis coded MDPSK in correlated and shadowed Rician fading channels," *IEEE Trans. Veh. Technol.*, Vol. 40, No. 4, pp. 786-797, Nov. 1991.

[38] Jay Jie Huang, "Tail Probability of a Noncentral Indefinite Gaussian Quadratic Form with Applications in Trellis Coded MDPSK Studies," Ph.D. Thesis, Department of Electrical Engineering, Queen's University, Kingston, Ontario, Canada, 1991.

[39] John G. Proakis, *Digital Communications*, McGraw-Hill, 1989.

[40] G. D. Forney, "The Viterbi algorithm," *Proceedings of the IEEE* , Vol. 61, No. 3, pp. 268-278, Mar. 1973.

[41] F. Davarian, "Mobile digital communications via tone calibration," *IEEE Trans. Veh. Technol.*, Vol. 36, No. 2, pp. 55-62, May 1987.

[42] J. McGeehan and A. Bateman, "Phase-lock transparent tone-in-band(TTIB): A new spectrum configuration particularly suited to the transmission of data over SSB mobile radio networks," *IEEE Trans. Commun.*, Vol. 32, No. 1, pp. 81-87, Jan. 1984.

[43] *Signal Processing Work System-User's Manual*, Comdisco, Inc.

[44] M. C. Jeruchim, P. Balaban and K. S. Shanmugan, *Simulation of Communication Systems*, Plenum Press, New York,1992.

[45] P. Ho and D. K. P. Fung, "Error performance of interleaved trellis-coded PSK modulations in correlated Rayleigh fading channels," *IEEE Trans. Commun.*, Vol. 40, pp. 1800-1809, Dec. 1992.